An Analytical and Numerical Study of the Second-Order Effects of Unsteadiness on the Performance of Turbomachines

by

Gerd Fritsch

Diplom-Ingenieur Maschinenwesen
Universität Stuttgart (1987)

SUBMITTED TO THE DEPARTMENT OF
AERONAUTICS AND ASTRONAUTICS
IN PARTIAL FULFILLMENT OF THE REQUIREMENTS
FOR THE DEGREE OF

Doctor of Science
at the
Massachusetts Institute of Technology

June 1992

Signature of the Author _____
Department of Aeronautics and Astronautics
March 31, 1992

Certified by _____
Professor Michael B. Giles
Thesis Supervisor, Department of Aeronautics and Astronautics

Certified by _____
Professor Edward M. Greitzer
Department of Aeronautics and Astronautics

Certified by _____
Professor Mark Drela
Department of Aeronautics and Astronautics

Accepted by _____
Professor Harold Y. Wachman
Chairman, Department Graduate Committee

An Analytical and Numerical Study of the Second-Order Effects of Unsteadiness on the Performance of Turbomachines

by

Gerd Fritsch

Submitted to the Department of Aeronautics and Astronautics
on March 31, 1992
in partial fulfillment of the requirements for the degree of
Doctor of Science in Aeronautics and Astronautics

A linear approach in two dimensions is used to investigate the second-order effects of unsteadiness on the efficiency of turbomachines. The three main themes are the identification of physical nature and location of unsteady loss mechanisms, the magnitude of the associated losses and their effect on the time-mean efficiency, and the assessment of the modeling accuracy of numerical simulations with respect to unsteady loss.

A mathematically rigorous link is established between linear waves in a compressible, two-dimensional flow and the efficiency drop associated with their dissipation. The analysis is applied to the mixing loss at the interface in a steady simulation of rotor/stator interaction in a turbine and to the study of unsteady loss mechanisms.

Two unsteady loss mechanisms are considered. Unsteady Circulation Loss, i.e. the transfer of mean-flow energy to kinetic energy associated with vorticity shed at the trailing edge in response to an unsteady circulation, was first considered by Keller (1935) and later by Kemp and Sears (1955). Keller's original work is extended to compressible, homentropic flows. The use of simulations to obtain circulation amplitudes avoids the limitations of thin-airfoil theory and yields a loss measure realistic for modern turbomachines. For the Unsteady Viscous Loss mechanism, i.e. the dissipation induced by pressure waves in unsteady boundary layers, the high-reduced-frequency limit and a near-wall approximation are used to obtain the local velocity distribution in the laminar Stokes sublayer and the corresponding time-mean dissipation. The input to the model are the unsteady pressure gradients along a blade surface obtained from an unsteady simulation. A numerical study of the errors due to modeling approximation is included.

Both sources of loss are small but not negligible. It is found that numerical smoothing shifts the principal locus of unsteady dissipation from boundary layers to the freestream, reducing the magnitude of the loss models input and the predicted loss.

Thesis Supervisor: Michael B. Giles,
Associate Professor of Aeronautics and Astronautics

Acknowledgments

It all started a little more than four years ago, when I concluded that it wasn't quite the time yet to settle down in southern Germany. Now, with almost four years of graduate study behind me, I have only one last page to go ...

Looking back, I can call these years at MIT an important and rewarding experience both in academic and personal terms. It was an experience that I would not want to have missed, although there have been innumerable times when I wished I had never asked for the application forms.

First, I would like to express my gratitude to my advisor, Prof. Michael B. Giles, for his support, advice, and encouragement throughout this project. He was an excellent teacher as well, and always had an open ear for my ideas and problems. I would like to thank Prof. Edward M. Greitzer for his constructive criticism and encouragement. Thanks also to Prof. Mark Drela for his helpful comments, and to the readers, Profs. Mårten T. Landahl and Alan H. Epstein, for their suggestions.

Thanks in no small measure is due to my fellow students in the CFD-Lab; their company and support have helped this project more than they may realize. Special thanks goes to Guppy, my climbing partner and friend, who constantly reminded me that there is life outside MIT. Countless are the summer days, when he tempted me with outdoor endeavors; needless to say that he met little resistance.

Special thanks also goes to Patrick and Harold for their friendship. Not only have they tolerated my little-refined social skills (not without the appropriate comments) and provided for many an interesting discussion, they have also been superb company in such diverse places as the Yucatan Peninsula of Mexico, Yosemite National Park in California, Acadia National Park in Maine, the many rocks of the East Coast, and, all too often, MIT.

Finally, I would like to thank Denise, my friend and fiancée. Her friendship, love, support, and fighting spirit contributed greatly to this project. With my departure, she will finally be able to cut her last physical link to MIT, three years after she graduated. Despite accompanying me through the second half of my studies at MIT, she has decided to pursue a doctoral study of her own. I hope that I can be as much of a backing to Denise during her upcoming *Promotion* in Germany as she was to me.

This research was supported by the Air Force Office of Scientific Research grant AFOSR-90-0035, supervised by Major Daniel Fant as the Technical Monitor.

Contents

List of Figures

List of Tables

Nomenclature

Latin Symbols

a	speed of sound
b	real amplitude
c	blade chord or blade axial chord
c_a	blade axial chord
c_p	specific heat at constant pressure
e	Euler's constant
e_t	total specific energy of a fluid, $e_t = h_t - (p/\rho)$
$\vec{e}_j$	j^{th} unit vector, $\vec{e}_j = [\delta_{1j}, \delta_{2j}, \delta_{3j}, \delta_{4j}]^T$
h_t	total specific enthalpy of a fluid
i	$\sqrt{-1}$
k	wave number,
	reduced frequencies, defined in equation (3.5) or (4.6)
l	length scale
$\overline{ke}$	temporal and spatial mean of the secondary kinetic energy
n_p	polytropic exponent
n	coordinate normal to a blade surface
p	pressure
q	heat
r	kinetic energy ratio, defined in equation (3.41)
s	entropy,
	blade surface coordinate
$\overline{s}$	nondimensional time-mean mass-average entropy, defined in (2.36)
t	time
u	velocity in the direction of the coordinate x or s
u_τ	wall friction velocity, defined in (4.89)
v	velocity in the direction of the coordinate y or n
$\vec{w}$	eigenvector
x	axial coordinate
$\acute{x}$	convected coordinate, in the mean flow direction
y	circumferential coordinate
$\acute{y}$	convected coordinate, normal to the mean flow
z	coordinate in the direction of wave propagation
A, B	matrices in the Euler equations in primitive form, defined in (2.5)
$\hat{A}, \hat{B}$	complex amplitudes of the potential functions (3.8) and (3.24)
D	matrix to calculate the second-order entropy rise in (2.36)
E	acoustic energy density, defined in equation (2.41)
F, G	flux vectors in the Euler equations, defined in equation (2.2)
H	matrix to calculate second-order mean flow changes in (2.30)
HFL	high-reduced-frequency limit

$\vec{I}$	acoustic intensity
N	acoustic energy flux defined in equation (2.41)
M	Mach number
P	pitch
$\acute{P}$	rotated pitch (in a convected coordinate system), $\acute{P} = P \cos \alpha$
P^*	pitch of the neighboring blade row in a single stage
Pr	Prandtl number
R	square root of the discriminant defined in (2.16), specific gas constant
$\mathbf{R}$	acoustical impedance
Re	Reynolds number
Re_s	Reynolds number defined with the local coordinate s
Re_θ	Reynolds number defined with the momentum thickness θ
S	entropy flux in subsection 2.3.2, $S = \rho u s$
T	period, characteristic time, temperature
T_f	forcing time scale (blade passing period or an integer fraction thereof)
U	state vector defined in equation (2.2) or (2.5)
U_e	freestream convection velocity
V_R	rotor speed

Greek Symbols

α	angle between the blade wake and the axial direction
β	inter-blade phase angle, amplitude attenuation factor
$\acute{\beta}$	inter-blade phase angle in a convected coordinate system
γ	ratio of specific heat for an ideal gas, vortex sheet strength
δ	boundary layer thickness
δ_f	unsteady boundary layer thickness
δ_l	laminar sublayer layer thickness in turbulent flow
δ_ν	viscous length scale
δ^*	displacement thickness
δ_{ij}	Kronecker delta function, defined in appendix C
ϵ	small (perturbation) parameter
ϵ_2, ϵ_4	second-difference and fourth-difference smoothing coefficients
η	efficiency
θ	angle between the wave propagation direction and the surface normal
κ	thermal conductivity
λ	a reduced frequency defined in equation (3.22)
λ_f	wavelength of a disturbance driving the unsteady boundary layer
μ	dynamic viscosity

ν	kinematic viscosity
π_t	total pressure ratio
ρ	density
σ	normal stress
τ	shear stress
τ_t	total temperature ratio
ϕ	potential function
φ	phase angle
ω	angular frequency
ω_f	forcing frequency, blade passing frequency
Γ	circulation
Δ	difference, small perturbation, grid spacing
Φ	dissipation function, first defined in equation (4.14)
Ω	reduced frequency defined in equation (2.11), control volume, volume of integration
$\mathrm{d}\Omega$	control volume boundary

Others

$\Re(\ ), \Im(\ )$	real and imaginary part of a complex quantity
∇	gradient operator

Subscripts

e	at the boundary layer edge
i	integrated, incoming
in	at the inflow boundary
inv	inviscid
l	left
m	mth spatial/temporal harmonic
n	nth temporal harmonic, in/normal to the direction of n
p	in primitive form, polytropic
o	fluid state after the dissipation of unsteady waves
out	at the outflow boundary
r	right, reflected, arbitrary reference state

s	isentropic, in/normal to the direction of s, based on the local value of the coordinate s
t	total/stagnation quantity, turbulent
u	velocity in the direction of the coordinate x or s
v	velocity in the direction of the coordinate y or n
vis	viscous
w	at the wall
x	in the direction of the coordinate x,
y	in the direction of the coordinate y
C	compression
D	design
E	expansion
HFL	high-reduced-frequency limit
R	rotor
S	stator
0	zeroth-order, mean state
1	first-order, first-order perturbation, entropy wave, fluid state before compression
2	second-order, second-order perturbation, vorticity wave, fluid state after compression
3	pressure wave propagating or decaying downstream, fluid state before expansion
4	pressure wave propagating or decaying upstream, fluid state after expansion
θ	based on the momentum thickness
∞	at infinity

Superscripts

T	transpose
$'$	quantity in a convected coordinate system
$\tilde{}$	unsteady quantity
$\hat{}$	complex amplitude
$\bar{}$	temporal mean, temporal and spatial mean
$\vec{}$	vector quantity

Chapter 1
Introduction

Flow fields in turbomachinery are inherently unsteady, with a multitude of sources contributing. The incoming flow itself can be nonuniform resulting in an unsteady inflow to the rotor frame of reference. The relative motion of neighboring blade rows, in conjunction with the spatially nonuniform pressure fields locked to loaded blades, leads to an unsteady pressure distribution in both through so-called potential interaction. A blade row may also move through and interact with shock wave systems. Stator wakes convected with the mean flow cause unsteadiness in the rotor frame of reference. Similarly, secondary flow effects like horse shoe vortices, passage vortices, and tip clearance vortices contribute to flow unsteadiness. The viscous flow past a blunt turbine trailing edge results in vortex shedding; trailing-edge vortex shedding has also been found in compressors operating in the transonic or supersonic regime. Finally, there is unsteadiness induced by the motion of the blades themselves, i.e. blade flutter.

Very successful turbomachines have been developed in the past by compensating for the lack of basic knowledge about unsteady effects or for their neglect with extensive empirical correlations. The past two decades have seen a strong increase in the experimental and computational effort devoted to unsteady flows in turbomachinery. Partly, this increase was driven by a tremendous rise in the computing power and memory available and by new or improved experimental facilities and techniques. Partly, it was fueled by continuing demands to improve upon existing designs and design methodologies. To increase engine efficiencies and stability margins, to extent engine life-times, to reduce weight and size, and to cut development cost and time, it is imperative to study and understand unsteady flow phenomena. With turbomachinery efficiencies typically around 90%, there is room left for improvement but one needs to look at all sources of loss, including those considered too small or too difficult to treat before.

1.1 Motivation

Besides the general recognition of the importance of unsteady effects in turbomachinery, several specific factors motivated this thesis.

First among them is the continuing prevalence of steady tools for routine design purposes in industry. The standard aerodynamic design tools for turbomachinery are steady codes, both inviscid and viscous, and steady cascade experiments. Designing a single stage or blade row with steady-state tools amounts to placing the stator and rotor row infinitely far apart thus eliminating the effects of blade row interaction. Unsteadiness, however, contributes additional loss with non-zero time-mean[1]. First, most of the energy associated with the unsteady part of the flow field is not recovered; it will eventually be dissipated. Second, the interaction of unsteadiness with boundary layers and shock structures can trigger additional loss. In a steady viscous simulation, the effect of unsteadiness on the efficiency is not captured. An unsteady, nonlinear simulation is still prohibitively expensive for routine design purposes and will likely remain so in the foreseeable future, particularly for multistage turbomachinery. Testing of a stage or a whole turbine under unsteady operating conditions will remain impractical for routine design purposes. Therefore, the error in the predicted efficiency stemming from the neglect of unsteady effects needs to be assessed.

Recently, linear perturbation methods have received increased attention as alternatives to fully nonlinear, unsteady simulations. In linear CFD-codes, a nonlinear steady state is found and the unsteady flow field is superimposed as a small perturbation. Second-order terms, i.e. terms quadratic in unsteady quantities, are neglected since the perturbations are assumed to be small. Linear perturbation codes have been found to give accurate results up to a surprisingly high level of unsteadiness [1, 2] and will be more widely used in the future. Linear codes, like steady codes, cannot capture unsteady loss. The time-mean of the first-order unsteady dissipation is zero; only terms second-order in unsteady quantities have a non-zero time-mean.

[1] This is not meant to imply that an increased spacing increases the efficiency. See sections 1.2 and 2.7 for a further discussion of this point.

Most recently, CFD-codes have been developed which account for the second-order effect of unsteadiness on the time-mean flow. Work in this direction has been pursued by Adamczyk [3] and Giles [4]. In this context, the thesis research was intented to underscore, or not, the need to include these effects.

Fully nonlinear, unsteady, viscous CFD-codes are another tool to evaluate unsteady loss. However, the weakest point of any numerical simulation, steady or unsteady, remains the accurate prediction of heat loads and losses due to the unavailability of adequate turbulence and transition models. Thus, there is a need to examine the modeling accuracy of numerical simulations with respect to unsteady flow phenomena and unsteady losses. Throughout this thesis research, the CFD-code UNSFLO by Giles [5, 6, 7], and the visualization package VISUAL2 by Giles and Haimes [8] were used.

The turbomachinery community is moving towards the consensus that increased losses under unsteady operating conditions are primarily due to strongly nonlinear effects like the alteration of the boundary layer characteristics through their effect on transition [9], the variation of secondary flow generation in downstream blade passages, and their effect on separation or reattachment. Those effects are beyond the realm of the linear/quadratic approach taken in this thesis. Nevertheless, the magnitude of effects that can be treated in a linear framework, remains to be determined.

1.2 Unsteadiness and Loss — Historical Perspective

Theoretical and Experimental Work

Unsteadiness affects the efficiency of turbomachinery in a variety of ways. What follows is a necessarily incomplete list of subjects of past investigations.

One of the earliest investigations was done by Keller [10] in 1935, who considered the transfer of mean-flow energy to the unsteady flow field through shedding of vorticity in an incompressible flow. The vorticity is shed off the blade trailing edges in response

to circulation variations, and its kinetic energy cannot be recovered. Keller estimated the circulation amplitudes and concluded that the rate of energy transfer is equivalent to between 0.4% and 1% of the power delivered or consumed by the rotor. In 1955, Kemp and Sears [11] applied thin-airfoil theory developed earlier [12, 13, 14], and used in the approximate analysis of interference between blade rows [15], to calculate the circulation variations, the shed vorticity, and the associated kinetic energy. They arrived at the conclusion that the rate of energy transfer is, generally, much less than estimated by Keller. In 1973, Hawthorne [16], who used a lifting-line approach, found rates of energy transfer which are in line with those of Keller[10].

In 1970, Kerrebrock and Mikolajczak [17] advanced a wake transport model to explain experimentally observed stagnation temperature and pressure non-uniformities in the stator exit plane of a compressor stage and their effect on the performance. In 1984, Ng and Epstein [18] measured large total temperature and pressure fluctuations at three to four the times blade passing frequency in the rotor core flow of a compressor stage. They proposed a moving shock model coupled to shed wake vorticity to explain their origin and deduced the magnitude of the associated loss. The entropy rise due to a moving shock was found to lead to a 0.15% drop in the efficiency while the mixing-out of fluctuations led to a loss on the order of the wake loss. Additional losses were expected from the interaction of the shed vorticity with downstream shock structures. Experimental evidence for moving shocks in a compressor rotor has subsequently been found by Strazisar [19]; Hathaway et el. [20] found vortex shedding in a axial-flow fan. Owen [21] observed vortex shedding off a transonic compressor rotor in numerical simulations.

More than one source of unsteadiness affects the compressor performance upon variation of the blade row gaps; those include wake transport, potential interaction, and wake mixing, among others. In 1970, Smith [22] reported an efficiency increase of 1% for reduced gaps in an multistage compressor. Later, Mikolajczak [23] confirmed their findings, while experiments by Hetherington and Moritz [24] contradicted them; the above experiments suggest that choosing an aerodynamically optimal gap is not an easy task.

The first studies on the influence of unsteadiness on the profile loss and the efficiency in attached flows appeared in the late sixties and early seventies [25, 26, 27]. Obremski and Fejer [28], as well as Walker [29], observed early transition in unsteady flow, leading to a greater length of the blade surface being covered by turbulent flow. Pfeil et al. [30, 31] observed unsteady transition on a flat plate subject to periodic wake-type disturbances. The same transition mechanism was found in an axial-flow compressor by Evans [32], and in an axial-flow turbine by Dring et al. [33]. Hodson [9] investigated the effect of unsteady transition on a cascade and found an increase of 50% in the rotor profile loss for unsteady inflow; subsequently he proposed an unsteady transition model [34]. Shock-wave/boundary layer interaction can lead to separation, as observed by Doorly and Oldfield [35], for example.

Numerical Developments

The progress in the numerical simulation of unsteady flow over the past two decades has been impressive. The range of methods includes linear potential [36, 37] and linear Euler methods [1, 2, 38], as well as nonlinear codes solving the Euler [5, 6, 39, 40, 41, 42, 43] or the Navier-Stokes equations [7, 44]. In linear (perturbation) methods, the steady flow is a solution to the nonlinear potential equation or to the nonlinear Euler equations, and the unsteady flow field is superimposed as a small perturbation. The appeal of linear methods lies in the savings in CPU-time they offer over a fully nonlinear formulation.

In response to the impracticality of multistage, unsteady, viscous simulations, Adamczyk [3] formulated a system of equations to account for the time-mean effect of the deterministic periodic unsteadiness on the mean flow through second-order terms similar to Reynolds stresses. In a research project related to this thesis, Giles [4] developed an asymptotic approach to unsteady flow in multistage turbomachinery. The asymptotic parameter is the level of unsteadiness in a flow described by the Euler equations. The approach leads to separate equations for the mean flow, the first-order perturbations, and the time-mean of the second-order perturbations. These can be solved more efficiently than the full nonlinear equations, in particular for multistage turbomachinery.

A number of comparisons have been conducted between experiments and simulations. Those were focusing, for example, on wake/stator interaction [5, 9, 42, 45], on the redistribution of inlet temperature profiles in a turbine stage [46, 47, 48, 49], on heat transfer in a turbine stage [50, 51, 52], or on the efficiency [53]. The weakest point of any numerical simulation remains, as was noted earlier, the exact prediction of heat loads and losses.

1.3 Thesis Outline

The first component of this thesis, chapter 2, focuses on the relation between unsteadiness and loss in two dimensions. The unsteady waves that are solutions to the linearized Euler equations are entropy and vorticity waves, convected with the mean flow, and pressure waves of propagating or evanescent nature. Concluding that most of the energy associated with the unsteadiness cannot be recovered, an asymptotic analysis in section 2.3 yields the second-order mean flow change and entropy rise resulting from the dissipation of an arbitrary combination of unsteady waves in a uniform mean flow. For the use in subsequent chapters, section 2.5 links the entropy rise to a total pressure loss and to a change in performance through a linearization of the isentropic efficiency. The result of the analysis is used in section 2.6 to evaluate the accuracy of the linear approach, and in section 2.7 to analyze mixing loss at the stator/rotor interface of a steady simulation.

The second component of this thesis focuses on the nature and the location of unsteady loss mechanisms and the magnitude of the associated losses. Two aspects are covered, termed Unsteady Circulation Loss and Unsteady Viscous Loss, respectively.

Chapter 3 revisits the Unsteady Circulation Loss first treated by Keller [10] in 1935 and later by Kemp and Sears [11] in 1956. Keller estimated the unsteady circulation amplitude to arrive at the kinetic energy in the unsteady flow field induced by the shed vorticity. Sears and Kemp used thin-airfoil theory to obtain the unsteady circulation amplitude. This approach, while enabling them to calculate the circulation amplitude,

limited them to incompressible flow and blades of zero thickness and camber with the mean flow nearly in the blade direction, i.e. lightly loaded blades. Thus, the airfoils are more representative of compressor blades than turbine blades. In this thesis, the circulation amplitudes are obtained from numerical simulations, which allows one to obtain amplitudes for arbitrary blade and stage geometries, steady lift distributions, and Mach numbers. Kelvin's Circulation Theorem, upon which Keller's work rests, is valid even in compressible flows, provided they are homentropic. Eliminating the need to estimate the circulation amplitudes or to deduce them from thin-airfoil theory, results in a realistic measure for the secondary kinetic energy in modern turbomachines and the loss associated with its dissipation.

The unsteady stator/rotor interaction can generate strong pressure waves. Unsteady Viscous Loss, considered in chapter 4, is a consequence of dissipation in unsteady boundary layers driven by these pressure waves. Using a linear approach and a near-wall approximation in the high-reduced-frequency limit, the streamwise momentum equation, driven by unsteady pressure gradients, yields the local velocity distribution in the laminar Stokes' sublayer. The driving pressure gradients are obtained from an unsteady simulation. In the high-frequency limit, the dissipation in unsteady boundary layers depends only on the unsteady shear. The associated entropy generation is integrated over a blade surface and related to a drop in the isentropic efficiency. The result of a numerical study to check the errors introduced by a departure from the high-frequency limit is presented in section 4.3. Section 4.4 applies the loss model to a transonic turbine stage and discusses the modeling accuracy of numerical simulations with respect to unsteady loss.

Chapter 5 summarizes the approaches taken and the results obtained in this thesis, and gives recommendations for future research on the topic of unsteady loss.

Chapter 2
Unsteadiness and Loss

The objective of this chapter is to establish, in a rigorous mathematical manner, a link between the dissipation of unsteadiness in a two-dimensional, inviscid, compressible flow and the efficiency of turbomachinery. The result will be used in the investigation of unsteady loss mechanisms in chapters 3 and 4, and in discussions of the numerical modeling accuracy.

The unsteady waves that are solutions to the linearized Euler equations in two dimensions are entropy and vorticity waves, convected with the mean flow, and pressure waves of propagating or evanescent nature. They are briefly (*re*)derived in section 2.1; this section closely follows [55]. Section 2.2 contains a brief survey of literature on wave transmission and reflection in turbomachines and takes a short look at the rectification of energy associated with unsteady waves.

A novel asymptotic analysis in section 2.3 links unsteady waves to the loss resulting from their dissipation in a uniform mean flow. In subsection 2.3.1, a mathematically rigorous flux-averaging procedure for an arbitrary unsteady flow relates the dissipation of unsteady waves to second-order mean-flow changes. Subsection 2.3.2, in turn, relates the change in the mean state vector to a time-mean mass-average entropy rise. It emphasizes the separate contributions from waves of different frequency, wavenumber and physical nature. Section 2.5 relates the entropy rise to an equivalent total pressure loss and to a change in the turbomachine performance through a linearization of the isentropic efficiency.

Section 2.6 looks at the accuracy of the second-order entropy rise calculated from the linear model by comparing it to the entropy rise calculated with a nonlinear approach. Section 2.7 contains the first application of a linear/quadratic model to the analysis of the interface treatment (the mixing loss) in steady rotor/stator interaction simulations.

2.1 Unsteady Modes

In the core flow, the inflow and outflow boundaries, and the gap between blade rows of a turbomachine, the Euler equations are sufficient to describe the fluid motion. They are usually expressed in a form based on the conservation of mass, momentum, and energy.

$$\frac{\partial U}{\partial t} + \frac{\partial F}{\partial x} + \frac{\partial G}{\partial y} = 0 \tag{2.1}$$

The state vector U and the flux vectors F and G are defined by

$$U = \begin{bmatrix} \rho \\ \rho u \\ \rho v \\ \rho e_t \end{bmatrix}, \quad F = \begin{bmatrix} \rho u \\ \rho u^2 + p \\ \rho uv \\ \rho u h_t \end{bmatrix}, \quad \text{and} \quad G = \begin{bmatrix} \rho v \\ \rho uv \\ \rho v^2 + p \\ \rho v h_t \end{bmatrix}. \tag{2.2}$$

The pressure is determined from

$$p = (\gamma - 1)\left[\rho e_t - \frac{1}{2}\rho\left(u^2 + v^2\right)\right], \tag{2.3}$$

where γ is the (constant) ratio of specific heats. Equation (2.3) can be used to eliminate the total energy per unit mass, e_t, and the stagnation enthalpy, $h_t = e_t + (p/\rho)$, from equations (2.1) to obtain the Euler equations in the so-called *primitive* form.

$$\frac{\partial U_p}{\partial t} + A\frac{\partial U_p}{\partial x} + B\frac{\partial U_p}{\partial y} = 0 \tag{2.4}$$

The primitive state vector U_p and the matrices A and B are defined by

$$U_p = \begin{bmatrix} \rho \\ u \\ v \\ p \end{bmatrix}, \quad A = \begin{bmatrix} u & \rho & 0 & 0 \\ 0 & u & 0 & 1/\rho \\ 0 & 0 & u & 0 \\ 0 & \gamma p & 0 & u \end{bmatrix}, \quad \text{and} \quad B = \begin{bmatrix} v & 0 & \rho & 0 \\ 0 & v & 0 & 0 \\ 0 & 0 & v & 1/\rho \\ 0 & 0 & \gamma p & v \end{bmatrix}. \tag{2.5}$$

Equations (2.4) are still nonlinear; they are linearized by considering small perturbations ϵU_1 of the primitive flow vector from a spatially uniform, steady (mean) flow U_0.

$$U_p = U_0 + \epsilon U_1(x, y, t) + \ldots \tag{2.6}$$

Since the character of the flow depends on the mean Mach number $M_{x,0}$, it is advantageous to nondimensionalize the mean flow and the unsteady perturbations by the mean

density ρ_0 and the mean speed of sound a_0. The first-order perturbations of the Euler equations (2.4) are

$$\frac{1}{a_0}\frac{\partial U_1}{\partial t} + A_0\frac{\partial U_1}{\partial x} + B_0\frac{\partial U_1}{\partial y} = 0, \tag{2.7}$$

with U_1, A_0, and B_0 defined by

$$U_1 = \begin{bmatrix} \rho_1 \\ u_1 \\ v_1 \\ p_1 \end{bmatrix}, \quad A_0 = \begin{bmatrix} M_{x,0} & 1 & 0 & 0 \\ 0 & M_{x,0} & 0 & 1 \\ 0 & 0 & M_{x,0} & 0 \\ 0 & 1 & 0 & M_{x,0} \end{bmatrix},$$

$$\text{and} \quad B_0 = \begin{bmatrix} M_{y,0} & 0 & 1 & 0 \\ 0 & M_{y,0} & 0 & 0 \\ 0 & 0 & M_{y,0} & 1 \\ 0 & 0 & 1 & M_{y,0} \end{bmatrix}. \tag{2.8}$$

Searching for wave-type solutions

$$U_1(x,y,t) = \tilde{U}(x,y,t) = \vec{w}_r \exp\left\{i\left(k_x x + k_y y - \omega t\right)\right\} \tag{2.9}$$

to equation (2.7), one is led to

$$\left(-\Omega + A_0\frac{k_x}{k_y} + B_0\right)\vec{w}_r = 0, \tag{2.10}$$

where $\vec{w}_r$ is a right eigenvector; the reduced frequency Ω is defined as

$$\Omega = \frac{\omega}{a_0 k_y}. \tag{2.11}$$

From the definition of A_0 and B_0, the dispersion relation is found as

$$\left[\left(\frac{k_x}{k_y}M_{x,0} + M_{y,0} - \Omega\right)^2 - 1 - \frac{k_x^2}{k_y^2}\right]\left(\frac{k_x}{k_y}M_{x,0} + M_{y,0} - \Omega\right)^2 = 0. \tag{2.12}$$

With the reduced frequency Ω and the circumferential wavenumber k_y known, equation (2.12) may be solved for the axial wavenumbers k_x, i.e. the eigenvalues of equations (2.7). The corresponding right eigenvectors are determined from equation (2.10).

The first two eigenvectors correspond to the twofold eigenvalue

$$k_{x,1} = k_{x,2} = k_y \ \frac{\Omega - M_{y,0}}{M_{x,0}}. \tag{2.13}$$

The corresponding eigenvectors are not unique and are chosen as

$$\vec{w}_{r,1} = \begin{bmatrix} 1 \\ 0 \\ 0 \\ 0 \end{bmatrix} \quad \text{and} \quad \vec{w}_{r,2} = \begin{bmatrix} 0 \\ -M_{x,0} \\ \Omega - M_{y,0} \\ 0 \end{bmatrix}. \tag{2.14}$$

The first right eigenvector, with a perturbation in the density only, represents an entropy wave, while the second, with perturbations in the velocities only, represents a vorticity wave. Both are convected with the mean flow.

The third and fourth eigenvector correspond to the eigenvalues

$$k_{x,3/4} = k_y \ \frac{(\Omega - M_{y,0})(\pm R - M_{x,0})}{1 - M_{x,0}^2}, \tag{2.15}$$

where

$$R = \sqrt{1 - \frac{1 - M_{x,0}^2}{(\Omega - M_{y,0})^2}}. \tag{2.16}$$

For a negative discriminant of R, the root with the positive imaginary part is implied. The corresponding eigenvectors are

$$\vec{w}_{r,3/4} = \begin{bmatrix} -(\Omega - M_{y,0})(\pm M_{x,0} R - 1) \\ (\Omega - M_{y,0})(\pm R - M_{x,0}) \\ \left(1 - M_{x,0}^2\right) \\ -(\Omega - M_{y,0})(\pm M_{x,0} R - 1) \end{bmatrix}. \tag{2.17}$$

In axially subsonic flow ($|M_{x,0}|<1$), they represent (isentropic) evanescent pressure waves with amplitudes decaying axially upstream and downstream, if the reduced frequency falls in the range $\left(M_{y,0} - \sqrt{1 - M_{x,0}^2}\right) \leq \Omega \leq \left(M_{y,0} + \sqrt{1 - M_{x,0}^2}\right)$. The evanescent nature is due to the complex (conjugate) wavenumbers $k_{x,3}$ and $k_{x,4}$. Outside that range, the eigenvectors represent (isentropic,) propagating pressure waves. In axially supersonic flow ($|M_{x,0}| \geq 1$), both pressure waves are of propagating nature and will be traveling in the downstream direction. Details are found in [55].

2.2 Dissipation and Rectification

In section 2.1, the unsteady waves that are solutions to the linearized Euler equations have been briefly rederived. The unsteady waves generated by wake/blade row interaction, rotor/stator interaction, vortex shedding, or any of the other mechanisms described in the introduction, propagate and/or are convected through the blade rows of a turbomachine. Away from the blades, the Euler equations are sufficient to describe the convection and propagation of unsteady waves, even if their origin is viscous as is the case for blade wakes or the vorticity shed off a blunt turbine trailing edge. The amplitudes of the unsteadiness in a turbomachinery environment can be quite large, in particular in the presence of viscous wakes and shock waves. Wakes are decomposed into vorticity and entropy waves while the weak shock waves can be modeled as isentropic pressure waves.

Unsteady waves in a turbomachine will undergo one of the following processes:

- Rectification
- Laminar or turbulent dissipation (in the blade passage or in boundary layers)
- Radiation out of the turbomachine upstream of the first row in an unchoked turbomachine
- Outflow or radiation out of the turbomachine downstream of the last blade row
- Acoustic transmission to the environment through the structure
- Dissipation through structural damping

Rectification denotes the recovery of energy associated with unsteady waves through its transfer to the mean flow. The effect of acoustic transmission and structural damping (an important player in the phenomena of flutter and forced response) cannot easily be quantified; they are not considered here. In multistage turbomachines one would expect the outflow/radiation at the inlet or the outlet to play a minor role only. In single-stage turbomachines, energy associated with unsteady waves is convected or radiated out and eventually dissipated. For multistage turbomachines, this leaves viscous dissipation in

the blade passage, the gap, and in unsteady boundary layers at blade, hub and tip as primary loss mechanisms.

Excluding the extraction of extra energy from the mean flow by unsteady waves, there are three questions about the effect of unsteadiness on the efficiency of turbomachinery. First, there is the question as to what percentage of the energy associated with unsteadiness is lost and what percentage is rectified. The second question pertains to the loss mechanism and its locus, if rectification is not possible. The third question inquires about the associated loss. Subsection 2.2.1 will briefly touch on the issue of rectification while subsection 2.2.2 takes a short look at the literature on wave transmission and reflection to make a conclusion about the locus of dissipation.

2.2.1 Conditions and Mechanism for Rectification

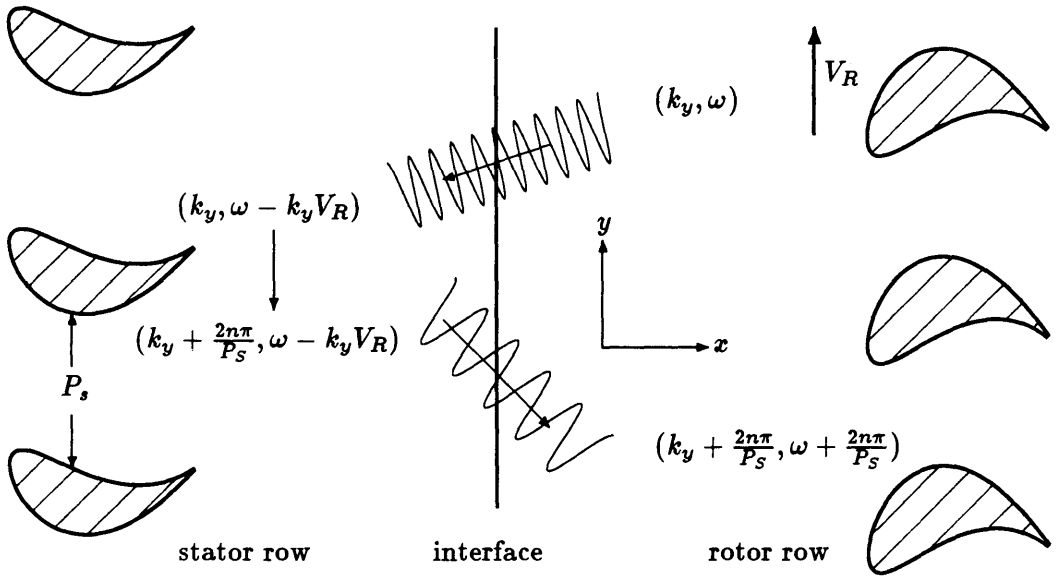

Figure 2.1: Rectification of unsteady waves

The energy associated with an unsteady wave can be rectified if the wave becomes steady in the rotor frame of reference. Figure 2.1 illustrates this process. An unsteady wave with normal wavenumber and frequency (k_y, ω) in the rotor frame crosses into the stator frame of reference. There, it is perceived as a wave with the same wavenumber but a different frequency due to the relative motion of the blade rows. Reflection at the stator blade row will give rise to waves of the same frequency but differing in their

wavenumbers by a term $(2\pi n/P_S)$, where P_S is the stator pitch. Crossing back into the stator frame of reference, they keep their wavenumbers but shift their frequencies to $(\omega+2\pi nV/P_S)$. If ω was the blade passing frequency, a harmonic thereof, or zero, in the first place, some of the reflected waves will be steady in the rotor frame of reference.

To recover the energy of a wave which is unsteady in the rotor frame and convert it into mechanical energy, the following conditions must hold:

- the circumferential wavelength must match the rotor pitch
- the axial wavelength must be large compared to the blade chord
- the inertial time scale of the rotor must be much less than the period of the unsteadiness

The first condition implies that the effect of a wave on different rotor blades in a row must be identical. Otherwise, the compound effect of the individual blade lift variations is zero; lift variations of different blades cancel. In practice, turbomachines never have identical rotor and stator pitches, making it impossible that the circumferential wavelength and the rotor pitch match. The second condition is of similar nature. If the wavelength is short compared to the blade chord, variations over different parts of a blade have a zero net effect on the blade lift. The third condition states that any lift circulations must be quasi-steady compared to the inertial time scale of the rotor. Otherwise, the rotor speed cannot follow lift variations and increase the mechanical energy delivered at the shaft. In turbomachines, the inertial time scale is much larger than the unsteady waves periods (which are linked to the blade passing frequencies and their harmonics), ruling out the rectification of waves which are unsteady in the rotor frame.

2.2.2 Wave Transmission and Reflection

Pressure waves encountering a blade row are partly transmitted and partly reflected. As a consequence of the Kutta condition, a vorticity wave is shed at the trailing edge of every blade. When a vorticity wave impinges upon the leading edge of a blade row, pressure waves are generated and another vorticity wave is shed at the trailing edge. Amiet [56] contains a good summary and a list of the related literature.

The amount of energy dissipated in the turbomachine and the location of its dissipation depend on the transmission and reflection characteristics of the blade rows with respect to the unsteady waves impinging upon them. The larger the reflection coefficients in a multistage turbomachine, the more likely it is that the waves are dissipated *in place*, i.e. in the gap between the blade rows or in unsteady boundary layers on the adjacent blade rows. Also, the larger the reflection coefficient of the blade rows, the larger is the probability that unsteady waves become steady in one frame of reference and are rectified. The larger the transmission coefficient, the more likely it is that they are radiated or convected out at the upstream or downstream end of the turbomachine.

Kaji and Okazaki [57, 58] made the most thorough study of this problems with a minimum number of limiting assumptions. In [57], they used a semi-actuator disk model to determine the transmission and reflection coefficients of a single blade row for a plane pressure wave or a vorticity wave impinging from upstream and for a plane pressure wave impinging from downstream. They examined the effects of mean-flow Mach number, wavelength, incidence angle, stagger angle, and steady aerodynamic blade loading. The Mach number and the incidence angle, combined with the stagger angle, were found to be the most important factors in determining the coefficients. High subsonic Mach number and angles of incidence far from the stagger angle substantially increased the reflection coefficients. The ratio of the wavelength of the incident wave to the blade chord had a minor effect only, especially at higher Mach numbers. The steady aerodynamic loading, i.e. the introduction of turning, was without substantial effect, its tendency being to increase the reflection coefficient and to eliminate cases of pure transmission or reflection. In a second paper [58], they used an acceleration potential method to clarify the effect of finite blade spacing; typically the longest wave in a turbomachine has a wavelength on the order of a blade chord or a blade pitch. It was found to be most significant at low Mach numbers and of secondary importance at high Mach numbers.

Muir [59] used an average-frequency approach, equivalent to the application of a delta-function of pressure to a blade row, to remove the wavenumber-dependence of transmission and reflection coefficients and extended the semi-actuator disk model to

three dimensions and cambered blades. The model is limited to circumferential wavelengths which are long compared to the blade spacing. The effect of three-dimensionality was found to be slight over the whole range of Mach numbers and cascade parameters.

Grooth [60] derived approximate expressions for the reflection coefficients of a semi-infinite flat plate cascade. The reflection coefficients model the effect of the neighboring blade row in a compressor and can be used to formulate reflecting boundary conditions in numerical simulations.

In all the references considered, the values of transmission and reflection coefficients varied greatly, depending on the exact choice of parameters like Mach number or angle of incidence and stagger. To draw a conclusion about the relative importance of transmission versus reflection, and ultimately about the locus of dissipation, these parameters would have to be known. None of the references treated camber angles close to those commonly found in turbines, nor did any of them consider the effect of blade-thickness. The results are therefore more relevant for compressors than for turbines. No clear general conclusion can be drawn about the reflection and transmission characteristics of blade rows in turbomachines; the exact amount of energy (associated with unsteady waves) rectified or dissipated, as well as the locus of dissipation, remain unknown.

2.3 Loss Due to Dissipation of Waves

The references on wave transmission and reflection examined in subsection 2.2.2 did not provide a clear picture of the relative importance of these phenomena or the applicability of the results to turbines. While some of the energy (associated with unsteady waves) can be recovered because they become steady upon changing the frame of reference, as illustrated in subsection 2.2.1, no quantitative assessment is available. The restrictive conditions placed on rectification suggest that little of this energy can be recovered.

If the energy of unsteady waves is simply lost (rather than causing extra unsteady losses), the level of loss still depends on the mean flow state at the locus of dissipation.

Part of the energy dissipated into heat at a pressure level above the exit pressure can be recovered in downstream blade rows. Downstream of a single-stage or a multistage turbomachine, the locus of dissipation and the mean flow state are obvious. In general, the locus of dissipation and the associated mean flow state are unknown.

Nevertheless, it is important to ask how an unsteady wave, or a combination thereof, contributes to the loss upon its dissipation in an arbitrary but uniform mean flow. Therefore, this section proceeds to investigate the dissipation of an arbitrary combination of unsteady waves in an arbitrary constant mean flow. The emphasis is on the final magnitude of the (mixing) loss as a result of complete spatial and temporal averaging of waves rather than its spatial evolution. By its nature, the result is directly applicable only to the generation of mixing loss downstream of the last blade row of a turbomachine and to the (unphysical) generation of loss at the interface in steady rotor/stator interaction simulations.

2.3.1 Flux-Averaging

A novel asymptotic approach and a control-volume argument are central to the analysis. Its aim is to link the dissipation of unsteady waves in a uniform mean flow to a measure of loss. Figure 2.2 serves to illustrate the idea.

At the right-hand side, the outflow boundary, the uniform and steady mean flow is described by the state vector in primitive form, U_0.

$$U_{p,out} = U_0 \tag{2.18}$$

At the left-hand side, the inflow boundary, the spatially and temporally varying flow enters the control volume. The flow there is described by

$$U_{p,in}(x, y, t) = U_0 + \Delta U(x, y, t). \tag{2.19}$$

The top and bottom surfaces are periodic boundaries. The perturbation ΔU is described

by an asymptotic expression in the small parameter ϵ.

$$\Delta U(x,y,t) = \epsilon U_1(x,y,t) + \epsilon^2 U_2(x,y,t) + \cdots \tag{2.20}$$

The first-order perturbations, $U_1(x,y,t)$, are assumed to consist of waves of the type given in section 2.1, equation (2.9). For the purposes of this chapter, it will suffice to include terms up to second order. In an ongoing research effort, to which this thesis is related, Giles [4] takes a similar asymptotic approach to the Euler equations for the simulation of unsteady flows through multistage turbomachinery.

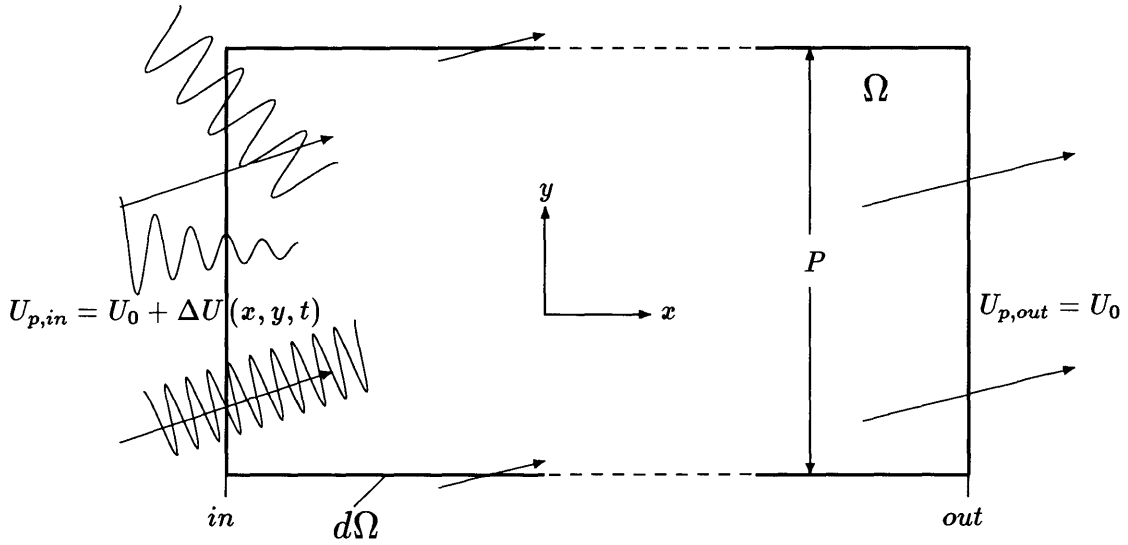

Figure 2.2: Control volume for the asymptotic analysis

The two-dimensional Euler equations in integral (conservation) form are

$$\frac{d}{dt}\int_\Omega U dA + \int_{d\Omega}(F dy + G dx) = 0. \tag{2.21}$$

Applying them to the control volume depicted in figure 2.2 and integrating over one fundamental period in time and space, one obtains the equations

$$\overline{F}_{out} = \overline{F}_{in}, \tag{2.22}$$

where $(\overline{*}) = \frac{1}{T}\int_0^T \left[\frac{1}{P}\int_0^P (*)dy\right] dt$ indicates the averaging operator. A formal Taylor

series expansion for the components of the flux vector, F_j, yields

$$F_j(U_0+\Delta U) = F_j(U_0) + \left.\frac{dF_j}{dU_p}\right|_{U_p=U_0} \Delta U + \frac{1}{2}\,\Delta U^T \left.\frac{d^2F_j}{dU_p^2}\right|_{U_p=U_0} \Delta U + \cdots \tag{2.23}$$

The second derivative of the flux vector, $\frac{d^2F}{dU^2}$, is a third-order tensor; the second derivative of a flux vector element F_j, $\frac{d^2F_j}{dU^2}$, can be expressed as a matrix, though. To check the derivatives, *Mathematica*®, a software package for performing symbolic mathematical manipulation by computer, was used. The first and second derivatives of the flux vector are defined in appendix A. Substituting the asymptotic expression (2.20) into (2.23), one obtains

$$\begin{aligned} F_j(U_0+\Delta U) = F_j(U_0) &+ \epsilon \left.\frac{dF_j}{dU_p}\right|_{U_p=U_0} U_1 \\ &+\epsilon^2 \left[\frac{1}{2}\,U_1^T \left.\frac{d^2F_j}{dU_p^2}\right|_{U_p=U_0} U_1 + \left.\frac{dF_j}{dU_p}\right|_{U_p=U_0} U_2\right] + \cdots \end{aligned} \tag{2.24}$$

Upon averaging, the second term on the right hand side of (2.24) vanishes because it varies harmonically in time and/or circumferentially; all that remains is

$$\overline{F}_j(U_0+\Delta U) = F_j(U_0) + \epsilon^2 \left[\frac{1}{2}\,\overline{U_1^T \left.\frac{d^2F_j}{dU_p^2}\right|_{U_p=U_0} U_1} + \left.\frac{dF_j}{dU_p}\right|_{U_p=U_0} \overline{U}_2\right] + \cdots \tag{2.25}$$

Equating fluxes as in (2.22), one obtains

$$\epsilon^2 \left[\frac{1}{2}\,\overline{U_1^T \left.\frac{d^2F_j}{dU_p^2}\right|_{U_p=U_0} U_1} + \left.\frac{dF_j}{dU_p}\right|_{U_p=U_0} \overline{U}_2\right] + \cdots = 0. \tag{2.26}$$

From (2.26), one can calculate $\overline{U}_2$, the time-mean part of U_2, by equating second-order terms. Again, *Mathematica*® was used; this time to solve the linear system of equations (2.26) for $\overline{U}_2$.

$$\overline{U}_2 = -\frac{1}{2}\left[\left.\frac{dF}{dU_p}\right|_{U_p=U_0}\right]^{-1} \sum_{j=1}^{4} \vec{e}_j\, \overline{U_1^T \left.\frac{d^2F_j}{dU_p^2}\right|_{U_p=U_0} U_1} \tag{2.27}$$

The vector $\vec{e}_j$ is the jth unit (column) vector with a non-zero entry in the jth row. For a non-zero axial Mach number the inverse of $\frac{dF}{dU}$ always exists. Note that the Euler equations (2.21) have been integrated along the inlet and outlet boundaries in time and space. The incoming unsteadiness $U_1(x,y,t)$ is a superposition of waves of different

frequencies, wavenumbers, and physical nature.

$$U_1 = \sum_m \sum_n \tilde{U}_{mn} = \sum_{l=1}^{4} \sum_m \sum_n b_{lmn} \vec{w}_{r,lmn} \exp\left\{i\left(k_{x,lmn}x + k_{y,m}y - \omega_n t + \varphi_{lmn}\right)\right\} \quad (2.28)$$

The variable b denotes a real amplitude, and the variable φ a phase angle; $\vec{w}_{r,l}$ stands for the right eigenvectors defined in section 2.1. The real part is implied wherever complex quantities appear in place of physical variables. Due to the orthogonality properties of sines and cosines, listed in appendix C, the integration (or averaging) removes crosscoupling between modes of different circumferential wavenumbers $k_{y,m}$ or different frequencies ω_n. Thus, one can consider one circumferential wavenumber and one frequency at a time and use the principle of superposition to obtain $\overline{U}_2$.

$$\overline{U}_2 = -\frac{1}{2}\left[\left.\frac{dF}{dU_p}\right|_{U_p=U_0}\right]^{-1} \sum_j \vec{e}_j \sum_m \sum_n \overline{\tilde{U}_{mn}^T \left.\frac{d^2 F_j}{dU_p^2}\right|_{U_p=U_0} \tilde{U}_{mn}} \quad (2.29)$$

However, this does not remove crosscoupling between waves of different physical nature, like pressure waves and vorticity waves, with the same frequency and circumferential wavenumber. After all elements in equation (2.29) have been non-dimensionalized by the outflow density and speed of sound, it may alternatively be written in the form

$$\overline{U}_2 = \frac{1}{1 - M_{x,0}} \sum_j \vec{e}_j \sum_m \sum_n \overline{\tilde{U}_{mn}^T H_j \Big|_{U_p=U_0} \tilde{U}_{mn}}. \quad (2.30)$$

The matrices H_j are defined in appendix A.

At this point, it is appropriate to remark that $\overline{U}_{2,mn}$ is a periodic function of the axial location of the inflow boundary due to the superposition of waves of different physical nature which are contained in U_1, defined equation (2.28); the mean inflow state, $\overline{U}_{p,in} = U_0 + \overline{U}_2$, varies periodically in the axial direction. This holds true even though one only considers waves of one circumferential wavenumber and frequency.

If only one type of wave, for example a propagating pressure wave, is present, only the phase angles of the unsteady perturbations will vary with the axial location. When two or more waves are present, the amplitude as well as the phase of the compound perturbation can change with the axial location[1] Figure 2.3 illustrates this for pertur-

[1] An exception is an evanescent pressure wave for which the amplitude changes also.

bations in the axial velocity. The subscripts 1 to 4 refer to the eigenvectors $\vec{w}_{r,1}$ to $\vec{w}_{r,4}$ of section 2.1. The magnitude of the compound perturbation $\tilde{u}$ is different at x_{in} and $x_{in}+\Delta x$. Also, the change in phase for the compound velocity perturbation is different from the phase changes $\Delta\varphi_2$ and $\Delta\varphi_3$ of the individual perturbations. In general, the amplitude and phase changes with axial location are different for each element of the state vector perturbation $\tilde{U}_{mn}$.

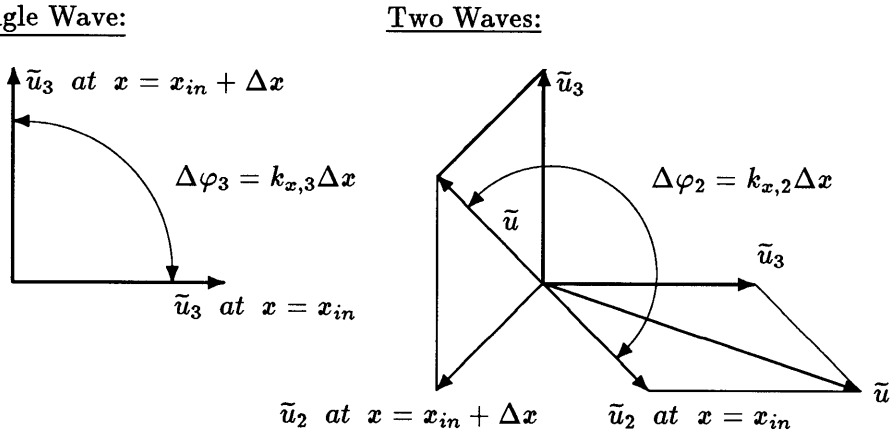

Figure 2.3: Compound phase and amplitude as a function of the axial position

Regardless of where the inviscid inflow boundary is located, one has to satisfy the equality of the average fluxes at inflow and outflow expressed in equation (2.22). This statement leads to equation (2.26), because the state U_0 is common to inflow and outflow. The first term in (2.26) contains time-means of products of perturbations in U_1; the time-mean of the product of two unsteady quantities, expressed in complex notation, is

$$\overline{\Re[b_1 \exp\{i\,(k_x x + k_y y - \omega t + \varphi_1)\}]\;\Re[b_2 \exp\{i\,(k_x x + k_y y - \omega t + \varphi_2)\}]} = \frac{1}{2}\,|b_1 b_2| \cos(\varphi_2 - \varphi_1), \quad (2.31)$$

where $\Re$ denotes the real part of a complex quantity and φ is a phase angle. The variables b_i denote constant and real amplitudes. The time-mean of the product of two unsteady quantities is a function of the axial location because the amplitudes and relative phases of its members change as the axial location of the boundary is changed. The second-order state vector perturbation with non-zero time-mean, $\overline{U}_2$, has to vary

axially to allow the equality of time-mean fluxes to be satisfied in the presence of first-order perturbations, U_1?

Again, waves of different frequency and/or circumferential wavenumber do not interact and influence the spatial distribution of the mean state $U_0+\overline{U}_2$. However, entropy, vorticity, and pressure waves of the same frequency and circumferential wavenumber have different axial wavenumbers k_x, the first two being convected with the flow and the latter two propagating with the speed of sound relative to the mean flow. Therefore, the phase angles and amplitudes implied in (2.30) will change with the axial location of the inflow boundary and so will $\overline{U}_2$. This is merely an artifact of the way the mean flow is represented, i.e. as a superposition of different physical modes. In [61], for example, Doak derives several, related partial differential equations illuminating how the contribution to the time mean energy flux $\overline{\rho u\,[u,v,w]}^T$ from fluctuating quantities changes in space in response to the presence of entropy, vorticity, and heat addition in a dissipative, conducting fluid.

2.3.2 Entropy Rise

Only the entropy is a measure of the irreversibilities in the flow. In inviscid, adiabatic flow, the substantial derivative of the specific entropy is zero.

$$\rho\frac{Ds}{Dt} = \rho\,\frac{\partial s}{\partial t} + \rho u\,\frac{\partial s}{\partial x} + \rho v\,\frac{\partial s}{\partial y} = 0. \tag{2.32}$$

With the help of the continuity equation, equation (2.32) can be rewritten as

$$\frac{\partial(\rho s)}{\partial t} + \frac{\partial(\rho u s)}{\partial x} + \frac{\partial(\rho v s)}{\partial y} = 0. \tag{2.33}$$

Averaging equation (2.33) in space and time leads to

$$\frac{\partial\overline{(\rho u s)}}{\partial x} = 0. \tag{2.34}$$

In an inviscid, adiabatic flow, the mean of the entropy flux $S{=}\rho u s$ is conserved in the axial direction. Note, that no such condition holds in unsteady, nonuniform flow for the

[2]The same holds true for a single evanescent pressure wave because the amplitude changes axially.

mean of the total pressure flux, $\overline{\rho u p_t}$. Analogous to equation (2.25), one can derive an equation for the entropy flux.

$$\overline{S}\left(U_0+\Delta U\right)=S\left(U_0\right)+\epsilon^2\left[\frac{1}{2}\overline{U_1^T\left.\frac{d^2S}{dU_p^2}\right|_{U_p=U_0}U_1}+\left.\frac{dS}{dU_p}\right|_{U_p=U_0}\overline{U}_2\right]+\cdots \tag{2.35}$$

The first and second derivatives of the entropy flux are defined in appendix B. Again, *Mathematica*® was used to check the derivatives. $\overline{U}_2$ is known from equation (2.30) and the mean change in the nondimensional specific entropy, $\overline{s}$, is given by

$$\Delta\overline{s}=\frac{(\rho us)_{out}-(\overline{\rho us})_{in}}{\rho_0 u_0 c_p}=\sum_m\sum_n\overline{\tilde{U}_{mn}^T D\tilde{U}_{mn}} \tag{2.36}$$

with the matrix D once more defined in appendix A. For physical insight, it is better to write $\Delta\overline{s}$ in explicit form. Equation (2.36) can be manipulated into the form

$$\Delta\overline{s}=\sum_m\sum_n\Delta\overline{s}_{mn}=\frac{1}{2}\sum_m\sum_n\left[(\gamma-1)\left(\overline{\tilde{u}^2}+\overline{\tilde{v}^2}+\overline{\tilde{p}^2}+2\frac{\overline{\tilde{p}\tilde{u}}}{M_{x,0}}\right)_{mn}+\overline{(\tilde{p}-\tilde{\rho})^2}_{mn}\right]. \tag{2.37}$$

Doak [61] derived a time-average entropy transport equation for a dissipative, conducting fluid. However, it does not show the final magnitude of the entropy increase after all fluctuations have been averaged out, nor does it single out contributions from waves of different physical nature.

Note that the entropy rise is invariant to a circumferential translation of the control volume. It seems that the time-mean increase in specific entropy between inflow and outflow, $\Delta\overline{s}$, varies axially with the location of the inflow boundary, if waves of different physical nature but the same circumferential wavenumber and frequency are present. The reasoning is the same as discussed in subsection 2.3.1; the phase relationships between the elements of the perturbation flow vectors $\tilde{U}_{mn}=[\tilde{\rho}\ \tilde{u}\ \tilde{v}\ \tilde{p}]_{mn}^T$ and their amplitudes are functions of the axial position. Physically, the entropy rise cannot depend on the location of the inflow boundary in an inviscid, non-conducting fluid. The location of the inlet boundary is arbitrary because there exists no mechanism of entropy generation; equation (2.34) confirms this notion and it can be shown that waves of different physical nature do not crosscouple in equation (2.37). The term 'crosscoupling' in the present context refers to the occurrence of mixed terms like $\overline{\tilde{u}_2\tilde{u}_3}$ or $\overline{\tilde{p}_3\tilde{u}_2}$

in equation (2.37). The time-mean of such crosscoupling terms depends on the axial location since the phase angle between the components varies with the axial location as a consequence of differing axial wavenumbers k_x.[3] The sum of the time-means of all crosscoupling terms between any two waves of different physical nature, however, is zero.

The following statements can be shown to hold:

- No crosscoupling between entropy, vorticity, and pressure waves (of propagating or evanescent nature) occurs in the flux-averaging process
- No crosscoupling exists between two propagating pressure waves, i.e. for real wavenumbers $k_{x,3mn}$ and $k_{x,4mn}$
- A single evanescent pressure wave, decaying upstream or downstream, does not lead to an increase in entropy upon flux-averaging
- If both evanescent pressure waves are present, they cause a uniform shift in entropy under the flux-averaging procedure (ill-posed problem)

Therefore, the entropy rise Δs_{mn} in the streamflux-averaging procedure can be calculated wave by wave and summed subsequently, as was the case for modes of different frequencies and/or circumferential wave numbers.

It is laborious but straightforward to prove the first statement by expressing the primitive variables in (2.37) as superpositions of contributions from the four physical modes with arbitrary amplitudes and phase relations between them. It is easy to see that entropy waves decouple in (2.37). The last term on the right hand side, the only place where entropy perturbations enter, is non-zero only for entropy waves and reduces to $(\overline{\tilde{\rho}^2}_1/2)$. The remaining proofs are presented in appendices D and E.

A single evanescent pressure wave, referred to in the third statement, is of importance in steady stator/rotor interaction simulations. There, the nonuniform stator outflow is averaged to provide uniform rotor inflow conditions while conserving mass, momentum,

[3] An exception is the case of two evanescent waves with conjugate complex axial wavenumbers.

and energy across the interface; this approach amounts to placing rotor and stator infinitely far apart and dissipating the unsteadiness between stator outflow boundary and rotor inflow boundary. Other approaches are possible but they are non-conservative and defy physical interpretation. If such a conservative averaging approach is used, the potential field of the upstream stator row does not lead to an entropy increase (mixing loss) at the interface; the subject will be discussed in detail in section 2.7. The proof is in appendix F. The third statement is of also of importance in the calculation of the efficiency which can include mixing losses downstream of the last stage. If the averaging is performed within the potential field of the last blade row, it will not affect the mixing loss.

In the presence of an entropy wave, a vorticity wave, and both propagating pressure waves, the entropy rise can be rewritten in terms of individual waves as

$$\Delta\bar{s}_{mn} = \underbrace{\frac{\overline{\bar{\rho}^2}_{1,mn}}{2}}_{\textit{entropy wave}} + \underbrace{\frac{\gamma-1}{2}\left(\overline{\bar{u}^2}_2 + \overline{\bar{v}^2}_2\right)_{mn}}_{\textit{vorticity wave}} +$$

$$+\frac{\gamma-1}{2}\left[\underbrace{\left(\overline{\bar{u}^2}_3+\overline{\bar{v}^2}_3+\overline{\bar{p}^2}_3+2\frac{\overline{\bar{p}_3\bar{u}_3}}{M_{x,0}}\right)_{mn}}_{\textit{pressure wave propagating downstream}} + \underbrace{\left(\overline{\bar{u}^2}_4+\overline{\bar{v}^2}_4+\overline{\bar{p}^2}_4+2\frac{\overline{\bar{p}_4\bar{u}_4}}{M_{x,0}}\right)_{mn}}_{\textit{... propagating up/downstream}}\right]. \quad (2.38)$$

For single evanescent pressure waves, the last two terms vanish (see appendix F).

2.3.3 Interpretation of the Entropy Rise

Entropy and Vorticity Waves

The first term on the right hand side of (2.38) represents the entropy increase through mixing-out of density (temperature) variations associated with entropy waves. The second term represents the effect of the averaging of velocity fluctuations associated with vorticity waves. This term's contribution to the entropy rise is related to the average kinetic energy per unit mass in a frame of reference convected with the mean

flow and is independent of the Mach number of the mean flow. It can also be derived from

$$\Delta\overline{s}_{2,mn} = \frac{\Delta\overline{q}}{c_p T_0}, \tag{2.39}$$

with the specific heat release $\Delta\overline{q}$ replaced by the average kinetic energy per unit mass in the convected frame. With $a_0^2=(\gamma-1)\,c_p T_0$, equation (2.39) can be manipulated into a form equivalent to (2.38).

$$\Delta\overline{s}_{2,mn} = (\gamma-1)\,\frac{\Delta\overline{q}}{a_0^2} = \frac{\gamma-1}{2}\left(\overline{\tilde{u}^2}_2 + \overline{\tilde{v}^2}_2\right)_{mn} \tag{2.40}$$

Propagating Pressure Waves

The pressure wave contributions on the right hand side of equation (2.38) are in terms of the axial component of the (nondimensional) acoustic energy flux, N_{mn}, originally put forward by Ryshov and Shefter [62]. Eversman [63] showed this energy flux and the corresponding acoustic energy density

$$E_{mn} = \frac{1}{2}\left(\overline{\tilde{p}^2}_3 + \overline{\tilde{u}^2}_3 + \overline{\tilde{v}^2}_3\right)_{mn}, \tag{2.41}$$

which is the sum of potential and kinetic energy, to be consistent with the energy equation in a uniform mean flow. In the limit of very high axial Mach numbers, the pressure waves are essentially convected with the mean flow and their main contribution to the entropy rise in (2.38) stems from the dissipation of their potential and kinetic energy. For small axial Mach numbers, the term containing a factor $1/M_{x,0}$, representing axial flux of acoustic energy across the inflow boundary of the control volume, dominates.

The interpretation of the pressure wave contributions depends on the axial Mach number $M_{x,0}$ of the mean flow. The first pressure wave, identified by a subscript 3, always propagates downstream and enters the control volume at the inflow boundary. So does the second pressure wave, identified by a subscript 4 and propagating against the mean flow, if the mean flow is axially supersonic ($M_{x,0}>1$).

In axially subsonic flow ($M_{x,0}<1$), a situation can arise in which a pressure wave leaves the control volume at the upstream boundary, the inflow boundary of the mean

flow. Since, by the way of the problem definition, no wave enters at the downstream boundary, a wave leaving the control volume at the inflow boundary leads to difficulties in interpretation, and it makes a negative contribution to the entropy rise.

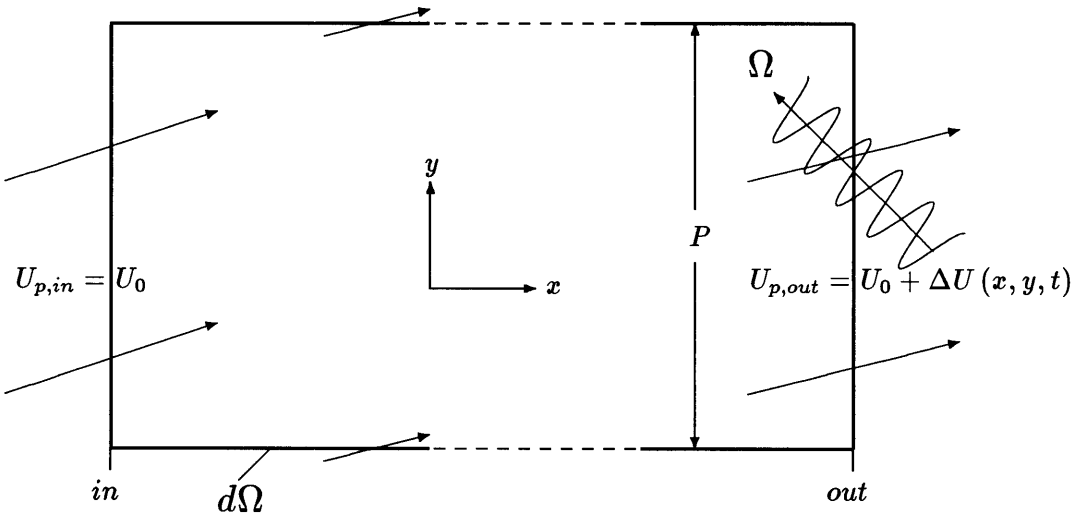

Figure 2.4: Control volume — revisited for propagating pressure waves

There are two ways to interpret this contribution. The first is to view this wave as a reflected wave, in which case a corresponding downstream propagating wave must also be present at the inflow boundary. Its negative contribution to the entropy rise reflects the fact that not all of the incoming wave is dissipated. The second way is to reformulate the problem, as is illustrated in figure 2.4. The flow is now uniform at the inflow boundary and the unsteadiness enters at the outflow boundary. The entropy rise between the inflow boundary and the outflow boundary due to dissipation of an upstream propagating wave is now given by the negative of the second pressure wave contribution, identified by a subscript 4 in equation (2.38).

Evanescent Pressure Waves

For single evanescent pressure waves, the last two terms in equation (2.38) are zero. The simultaneous presence, however, of an evanescent pressure wave decaying upstream and an evanescent pressure wave decaying downstream leads to an entropy increase/decrease under the flux-averaging procedure. Details are found in appendix E.

While the last two terms of equation (2.38) are still zero, there is a non-zero contribution from crosscoupling terms in equation (2.37).

$$\Delta\overline{s}_{mn} = \frac{\gamma - 1}{2}\left(\overline{\tilde{u}_3\tilde{u}_4} + \overline{\tilde{v}_3\tilde{v}_4} + \overline{\tilde{p}_3\tilde{p}_4} + \frac{\overline{\tilde{p}_3\tilde{u}_4} + \overline{\tilde{p}_4\tilde{u}_3}}{M_{x,0}}\right)_{mn} \tag{2.42}$$

This entropy change through crosscoupling is (and has to be) independent of the axial location of the inflow boundary because the axial wavenumbers of the two waves are complex conjugates. Thus, the phase shift with axial location is identical for both waves, leaving the relative phase angle between the waves constant. The product of the two amplitudes remains constant because, the waves decay/grow axially at the same rate. This result, however, is meaningless because the assumed mean flow state U_0 does not exist.

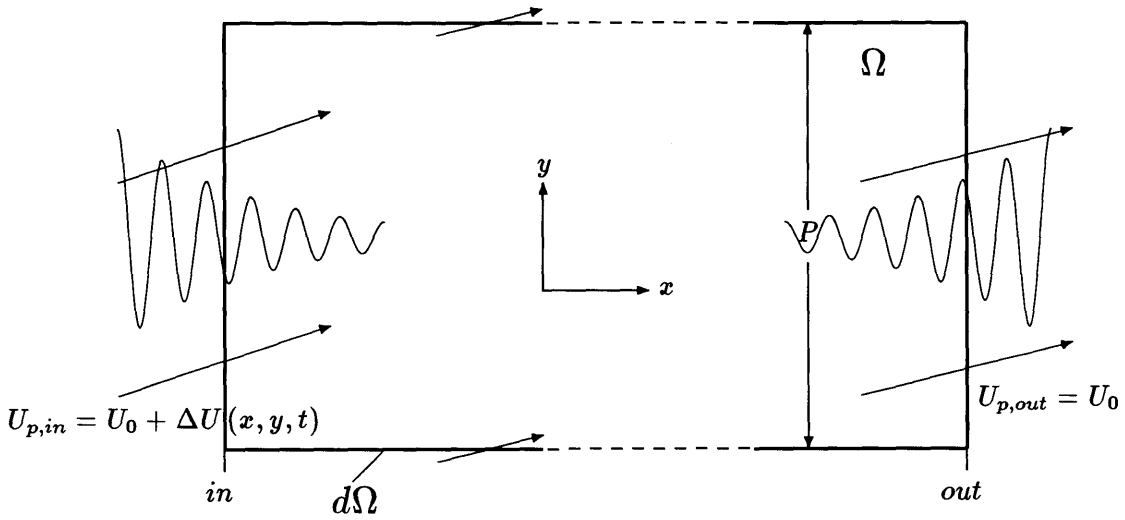

Figure 2.5: Control volume — revisited for evanescent pressure waves

2.4 A Note on Numerical Smoothing

The control-volume argument of subsection 2.3.1 and the derivation of the entropy rise in subsection 2.3.2 made no assumption other than the applicability of the linear regime and the conservation of the axial flux $\overline{F}$ defined in equation (2.2).

In particular, no assumption was made about the mechanism by which the flow is averaged out within the control volume. The results, equations (2.37) and (2.38), are valid for a physical flow averaged by the action of laminar or turbulent viscosity/conductivity and for a simulated flow averaged by the action of numerical smoothing[4].

Numerical smoothing is required to stabilize numerical simulations of the Euler equations. Fourth-difference smoothing dissipates high-wavenumber oscillations (with wavelengths on the order of the grid spacing Δ), which are solutions of the finite difference equations but not the partial differential equations. Second-difference smoothing is necessary to capture shock waves; it suppresses or limits overshoots and oscillations. Not all numerical methods explicitly add numerical smoothing. Those that do not, have it implicitly contained within their basic formulation, like McCormack's method [64].

As long as the basic formulation and the implementation of the numerical method and the numerical smoothing operators are conservative, the results (2.37) and (2.38) hold in a numerical simulation of the model problem depicted in figure 2.4.

In numerical simulations, the contributions of numerical smoothing to the fluxes (of mass, momentum, and energy) across the (inviscid) inflow and outflow boundaries are negligible. Thus, a simulation of a flow, in which unsteady waves are dissipated by way of numerical smoothing, must show the same entropy rise as the corresponding physical flow in which the unsteady waves are dissipated by the action of the laminar or turbulent viscosity/conductivity. This statement also holds in flows with a nonuniform, spatially varying mean state[5], which has important implications for the discussion of the numerical modeling accuracy in subsection 4.4.3.

[4] for a further discussion of numerical smoothing see subsections 4.4.3 and 4.4.4

[5] In this more general context, the results (2.37) and (2.38) do not apply, of course.

2.5 Efficiency Considerations

2.5.1 Total Pressure Loss

The effect of the averaging/dissipation on the isentropic or polytropic efficiency will be expressed in terms of a total pressure loss. The total pressure is defined by

$$p_t = p\left(1 + \frac{\gamma - 1}{2} M^2\right)^{\frac{\gamma}{\gamma - 1}}. \tag{2.43}$$

A change in specific entropy is related to changes in total pressure and temperature by

$$\frac{ds}{c_p} = \frac{dT_t}{T_{t,0}} - \frac{(\gamma - 1)}{\gamma} \frac{dp_t}{p_{t,0}}. \tag{2.44}$$

After multiplying both sides by (ρu), equation (2.44) may also be written in the form

$$\frac{d(\rho u s)}{c_p} = \frac{d(\rho u T_t)}{T_{t,0}} - \frac{(\gamma - 1)}{\gamma} \frac{d(\rho u p_t)}{p_{t,0}} + d(\rho u)\left(\frac{s}{c_p} - \frac{1}{\gamma}\right). \tag{2.45}$$

In steady, spatially uniform, and adiabatic flow, the first and the last term on the right hand side of equation (2.45) are zero due to conservation of energy and mass. Thus, the (flux-average) total pressure loss becomes

$$\frac{d(\rho u s)}{(\rho u)_0 c_p} = -\frac{(\gamma - 1)}{\gamma} \frac{d(\rho u p_t)}{(\rho u p_t)_0}. \tag{2.46}$$

Equation (2.46) is used to define an equivalent total pressure loss in (spatially) uniform and steady flow from the entropy rise $\Delta\overline{s}$ of subsection 2.3.1 resulting from the dissipation of unsteady waves.

$$\Delta\overline{p}_t = \frac{(\rho u p_t)_{out} - (\rho u p_t)_{in}}{(\rho u p_t)_0} = -\frac{\gamma}{\gamma - 1} \sum_m \sum_n \Delta\overline{s}_{mn} \tag{2.47}$$

2.5.2 Linearized Efficiency

The dissipation of energy associated with unsteady waves causes an entropy rise whose magnitude is given in equation (2.38). Equation (2.47), in turn, relates it to the equivalent total pressure loss that would be seen if this entropy rise (dissipation) had occurred in uniform, steady, and adiabatic flow. Neither the absolute magnitude of the rise in

entropy nor the absolute magnitude of the drop in total pressure are meaningful in turbomachinery; they must be compared to the entropy rise or total pressure drop through the stage or the turbomachine to obtain the effect on the performance.

Steady, Uniform Flow in a Turbine

The isentropic efficiency of a single stage (or a turbine) for steady, uniform inflow and outflow is defined by

$$\eta_{s,E} = \frac{\Delta h_t}{\Delta h_{t,s}} = \frac{h_{t,4o} - h_{t,3}}{h_{t,4s} - h_{t,3}}, \tag{2.48}$$

where the numerator represents the specific work extracted from a real engine while the denominator corresponds to the work extracted from an (ideal) isentropic engine. The subscripts 3, 4, and 4s refer to the initial and final states, i.e. before and after the isentropic or polytropic expansion in figure 2.6.

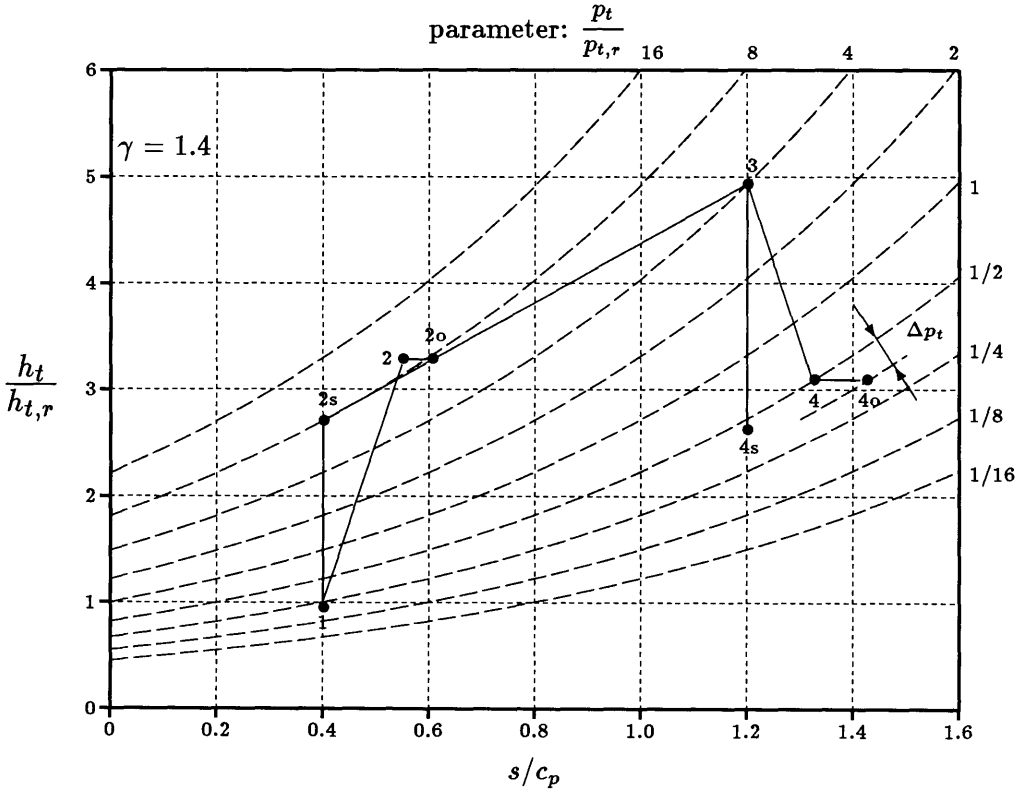

Figure 2.6: $h_t - s$ diagram for an ideal gas

For an ideal gas with constant specific heats, equation (2.48) may also be expressed as

$$\eta_{s,E} = \frac{1-\tau_t}{1-\pi_t^{\frac{\gamma-1}{\gamma}}} = \frac{1-\pi_t^{\frac{n_p-1}{n_p}}}{1-\pi_t^{\frac{\gamma-1}{\gamma}}}, \tag{2.49}$$

where π_t represents the total pressure ratio ($p_{t,4}/p_{t,3}$) and τ_t the total temperature ratio ($T_{t,4}/T_{t,3}$). The efficiency of a turbine is assessed by the isentropic efficiency; the efficiency of a single blade row or stage is given by the polytropic efficiency

$$\eta_{p,E} = \frac{\gamma}{\gamma-1}\frac{n_p-1}{n_p}. \tag{2.50}$$

The polytropic exponent n_p ($1 \leq n_p \leq \gamma$) is defined by

$$\frac{n_p-1}{n_p} = \frac{\ln(\tau_t)}{\ln(\pi_t)}. \tag{2.51}$$

For small total pressure ratios, the isentropic and the polytropic efficiency become equal.

The rotor operates with efficiency $\eta_{s,E,D}$ at the design point. The design point efficiency is here defined between the inflow state, point 3, and the outflow state after dissipation, point 4o. A Taylor series expansion around the design point yields the change in the isentropic efficiency due to a drop in total pressure and/or total temperature.

$$\eta_{s,E} = \eta_{s,E,D} + \left.\frac{\partial \eta_{s,E}}{\partial p_t}\right|_{\eta_{s,E}=\eta_{s,E,D}} \Delta p_t + \left.\frac{\partial \eta_{s,E}}{\partial \tau_t}\right|_{\eta_{s,E}=\eta_{s,E,D}} \Delta \tau_t + \cdots \tag{2.52}$$

$\Delta p_t = (p_{t,4o} - p_{t,4})/p_{t,4o}$ denotes the total pressure loss non-dimensionalized by the outlet total pressure. Assuming that dissipation downstream of the last rotor blade row leaves the total temperature unchanged, one obtains

$$\frac{\Delta\eta_{s,E}}{\eta_{s,E,D}} = \frac{\eta_{s,E}-\eta_{s,E,D}}{\eta_{s,E,D}} \approx \frac{\gamma-1}{\gamma}\frac{\pi_{t,D}^{\frac{\gamma-1}{\gamma}}}{1-\pi_{t,D}^{\frac{\gamma-1}{\gamma}}}\Delta p_t = -\frac{\pi_{t,D}^{\frac{\gamma-1}{\gamma}}}{1-\pi_{t,D}^{\frac{\gamma-1}{\gamma}}}\Delta\overline{s} \tag{2.53}$$

to first order. Equation (2.53) tells which part of the deviation of the isentropic efficiency from unity is due to the (adiabatic) dissipation (of unsteady waves) downstream of the outflow boundary. Figure 2.7 shows the relative drop in efficiency per unit total pressure loss as a function of the design total pressure ratio. The symbols in figure 2.7 denote turbine stages to be examined in chapters 3 and 4.

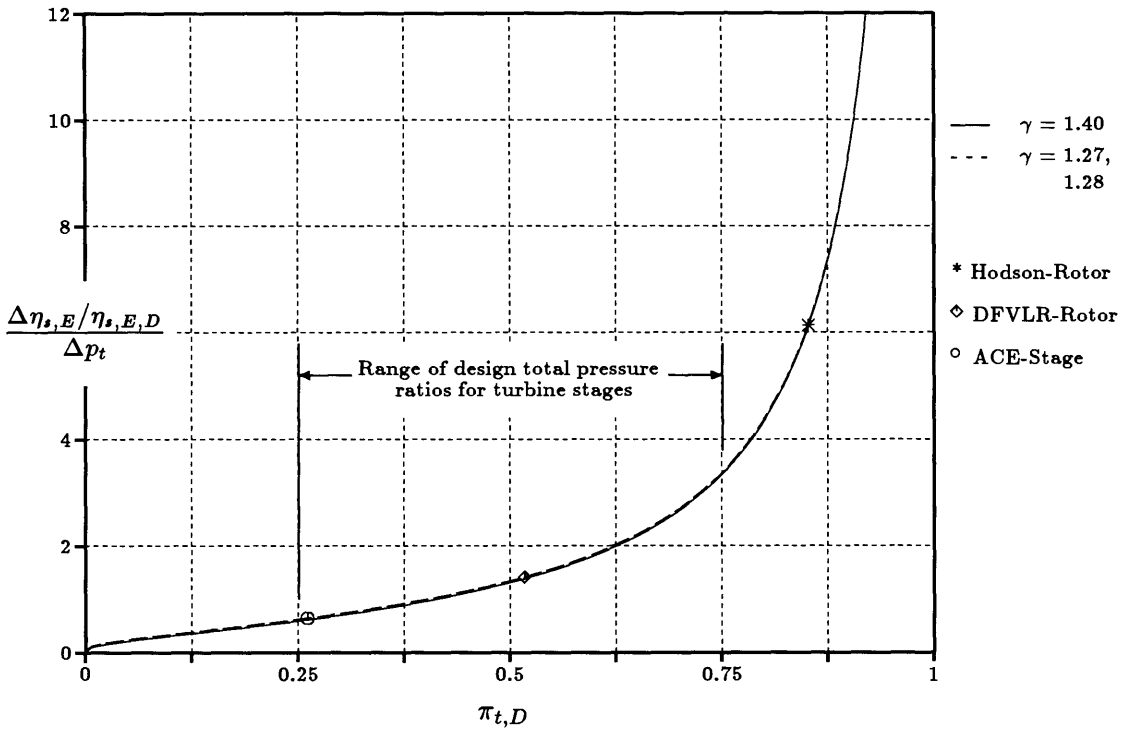

Figure 2.7: Total pressure loss and isentropic efficiency drop for a turbine

For the polytropic efficiency which is presented in figure 2.8, an identical approach gives the result

$$\frac{\Delta\eta_{p,E}}{\eta_{p,E,D}} \approx -\frac{\Delta p_t}{\ln(\pi_{t,D})}. \tag{2.54}$$

Most turbines stages are located between $0.25 < \pi_{t,D} < 0.75$, which translates into a (normalized) isentropic efficiency drop in the range of 0.6 to 3.3 times the (normalized) total pressure loss.

The same linearized approach to the efficiency was used by Cattafesta [65] to calculate the effect of experimental uncertainties in total temperature and pressure measurements and the ratio of specific heats on the measured stage performance.

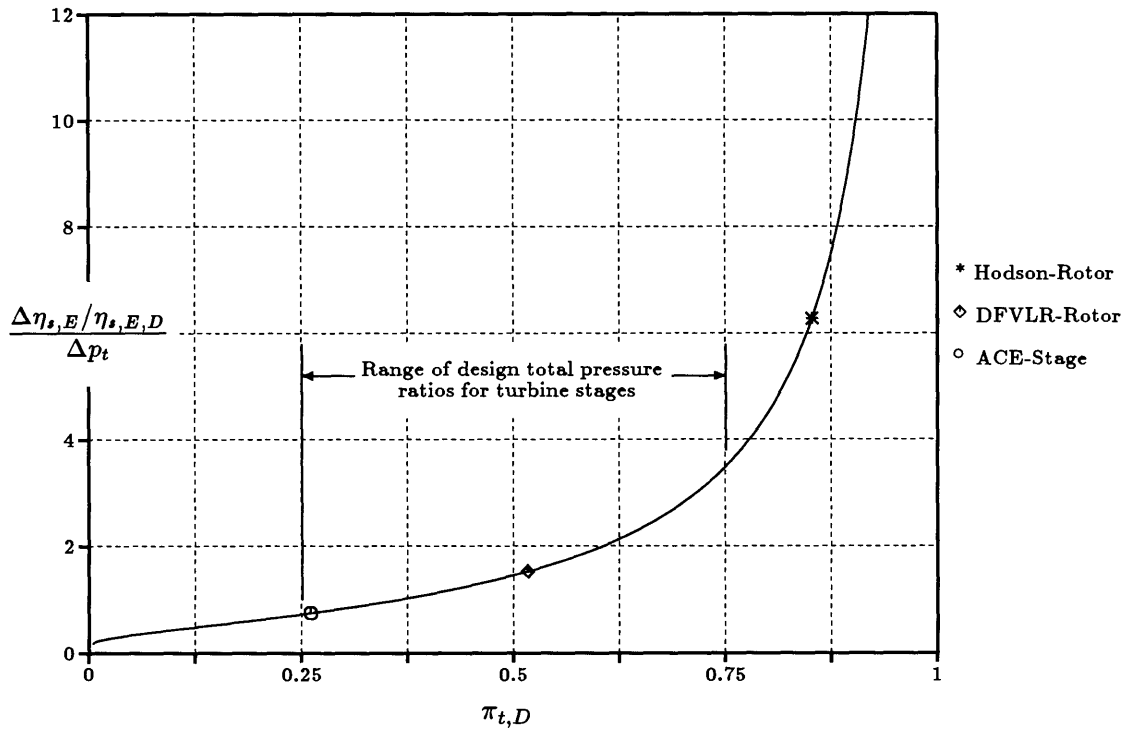

Figure 2.8: Total pressure loss and polytropic efficiency drop for a turbine

Steady, Uniform Flow in a Compressor

The corresponding result for steady, uniform flow through a compressor is easily derived as the analogue of the result for a turbine. The definition of the isentropic efficiency for a compressor is

$$\eta_{s,C} = \frac{(\rho u h_t)_{2s} - (\rho u h_t)_1}{(\rho u h_t)_{2o} - (\rho u h_t)_1}, \tag{2.55}$$

with the subscripts 1 and 2 corresponding to the states before and after compression. Proceeding as for the turbine, one obtains

$$\frac{\Delta\eta_{s,C}}{\eta_{s,C,D}} \approx -\frac{\pi_{t,D}^{\frac{\gamma-1}{\gamma}}}{\pi_{t,D}^{\frac{n_p-1}{n_p}} - 1}\,\Delta\bar{s} = \frac{\gamma-1}{\gamma}\,\frac{\pi_{t,D}^{\frac{\gamma-1}{\gamma}}}{\pi_{t,D}^{\frac{n_p-1}{n_p}} - 1}\,\Delta\bar{p}_t \tag{2.56}$$

to first order. Figure 2.9 shows the relative drop in the isentropic efficiency per unit total pressure loss in a compressor as a function of the design total pressure ratio.

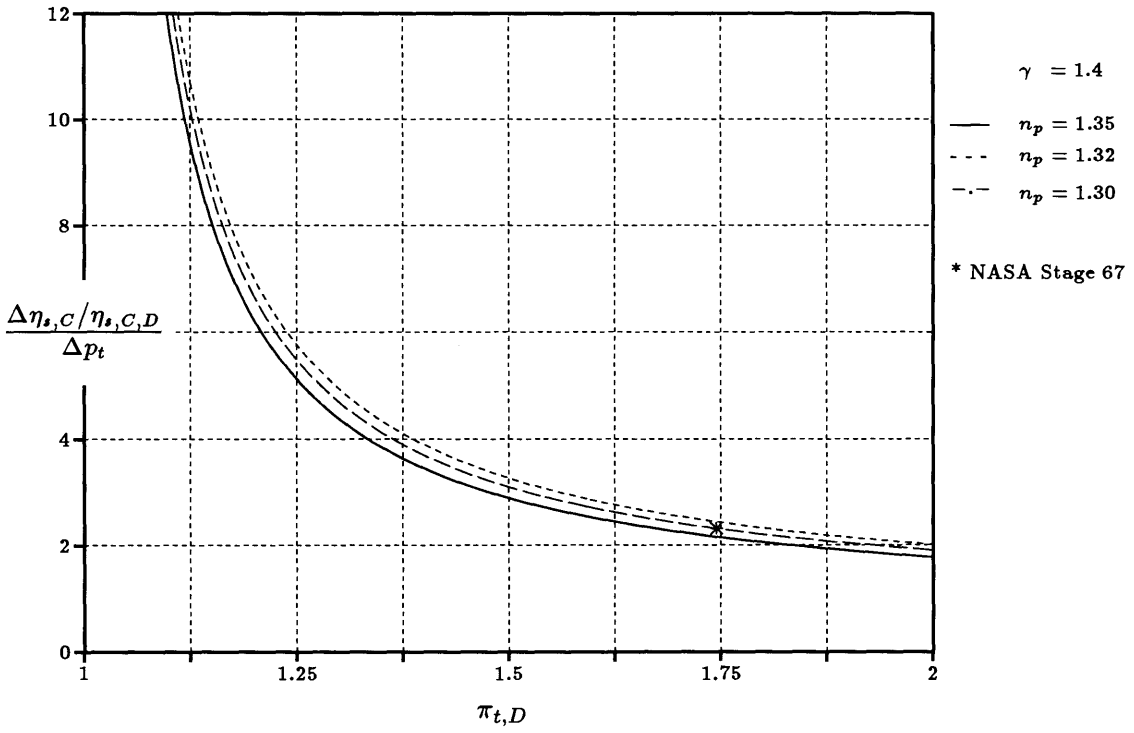

Figure 2.9: Total pressure loss and isentropic efficiency drop for a compressor

2.6 Numerical Check and Accuracy

In order to check the analytical results for the mean-flow change $\overline{U}_2$ (subsection 2.3.1) and the entropy rise (subsection 2.3.2), a code was written to simulate the problem illustrated in figure 2.2. The mean-flow change and the entropy rise were calculated using the linear/quadratic approach of section 2.3 and a fully nonlinear approach.

An arbitrary combination of unsteady waves of arbitrary amplitudes b_{lmn} and phases φ_{lmn} but the same reduced frequency Ω_{mn} was superimposed upon a uniform mean flow of arbitrary Mach numbers $M_{x,0}$ and $M_{y,0}$. The perturbations enter (or leave) the control volume at the left-hand boundary.

In the fully nonlinear approach, the vector sum of the density, velocity and pressure disturbances was taken to arrive at the compound vector of unsteadiness $\widetilde{U}_{mn}$, defined in equation (2.28). The resulting compound unsteadiness was used in an (adaptive)

integration via the Romberg method [66] to obtain the time-mean, space-average of the flux vector at the inflow boundary[6] A Newton-Raphson algorithm, using the first derivatives of the flux vector defined in appendix A, was employed to solve for the mixed-out state at the outflow boundary. The initial guess for the outflow state was the mean inflow state. Using the nonlinear definition

$$\frac{s - s_0}{c_p} = \frac{1}{\gamma} \ln\left(\frac{p}{p_0}\right) - \ln\left(\frac{\rho}{\rho_0}\right) \tag{2.57}$$

for the entropy, the time-mean, space-average of the entropy flux at the inflow boundary was calculated by Romberg integration. With the state at the outflow boundary known, the (nonlinear) entropy increase was calculated.

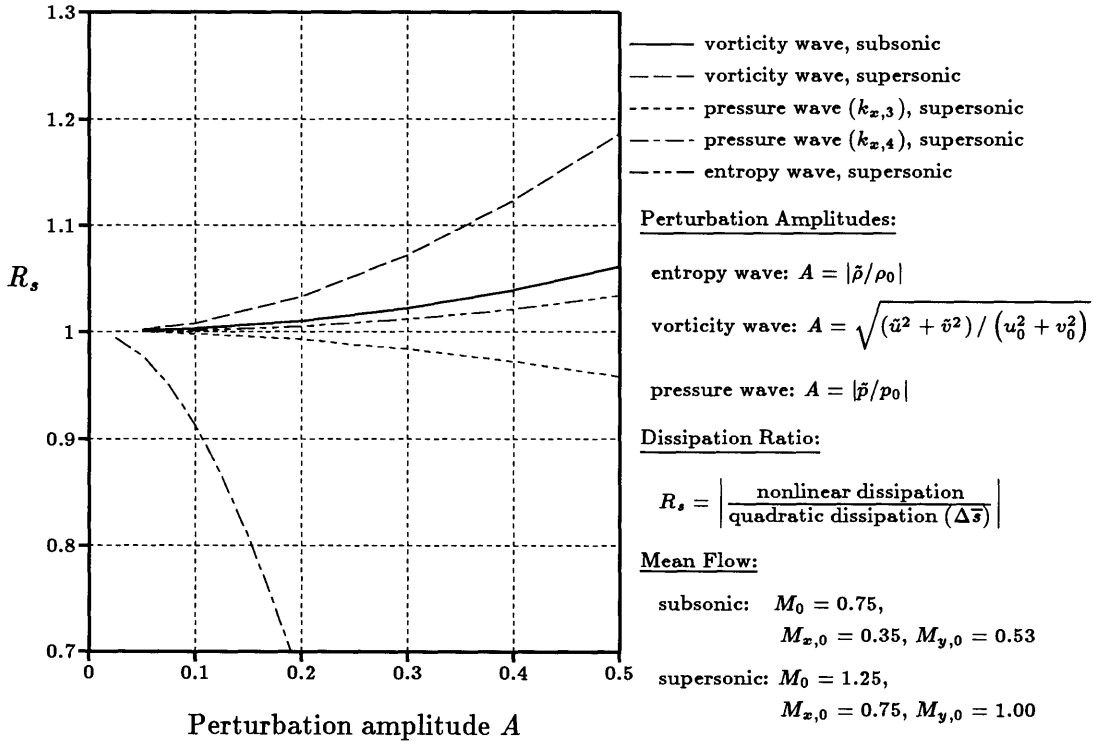

Figure 2.10: Accuracy of the second-order entropy rise ($\Omega = 0$)

In the linear approach, the mean-flow change $\overline{U}_{2,mn}$ was calculated according to equation (2.30) from the compound first-order disturbance vector $\widetilde{U}_{mn}$. The entropy rise Δs_{mn} was calculated from equation (2.37), which is in terms of the compound

[6] In contrast to figure 2.2 and equation (2.20), the second-order mean-flow change, $\Delta\overline{U}_{2,mn}$, was superimposed upon the flow at the outlet boundary.

disturbance vector, and from equation (2.38), which is in terms of the individual waves making up the disturbance vector.

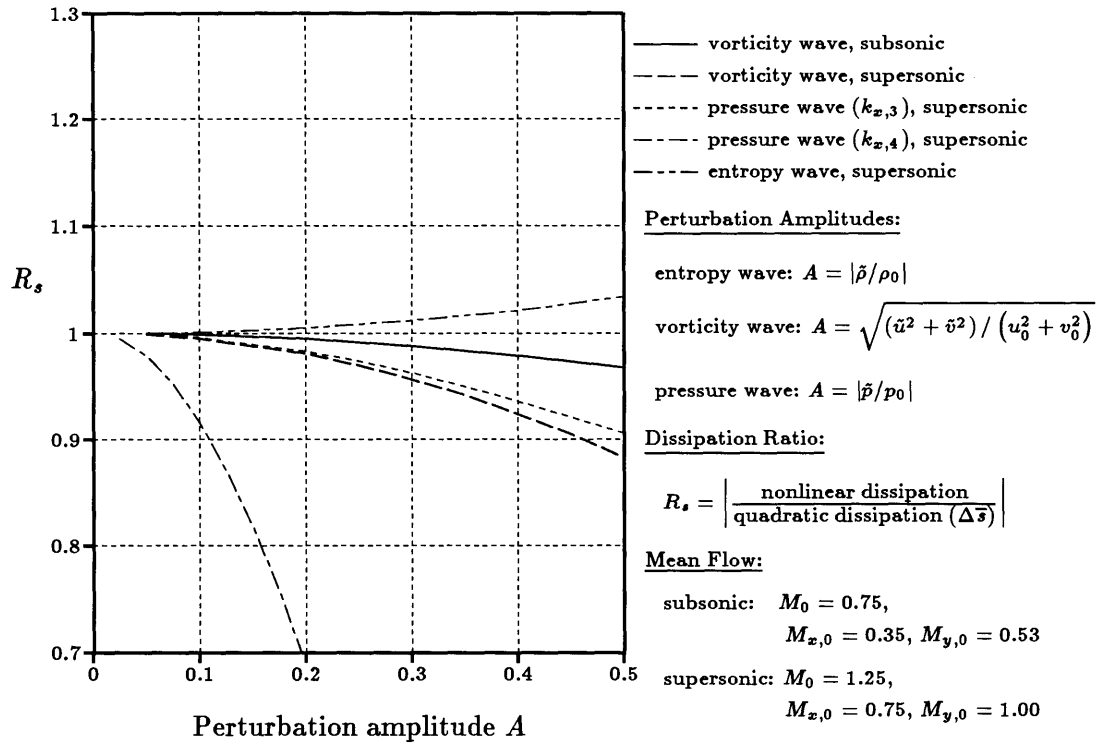

Figure 2.11: Accuracy of the second-order entropy rise ($\Omega = 4$)

Comparing the results from both approaches, the result for the mean-flow change (2.30) and the second-order entropy rise (2.37,2.38) were confirmed. For small wave amplitudes, the results from both approaches were identical regardless of the mean flow state and the composition of the disturbance vector. Since the mean flow-change is a vector quantity, it is difficult to present in a diagram. The entropy rise, however, is a scalar quantity and can easily be plotted. Figures 2.10 and 2.11 show the accuracy of the second-order entropy rise calculated from equation (2.38) versus the perturbation amplitudes of the disturbance for reduced frequencies of $\Omega = 0$ and $\Omega = 4$. The variable R_s is the ratio of the nonlinear entropy rise over the entropy rise calculated from equation (2.38). Only one disturbance, i.e. a single entropy wave, a single vorticity wave, or a single pressure wave, was entering (or leaving) the control volume in the cases presented in figures 2.10 and 2.11. In the most general case, the model has ten degrees of freedom. They are the mean Mach numbers $M_{x,0}$ and $M_{y,0}$, the reduced

frequency Ω, four perturbation amplitudes, and three relative phases. The choice of a single disturbance for figures 2.10 and 2.11 is (necessarily) arbitrary, but allows one to judge the degree of nonlinearity of the Euler equations and the range of applicability of the linear/quadratic analysis (if the accuracy requirement is known).

2.7 Mixing Loss at Steady Interfaces in CFD

The asymptotic analysis presented in section 2.3 can be used to investigate the mixing loss at a steady interface in a (viscous or inviscid) simulation. A viscous simulation of a highly loaded, transonic high-pressure turbine stage, called the ACE turbine stage, which has been tested at MIT [50] and Oxford University [52, 54], was chosen to illustrate the mixing loss. The simulation was performed with the CFD-code UNSFLO by Giles [5, 6, 7, 67]. In the freestream, it uses an explicit Lax-Wendroff scheme to solve the two-dimensional, unsteady (compressible) Euler equations on an unstructured grid composed of triangular or quadrilateral cells. Around the blades, it uses the Thin-Shear-Layer approximation of the Navier-Stokes equations to model viscous effects in boundary layers. Its quasi-3D capability allows it to account for a varying streamtube thickness; arbitrary pitch ratios can be handled with a time-inclined computational domain.

A detailed computational account of the (inviscid) stator/rotor interaction was presented by Giles [6]. Figure 2.12 shows the static pressure contours at a particular instant during an unsteady viscous simulation. In the unsteady simulation, the stator and the rotor row are separated by an axial gap of about 40% rotor axial chord. The outflow of both the rotor and the stator row are supersonic, producing weak oblique shocks at the trailing edges. An oblique shock wave, originating at the nozzle guide vane trailing edge, first hits the downstream rotor around the crown of the suction surface and is reflected from there. Subsequently, it moves forward to the leading edge with the reflected portion impinging on the adjacent pressure surface and being reflected to the suction surface, once more. Upon lifting off the rotor blade, the primary shock wave grows in length until the relative motion of the blade row causes it to strike the next rotor blade. In the meantime, its reflection off the rotor leading edge has impinged on and

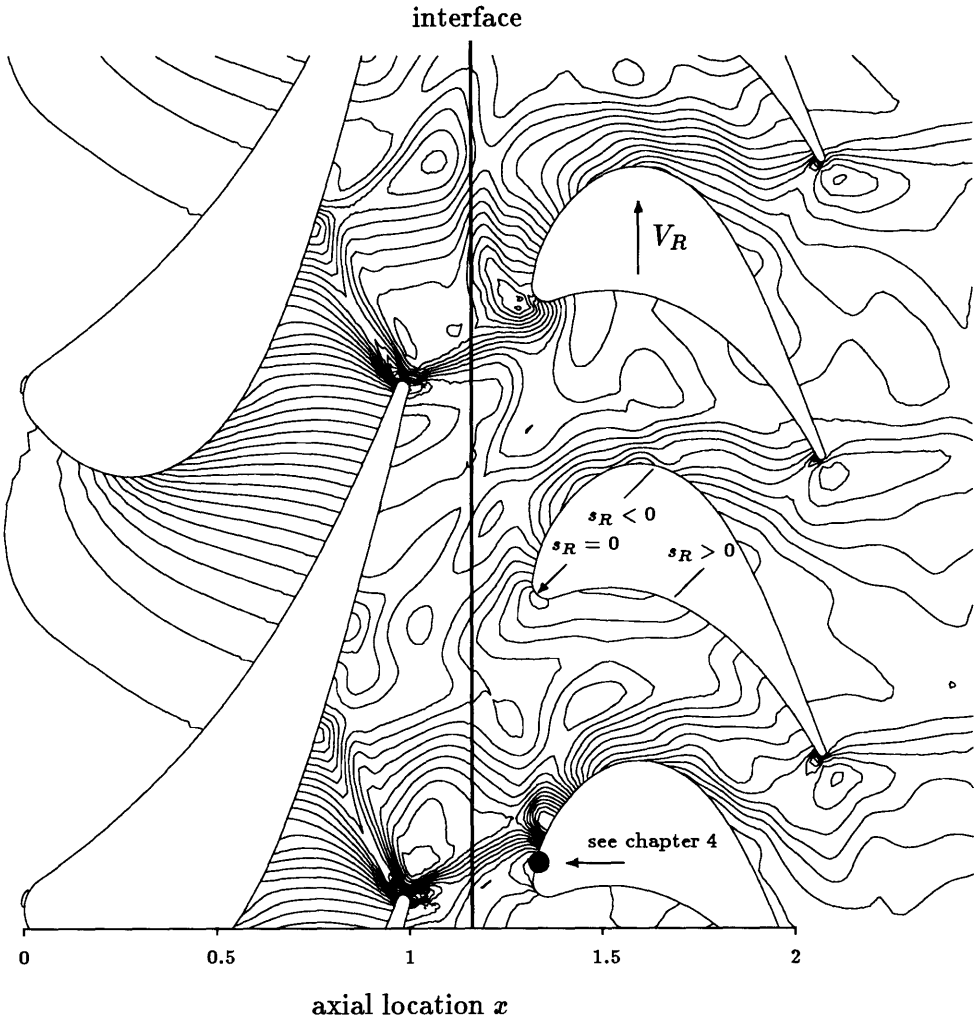

Figure 2.12: Static pressure contours in an unsteady simulation of the ACE turbine stage for $(t/T) = 0.7$

been reflected from the nozzle guide vane suction side. Comparatively large unsteady amplitudes are expected and have been found for this turbine stage [6].

While the flows in turbomachinery are inherently unsteady, steady simulations are often used for routine design purposes because they are easier to implement and less CPU-intensive than unsteady simulations. Also, a steady simulations is often performed to provide an initial condition from which to start an unsteady simulation. In a steady simulation, the axial fluxes of mass, momentum, and energy, defined in equation (2.18), are averaged at the stator outflow boundary to provide uniform and steady rotor inflow conditions. Other approaches are possible and are used in practice, but they are non-

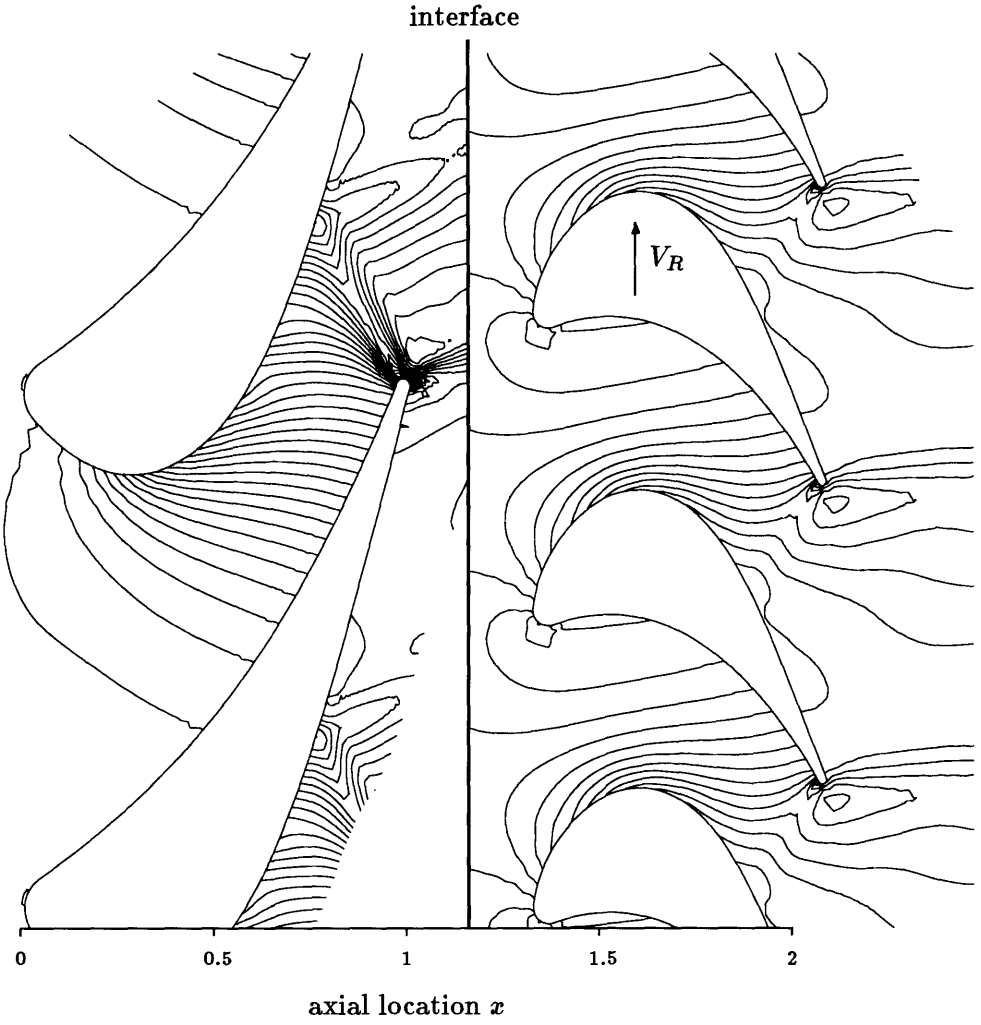

Figure 2.13: Static pressure contours in a steady simulation of the ACE turbine stage

conservative, (i.e. the fluxes are not conserved across the interface,) and defy physical interpretation. Figure 2.13 shows the static pressure contours during a steady simulation of the flow through the ACE turbine stage. The shock waves originating at the stator trailing edge are seen to vanish at the interface. There, outflow boundary conditions, based on a linearized model [55] as described in section 2.1, ensure that entropy waves, vorticity waves, and pressure waves leave the stator computational domain (almost) without reflections. Between the stator outflow and the rotor inflow boundary, the waves are mixed out to provide steady rotor inflow conditions. While the equations describing the mixing at the interface are nonlinear, the associated mixing loss can be analyzed and understood with the help of the linear model of section 2.3.

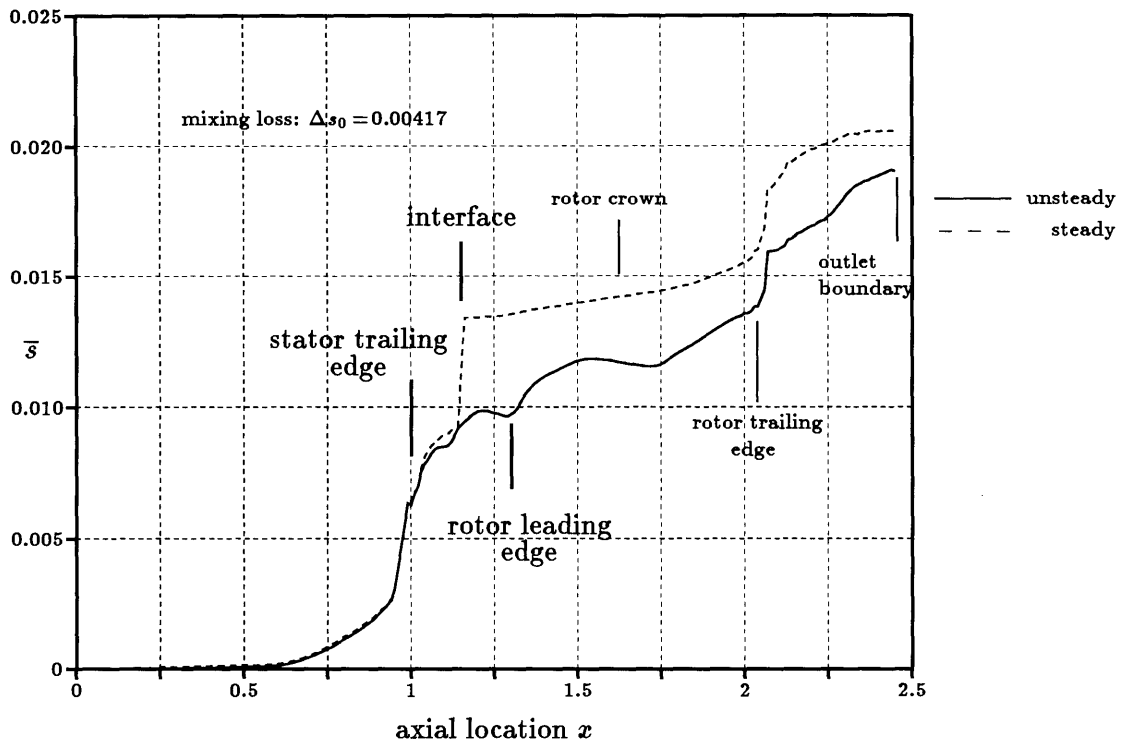

Figure 2.14: Entropy rise in the simulations of the ACE turbine stage

Figure 2.14 compares the time-mean mass-average of the specific entropy rise, $\Delta\bar{s}$, in a blade passage for a steady and an unsteady simulation of the flow through the ACE turbine stage. It is defined analogous to equation (2.36) as

$$\Delta\bar{s}(x) = \frac{\int_0^1 \left[\int_0^1 (\rho u s)|_x \; d(y/P)\right] d(t/T)}{c_p \int_0^1 \left[\int_0^1 (\rho u) \; d(y/P)\right] d(t/T)}. \tag{2.58}$$

The axial coordinate x has been non-dimensionalized by the stator axial chord. The stator leading edge is located at x=0, the trailing edge at x=1, as is shown in figures 2.12 and 2.13. The focus here is on the steady interface; other aspects of figure 2.14 are brought up later. Of the total entropy rise in a steady simulation, about 20% (equivalent to $\Delta\bar{s}$=0.00417) are caused by (nonphysical) mixing at the stator/rotor interface. However, the entropy rise beyond the interface is slower in the steady simulation because all waves that could cause unsteadiness and additional loss in the rotor frame have been dissipated at the interface already. As a consequence, the entropy rise through the stage remains only 8% higher in the steady simulation than in the unsteady simulation.

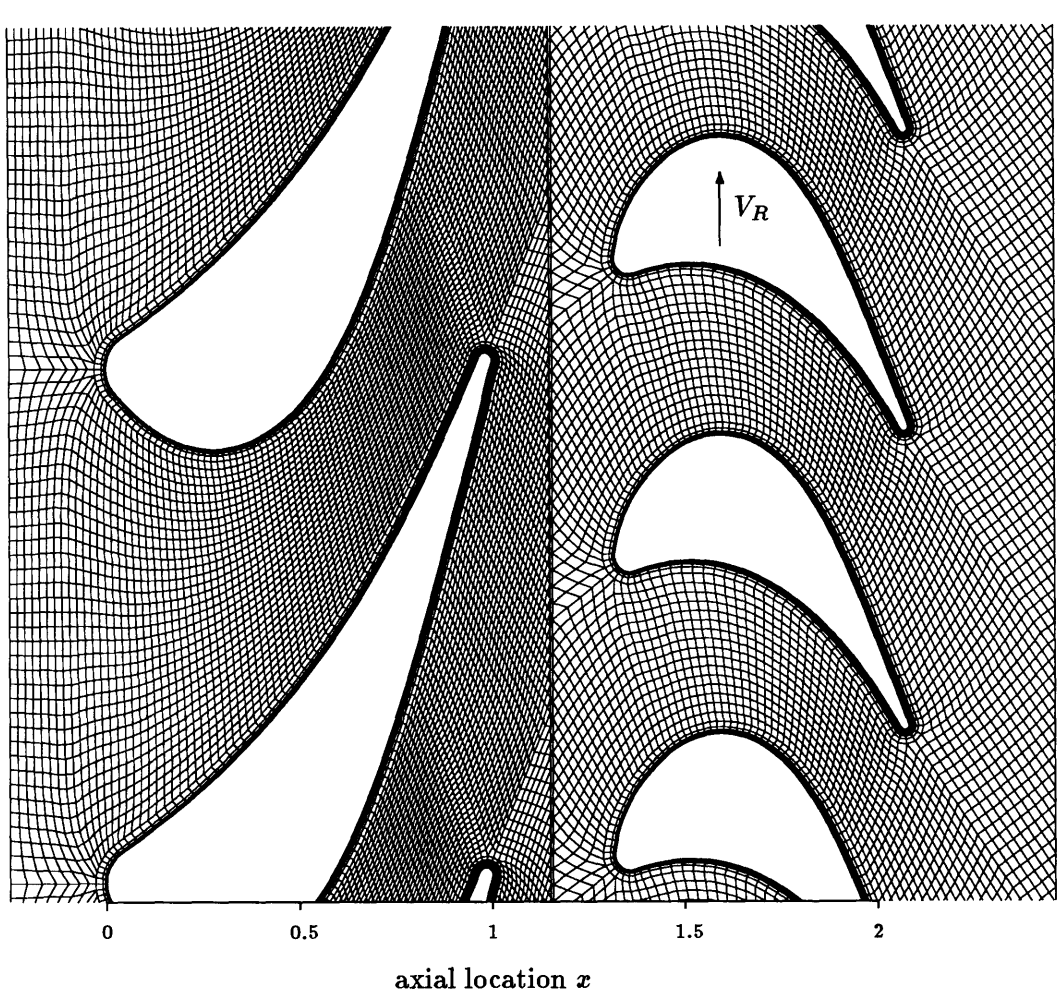

Figure 2.15: Stage geometry and computational grid of the ACE turbine stage for $(t/T) = 0.7$

The computational grid, see figure 2.15, along the stator outlet boundary (as well as the stator inlet, the rotor inlet, and the rotor outlet boundary) is equally-spaced. This facilitates the implementation of boundary conditions in a steady simulation and the transfer of information between the blade rows in an unsteady simulation. Due to the constant spacing, the nonuniform flow in a steady simulation can easily be decomposed into its spatial Fourier modes along the stator outflow boundary. With the Fourier modes known, the individual waves contained in these modes can be determined with the help of the left eigenvectors of the linearized Euler equations defined in appendix G. From the individual waves, the entropy rise (the mixing loss) at the interface can be

determined using equation (2.38). Figure 2.16 shows the contributions to the entropy rise of individual waves of different wavenumbers along the interface.

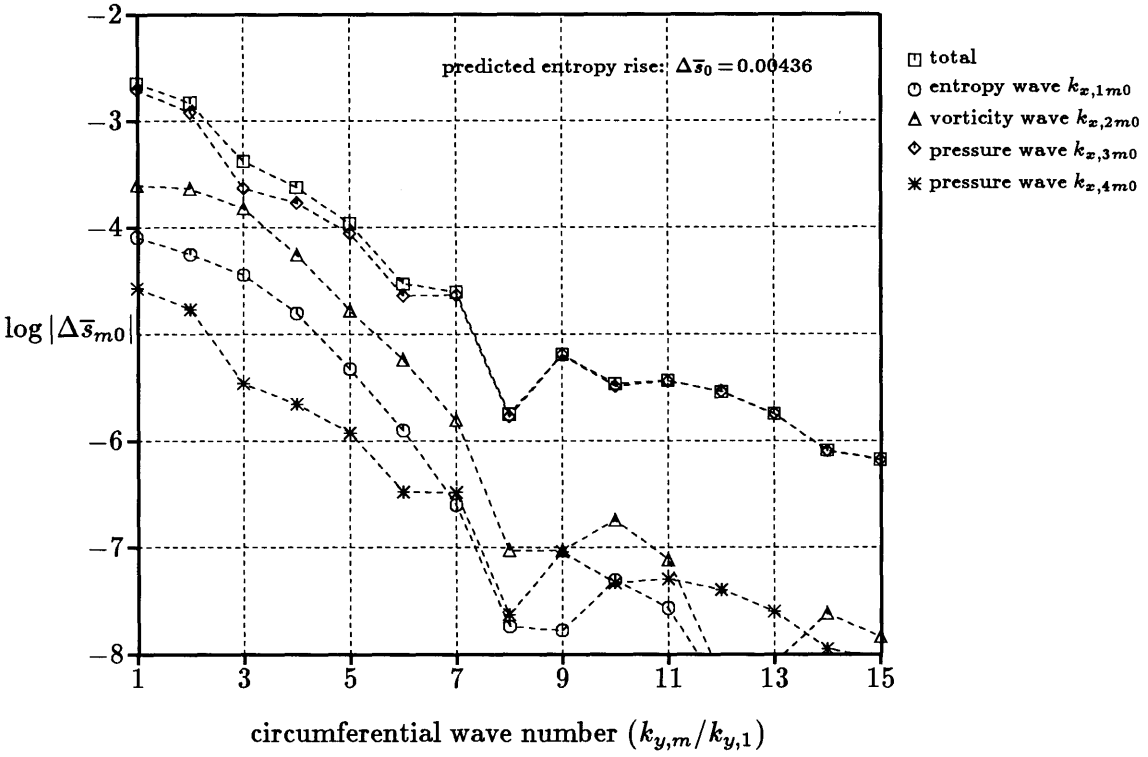

Figure 2.16: Decomposition of the entropy rise into the wave types and wavenumbers (fundamental wavenumber $k_{y,1}$ corresponds to the stator pitch)

While it was recognized previously that the interface treatment in steady simulations results in an entropy rise, it was assumed to be negligible [68]. Clearly, this is not true for stages with a high level of unsteadiness, like the ACE turbine stage. The presence of oblique shock waves introduces a relatively strong perturbation into the stator outflow and causes a considerable entropy rise upon mixing-out. The entropy rise is not without physical implication, though. The same entropy rise would be seen if stator and rotor were placed infinitely far apart and the flow allowed to mix out in between.

Many factors contribute to changes in the efficiency upon variation of the gap between blade rows. In experiments by Smith [22] and Mikolajczak [23], the efficiency increased with decreasing axial gap. In experiments by Hetherington and Moritz [24]

it decreased with decreasing axial gap. Mixing loss can give one explanation for an increase in efficiency with decreasing axial gaps. The entropy rise at the stator/rotor interface of a steady simulation is equivalent to the maximum entropy rise that can result from mixing losses.

In a *steady* subsonic flow, all pressure waves are of evanescent nature, as can easily be deduced from equation (2.15). They do not contribute to the entropy rise. In a *steady* supersonic flow, all pressure waves are non-evanescent and do contribute. Weak shock waves can be modeled as isentropic pressure waves with the vector sum of propagation velocity (speed of sound) and convection velocity along the shock front. The flow at the stator outlet boundary of the ACE turbine stage is supersonic. From figure 2.16 and table 2.1, shock waves (pressure waves propagating downstream with wavenumber $k_{3,m0}$) are seen to account for the major part of the mixing loss. Vorticity waves and entropy waves, primarily a consequence of the stator boundary layer, contribute the rest. There is also a minor (negative) contribution to the entropy rise from pressure waves propagating upstream. The flow is *axially* subsonic and pressure waves can travel upstream against the flow. Since disturbances in the rotor frame do not make themselves felt upstream beyond the interface of a steady simulation, these must be due to reflections from the stator outlet boundary. While the stator outlet boundary conditions are designed to pass through waves traveling downstream, their linear nature produces weak reflections in the presence of nonlinear phenomena like shock waves.

predicted entropy rise $\Delta\overline{s}$	0.00436
Entropy waves ($k_{x,1m}$)	4.3%
Vorticity waves ($k_{x,2m}$)	15.6%
Pressure waves ($k_{x,3m}$)	80.9%
Pressure waves ($k_{x,4m}$)	−0.8%

Table 2.1: Contributions to the entropy rise at the interface — by wave type

The linear/quadratic model overpredicts the (nonlinear) mixing loss in the simulation by only 4.5%. The discrepancy is explained by the nonlinearity of the averaging process in the presence of (all but the weakest) shock waves. Note that this behavior is

consistent with figure 2.10, which shows that the linear model overpredicts the entropy rise due to dissipation of downstream propagating pressure waves of finite amplitudes. The axial Mach number $M_{x,0}$ and the normal Mach number $M_{y,0}$ used for the supersonic cases in figure 2.10 are very close to the Mach numbers found at the stator outlet boundary in the steady simulation of the ACE turbine stage. Weak shock waves can be modeled as isentropic pressure waves with the vector sum of local convection velocity and local propagation velocity (speed of sound) pointing along the shock front. From table 2.1, downstream propagating pressure waves are seen to be the dominating perturbation at the stator outflow boundary. Given the large amplitude of the disturbance at the stator outlet, the ACE turbine stage represents a difficult test for the linear/quadratic model and it exhibits surprising accuracy.

Table 2.2 lists the contributions of different wavenumbers to the entropy rise, independent of the wave type. The fundamental wavenumber along the interface, $k_{y,1}$, corresponds to a wave with one period per (stator) blade pitch. The importance of higher harmonics is due to the presence of oblique shock waves.

predicted entropy rise $\Delta\overline{s}$	0.00436
wavenumber $k_{y,1}$	49.9%
$k_{y,2}$	32.5%
$k_{y,3}$	9.2%
$k_{y,4}$	5.2%
$k_{y,5}$	2.4%
all higher modes	0.8%

Table 2.2: Contributions to the entropy rise at the interface — by wavenumber

2.8 Summary — Unsteadiness and Loss

This chapter presented a rigorous mathematical argument relating the dissipation of unsteady waves in a uniform mean flow to the resulting entropy rise. It is the first application of an asymptotic analysis to this problem and represents the first work clearly identifying the separate contributions to the entropy rise stemming from simultaneous linear disturbances.

The accuracy of the linear/quadratic model was evaluated by comparison to a nonlinear approach. Also contained in this chapter is the first detailed analysis of the mixing loss at the stator/rotor interface of a steady simulation. The magnitude of the mixing loss predicted by the asymptotic analysis is in excellent agreement with the (nonlinear) simulation.

This chapter also pointed out another fact that seems to have been generally overlooked. As a consequence of the mixing loss at the stator/rotor interface, the steady simulation of a stage can have a lower efficiency than the corresponding unsteady simulation. The mixing loss at the interface is the same as the one which would occur for an infinite gap between the rotor row and the stator row, providing an explanation for a loss increase in turbomachinery with increasing blade row gaps.

Chapter 3
Unsteady Circulation Loss

A turbomachine blade row moves through a flow field disturbed by inflow distortions, potential interactions with adjacent blade rows, shock waves, wakes, vorticity shed at the upstream blade rows, and propagating pressure waves. Furthermore, blade movement (in flutter or forced-response problems) leads to periodic changes in the magnitude and the direction of the incoming flow vector relative to the blade. As a consequence, the blade circulation changes in a periodic manner and, in accordance with Kelvin's Circulation Theorem, vorticity is shed at the trailing edges and convected downstream with the mean flow. The transfer of energy from the mean flow into kinetic energy associated with unsteady vortex sheets is regarded as a loss in accordance with chapter 2.

This loss mechanism was first considered by Keller [10], who calculated the average kinetic energy in the vortex sheets trailing a single blade row in an incompressible flow as a function of the unsteady c irculation amplitudes and the stage geometry. He estimated the circulation amplitudes at 5% of the steady circulation and related the average rate at which energy is transferred into the vorticity field to the steady power required to turn the rotor. His results indicate that, on average, the specific secondary kinetic energy is between 0.4% and 1% of the steady specific work absorbed or developed by the rotor, with the exact value depending on the stage geometry.

Sears and Kemp [70] used thin-airfoil theory to calculate the unsteady lift acting on a rotor row subject to the wakes of an upstream stator row. Fourier decomposition of the velocity perturbation and subsequent application of results presented in earlier papers [12, 13], allowed them to calculate a slowly converging series of unsteady lift coefficients. In [11], they used thin-airfoil theory, as presented in earlier papers [15, 14], to calculate the circulation amplitudes and extended the approach to an elementary stage

with potential interactions between blade rows. This approach, while enabling them to calculate the circulation amplitudes, limited them to incompressible flow, blades of zero thickness and camber with the mean flow nearly in the blade direction, i.e. lightly loaded blades. Thus, the airfoils are more representative of compressor blades than turbine blades. Furthermore, they had to specify the steady lift distribution on the blades. They found that the unsteady circulation amplitudes are, in general, substantially less than those assumed by Keller. As a consequence, the secondary kinetic energy is less than what was found in [10]. Also, the circulation amplitudes were much larger for the upstream blade row (in a single stage) than for the downstream blade row. This was attributed to the importance of the velocity field at trailing edge to the blade circulation.

In another approach for incompressible flows, Hawthorne [16] used lifting-line theory to calculate the rate of energy transfer. He found values which are essentially in line with those of Keller.

Korakianitis [71] used a CFD-code (UNSFLO) to determine the unsteady forces acting on rotor blades in subsonic flow. He systematically varied the geometric parameters of rotor blade rows in an effort to provide design data that predicts the unsteady blade forces in response to incoming viscous wakes and potential disturbances. In the cases considered, he found average unsteady forces and moments which are typically between 90% and 100% of the mean values. Giles [6] reported a 40% peak-to-peak variation in the rotor lift for a transonic high-pressure turbine stage under the influence of unsteady shock wave/blade row interaction.

In this work, the circulation amplitudes are the results of numerical simulations, which allows one to obtain unsteady circulation amplitudes for arbitrary blade and stage geometries, steady lift distributions, and Mach numbers. Kelvin's Circulation Theorem is valid even in compressible flows, provided the flow is homentropic. Eliminating the need to estimate the circulation amplitudes or to deduce them from thin-airfoil theory, results in a realistic measure for the importance of this loss mechanism in modern turbomachines. The work proceeds along the lines of [10]; it considers a single blade row, its circulation variation and the associated trailing vorticity only. Wake/rotor and

rotor/stator interaction cases are considered. In wake/rotor interaction cases, experimental data is used to model the wake.

3.1 Analytical Theory

3.1.1 Single Airfoil

Figure 3.1 shows an airfoil experiencing an unsteady lift and circulation due to either its own motion or the imposition of an external disturbance. The coordinate system has been chosen such that the freestream velocity, U_∞, and the wake are aligned with the x-axis.

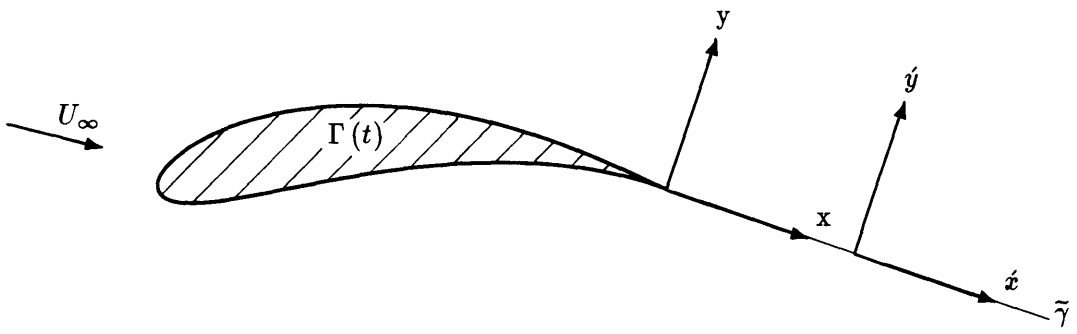

Figure 3.1: An isolated airfoil with an unsteady lift and circulation

Let the circulation on the airfoil be described by a steady component plus sinusoidally varying, unsteady components.

$$\Gamma(t) = \overline{\Gamma} + \sum_{m=1}^{\infty} \tilde{\Gamma}_m(t) = \overline{\Gamma} + \sum_{m=1}^{\infty} \Gamma_m e^{-i(\omega_m t - \varphi_m)} \tag{3.1}$$

The variable φ_m denotes the phase angle of the mth temporal mode. In the above equation, and in the remainder of this chapter, it is the real part of any quantity, that is implied by complex notation.

The strength of the unsteady vortex sheet shed at the trailing edge is determined by the condition that the sum of bound and shed vorticity remain constant. This is a consequence of Kelvin's Circulation Theorem which is valid in any compressible flow that is inviscid, barotropic, and has only conservative body forces acting on it. In a barotropic flow, the density is a function of the pressure only. The barotropic condition can be replaced by the requirement of a homentropic flow because a homentropic flow is also barotropic. If any of these conditions is violated, source terms appear in Kelvin's Circulation Theorem, and the sum of shed and bound vorticity is no longer constant.

The strength of the vortex sheet $\tilde{\gamma}(x,t)$, which is convected with the mean flow, is related to the rate of change of the circulation by

$$\tilde{\gamma}(x,t) = -\frac{1}{U_\infty}\frac{d}{dt}\left[\Gamma\left(t - \frac{x}{U_\infty}\right)\right]. \tag{3.2}$$

There are, at this point, two principal objections to this model. First, a single vortex sheet suffers from the Kelvin-Helmholtz instability to small perturbations and tends to roll up into discrete vortices. Second, due to the circulation bound to the airfoil, a simple convection of the vortex sheet is a poor model in the nearfield. The first problem is solved by noting that the kinetic energy of an isolated vortex sheet undergoing inviscid roll-up is invariant. The second problem exists in the nearfield only; in the farfield, the influence of the steady circulation is limited to an axial and circumferential offset, which is without consequence for the amount of secondary kinetic energy present.

A frame of reference convected with the mean flow, in which the flow appears steady, is introduced by

$$\acute{x} = x - U_\infty t$$

$$\text{and} \quad \acute{y} = y. \tag{3.3}$$

Equation (3.2) may now be written in the form

$$\tilde{\gamma}(\acute{x},t) = \sum_{m=1}^{\infty} \hat{\gamma}_m \exp\left\{ik_m\frac{\acute{x}}{c}\right\} = i\sum_{m=1}^{\infty} k_m\frac{\Gamma_m}{c}\exp\left\{i\left(k_m\frac{\acute{x}}{c} + \varphi_m\right)\right\}, \tag{3.4}$$

where the reduced frequency k_m is defined by

$$k_m = \frac{\omega_m c}{U_\infty}. \tag{3.5}$$

The variable c denotes the airfoil chord.

In the stationary frame, the linearized potential equation, i.e. the equation for the perturbation potential $\tilde{\phi}$ describing the flow field induced by the vortex sheet far downstream of the trailing edge, is

$$-\frac{1}{a_\infty^2}\left(\frac{\partial}{\partial t}+U_\infty\frac{\partial}{\partial x}\right)^2\tilde{\phi}+\nabla^2\tilde{\phi}=0, \tag{3.6}$$

where a denotes the speed of sound. Unsteady and convective contributions in equation (3.6) are eliminated by the shift in the frame of reference; all that remains is

$$\frac{\partial^2\tilde{\phi}}{\partial\acute{x}^2}+\frac{\partial^2\tilde{\phi}}{\partial\acute{y}^2}=0. \tag{3.7}$$

In the convected frame, the flow perturbation satisfies the equations for steady, irrotational, and incompressible flow, regardless of the freestream Mach number. Due to the linear nature of equation (3.7), the principle of superposition can by applied. Far downstream of the trailing edge, where the influence of the bound circulation is negligible, the perturbation potential $\tilde{\phi}_m$ associated with the mth mode is

$$\begin{aligned}\tilde{\phi}_m &= \hat{A}_m^+ \exp\left\{ik_m\frac{\acute{x}}{c}\right\}\exp\left\{-k_m\frac{\acute{y}}{c}\right\}, \quad \text{for} \quad \acute{y}\geq 0,\\ \text{and} \quad \tilde{\phi}_m &= \hat{A}_m^- \exp\left\{ik_m\frac{\acute{x}}{c}\right\}\exp\left\{+k_m\frac{\acute{y}}{c}\right\}, \quad \text{for} \quad \acute{y}\leq 0.\end{aligned} \tag{3.8}$$

The values of $\hat{A}_m^+$ and $\hat{A}_m^-$ are determined from the matching conditions at $\acute{y}=0$. First, the jump in the tangential velocity perturbation $\tilde{u}$ across the vortex sheet must equal the strength of the vortex sheet.

$$\tilde{u}_m\left(\acute{x},0^+\right)-\tilde{u}_m\left(\acute{x},0^-\right)=\tilde{\gamma}_m\left(\acute{x}\right) \tag{3.9}$$

This leads to

$$\hat{u}_m\left(0^+\right)-\hat{u}_m\left(0^-\right)=\hat{\gamma}_m \quad \Rightarrow \quad i\frac{k_m}{c}\left(\hat{A}_m^+-\hat{A}_m^-\right)=\hat{\gamma}_m. \tag{3.10}$$

Second, for the problem under consideration, there must be no jump in the normal velocity perturbation $\tilde{v}$.

$$\tilde{v}_m\left(\acute{x}, 0^+\right) - \tilde{v}_m\left(\acute{x}, 0^-\right) = 0 \tag{3.11}$$

From equation (3.11) follows

$$\hat{v}_m\left(0^+\right) - \hat{v}_m\left(0^-\right) = 0 \quad \Rightarrow \quad -\hat{A}_m^+ - \hat{A}_m^- = 0. \tag{3.12}$$

Combining the two results above gives

$$\hat{A}_m^+ = -\hat{A}_m^- = \frac{\Gamma_m}{2} e^{i\varphi_m}. \tag{3.13}$$

The average rate at which kinetic energy is transferred from the mean flow to the unsteady motion associated with the shed vorticity is $\overline{ke}U_\infty$. Due to the orthogonality properties of trigonometric functions, summarized in appendix B, the principle of superposition can be used. The kinetic energy in the convected frame can be calculated mode by mode and summed subsequently. The average specific kinetic energy per unit wake length and depth of the mth mode, $\overline{ke}_m$, is determined by integrating the kinetic energy over one wavelength in the $\acute{x}$-direction and from 0 to $\pm\infty$ in the $\acute{y}$-direction.

$$\begin{aligned}
\overline{ke}_m &= \frac{k_m}{2\pi c} \int_{-\infty}^{+\infty} \int_0^{2\pi c/k_m} \frac{1}{2} \left\{ \left[\Re\left(\tilde{u}_m\right)\right]^2 + \left[\Re\left(\tilde{v}_m\right)\right]^2 \right\} \, d\acute{x} \, d\acute{y} \\
&= \frac{k_m}{\pi c} \int_0^{+\infty} \int_0^{2\pi c/k_m} \frac{1}{2} \left\{ \left[\Re\left(\frac{\partial \tilde{\phi}_m}{\partial \acute{x}}\right)\right]^2 + \left[\Re\left(\frac{\partial \tilde{\phi}_m}{\partial \acute{y}}\right)\right]^2 \right\} \, d\acute{x} \, d\acute{y}
\end{aligned} \tag{3.14}$$

The symbol $\Re$ denotes the real part of a complex quantity. With the help of equation (2.31) in subsection 2.3.1, the final result for the average kinetic energy associated with the shed vorticity becomes

$$\overline{ke} = \frac{1}{8} \sum_{m=1}^{\infty} k_m \left(\frac{\Gamma_m}{c}\right)^2. \tag{3.15}$$

It is the average specific kinetic energy, $\overline{ke}$, which, in accordance with equation (2.38) of subsection 2.3.2, is related to the entropy rise upon mixing. There, the entropy rise was summed over all temporal and spatial modes, In the application here, the spatial Fourier-decomposition of the convected unsteady velocity field is not known explicitly. If the spatial Fourier-decomposition of the unsteady velocity field were carried out and the secondary kinetic energy of one temporal mode summed up by spatial modes, the

result would be the same as in equation (3.15) by virtue of the orthogonality properties of sines and cosines (appendix C). It is important to point out that the entropy rise is independent of the frame of reference and, in particular, the Mach number of the freestream. Thus, the approach taken in [10] can be extended to compressible flows.

3.1.2 Cascade

Figure 3.2 shows an analogous situation for a cascade in which every blade is experiencing an unsteady lift and circulation due to the imposition of an external disturbance induced by the upstream blade row in an elementary stage.

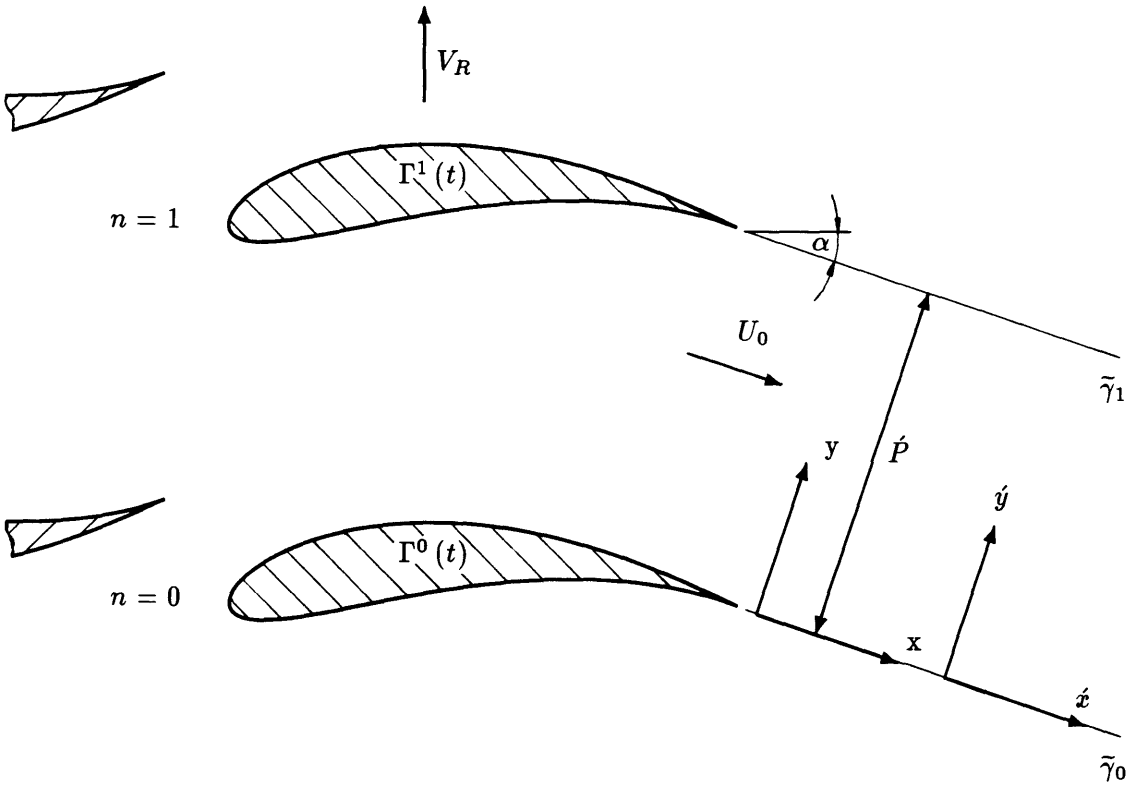

Figure 3.2: A cascade with an unsteady lift and circulation

The coordinate system has been chosen such that the mean downstream velocity, U_0, is in the $\acute{x}$-direction and the wake of the nth blade lies along $\acute{y} = n\acute{P}$. P is the

standard pitch, $\acute{P}$ the rotated pitch defined as $P\cos\alpha$, P^* the standard pitch of the neighboring blade row, and α the angle between the wake and the axial direction.

Suppose that the circulation of the nth blade is given by

$$\Gamma^n(t) = \overline{\Gamma} + \sum_{m=1}^{\infty} \tilde{\Gamma}_m^n(t)\, e^{in\beta_m} = \overline{\Gamma} + \sum_{m=1}^{\infty} \Gamma_m e^{-i(\omega_m t - n\beta_m - \varphi_m)}, \tag{3.16}$$

with β_m being the inter-blade phase angle for the mth mode. The frequencies ω_m correspond to the blade passing frequency and its harmonics

$$\omega_m = m\,\omega_f = 2\,\pi\,m\,\frac{V_R}{P^*}, \tag{3.17}$$

where V_R is the rotor speed. The inter-blade phase angle is obtained from the difference in pitch of the blade rows as

$$\beta_m = 2\,\pi\,m\,\frac{P^* - P}{P^*}\text{sign}(V_R). \tag{3.18}$$

Thus, the unsteady vortex sheet strength along the nth wake is given by

$$\tilde{\gamma}_n(x,t) = -\frac{1}{U_0}\frac{d}{dt}\left[\Gamma^n\left(t - \frac{x - nP\sin\alpha}{U_0}\right)\right]. \tag{3.19}$$

With equation (3.16), this can be expressed in the form

$$\tilde{\gamma}_n(\acute{x}) = i\sum_{m=1}^{\infty} k_m \frac{\Gamma_m}{c}\exp\left\{i\left(k_m\frac{\acute{x}}{c} + n\acute{\beta}_m + \varphi_m\right)\right\}. \tag{3.20}$$

The inter-wake phase angle of the mth mode, $\acute{\beta}_m$, is defined by

$$\frac{\acute{\beta}_m}{2} = \frac{\beta_m}{2} - \frac{1}{2}k_m\frac{P}{c}\sin\alpha = \frac{\beta_m}{2} - \lambda_m\tan\alpha, \tag{3.21}$$

with the reduced frequency λ_m given by

$$\lambda_m = \frac{1}{2}k_m\frac{\acute{P}}{c}. \tag{3.22}$$

The convected coordinate $\acute{x}$ and the reduced frequency k_m are defined as before, with U_∞ replaced by U_0, and the airfoil chord replaced by the blade axial chord. The spatial periodicity condition for the perturbation potential of the mth temporal mode is

$$\tilde{\phi}_m\left(\acute{x}, \acute{y} + \acute{P}\right) = \tilde{\phi}_m(\acute{x}, \acute{y})\, e^{i\acute{\beta}_m}. \tag{3.23}$$

The matching conditions at the zeroth wake are identical to the conditions used for a single airfoil, equations (3.9) and (3.11). For $0 \le \acute{y} \le \acute{P}$, the potential can be written as

$$\tilde{\phi}_m(\acute{x},\acute{y}) = \left[\widehat{A}\cosh\left(k_m\frac{\acute{y}}{c}-\lambda_m\right)+\widehat{B}\sinh\left(k_m\frac{\acute{y}}{c}-\lambda_m\right)\right]\exp\left\{i\left(k_m\frac{\acute{x}}{c}+\frac{\acute{\beta}_m}{2}\right)\right\}. \quad (3.24)$$

Using the periodicity condition (3.23) to relate the velocities at $(\acute{x},0^-)$ to those at $(\acute{x},\acute{P}^-)$, the matching conditions give the following equations:

$$\left(\widehat{A}_m\cosh\lambda_m-\widehat{B}_m\sinh\lambda_m\right)e^{+i\acute{\beta}_m/2}-\left(\widehat{A}_m\cosh\lambda_m-\widehat{B}_m\sinh\lambda_m\right)e^{-i\acute{\beta}_m/2}=\Gamma_m e^{i\varphi_m}$$
$$\left(\widehat{A}_m\cosh\lambda_m+\widehat{B}_m\sinh\lambda_m\right)e^{+i\acute{\beta}_m/2}+\left(\widehat{A}_m\cosh\lambda_m-\widehat{B}_m\sinh\lambda_m\right)e^{-i\acute{\beta}_m/2}=0 \quad (3.25)$$

These two equations can be written in matrix form as

$$\begin{bmatrix} +i\cosh\lambda_m\sin\frac{\acute{\beta}_m}{2} & -\sinh\lambda_m\cos\frac{\acute{\beta}_m}{2} \\ -i\sinh\lambda_m\cos\frac{\acute{\beta}_m}{2} & +i\cosh\lambda_m\sin\frac{\acute{\beta}_m}{2} \end{bmatrix}\begin{pmatrix}\widehat{A}\\ \widehat{B}\end{pmatrix}=\begin{pmatrix}\frac{\Gamma_m}{2}e^{i\varphi_m}\\ 0\end{pmatrix}, \quad (3.26)$$

and solved to yield

$$\widehat{A}_m=-\frac{i}{2}\,\frac{\cosh\lambda_m\sin\frac{\acute{\beta}_m}{2}}{\sin^2\frac{\acute{\beta}_m}{2}+\sinh^2\lambda_m}\Gamma_m e^{i\varphi_m},$$
$$\text{and}\quad \widehat{B}_m=-\frac{i}{2}\,\frac{\sinh\lambda_m\cos\frac{\acute{\beta}_m}{2}}{\sin^2\frac{\acute{\beta}_m}{2}+\sinh^2\lambda_m}\Gamma_m e^{i\varphi_m}. \quad (3.27)$$

Hence, the solution for $0 \le \acute{y} \le \acute{P}$ is

$$\tilde{\phi}_m=-\frac{\Gamma_m/2c}{\sin^2\frac{\acute{\beta}_m}{2}+\sinh^2\lambda_m}\left[i\cosh\lambda_m\sin\frac{\acute{\beta}_m}{2}\cosh\left(k_m\frac{\acute{y}}{c}-\lambda_m\right)\right.$$
$$\left.+\sinh\lambda_m\cos\frac{\acute{\beta}_m}{2}\sinh\left(k_m\frac{\acute{y}}{c}-\lambda_m\right)\right]\exp\left\{i\left(k_m\frac{\acute{x}}{c}+\frac{\acute{\beta}_m}{2}+\varphi_m\right)\right\}, \quad (3.28)$$

$$\tilde{u}_m=-\frac{k_m\Gamma_m/2c}{\sin^2\frac{\acute{\beta}_m}{2}+\sinh^2\lambda_m}\left[-\cosh\lambda_m\sin\frac{\acute{\beta}_m}{2}\cosh\left(k_m\frac{\acute{y}}{c}-\lambda_m\right)\right.$$
$$\left.+i\sinh\lambda_m\cos\frac{\acute{\beta}_m}{2}\sinh\left(k_m\frac{\acute{y}}{c}-\lambda_m\right)\right]\exp\left\{i\left(k_m\frac{\acute{x}}{c}+\frac{\acute{\beta}_m}{2}+\varphi_m\right)\right\}, \quad (3.29)$$

and

$$\tilde{v}_m=-\frac{k_m\Gamma_m/2c}{\sin^2\frac{\acute{\beta}_m}{2}+\sinh^2\lambda_m}\left[i\cosh\lambda_m\sin\frac{\acute{\beta}_m}{2}\sinh\left(k_m\frac{\acute{y}}{c}-\lambda_m\right)\right.$$
$$\left.+\sinh\lambda_m\cos\frac{\acute{\beta}_m}{2}\cosh\left(k_m\frac{\acute{y}}{c}-\lambda_m\right)\right]\exp\left\{i\left(k_m\frac{\acute{x}}{c}+\frac{\acute{\beta}_m}{2}+\varphi_m\right)\right\}. \quad (3.30)$$

The corresponding average kinetic energy per unit mass is

$$\begin{aligned}
\overline{ke}_m &= \frac{1}{\acute{P}}\int_0^{\acute{P}} \frac{k_m}{2\pi c}\int_0^{2\pi c/k_m} \frac{1}{2}\left[\Re^2\left(\tilde{u}_m\right)+\Re^2\left(\tilde{v}_m\right)\right] d\acute{y}\, d\acute{x} \\
&= \left(\frac{k_m\Gamma_m/4c}{\sin^2\frac{\acute{\beta}_m}{2}+\sinh^2\lambda_m}\right)^2 \left(\cosh^2\lambda_m \sin^2\frac{\acute{\beta}_m}{2}+\sinh^2\lambda_m\cos^2\frac{\acute{\beta}_m}{2}\right)\times \\
&\qquad \times\frac{1}{\acute{P}}\int_0^{\acute{P}}\left[\cosh\left(k_m\frac{\acute{y}}{c}-\lambda_m\right)+\sinh\left(k_m\frac{\acute{y}}{c}-\lambda_m\right)\right] d\acute{y} \\
&\qquad = \frac{(k_m\Gamma_m/4c)^2}{\sin^2\frac{\acute{\beta}_m}{2}+\sinh^2\lambda_m}\frac{1}{\acute{P}}\int_0^{\acute{P}}\cosh 2\left(k_m\frac{\acute{y}}{c}-\lambda_m\right) d\acute{y} \\
&\qquad\qquad = \frac{1}{4}\left(\frac{\Gamma_m}{\acute{P}}\right)^2 \frac{\lambda_m\sinh\lambda_m\cosh\lambda_m}{\sin^2\frac{\acute{\beta}_m}{2}+\sinh^2\lambda_m}, \qquad (3.31)
\end{aligned}$$

which can be shown to coincide with the result of [10]. When this energy is dissipated later, the resulting mass-average entropy increase is

$$\Delta\bar{s}_m = \frac{\gamma-1}{4}\left(\frac{\Gamma_m}{\acute{P}a_0}\right)^2 \frac{\lambda_m\sinh\lambda_m\cosh\lambda_m}{\sin^2\frac{\acute{\beta}_m}{2}+\sinh^2\lambda_m}, \qquad (3.32)$$

in accordance with equation (2.38) of subsection 2.3.2. The corresponding total pressure drop

$$\Delta\bar{p}_{t,m} = -\frac{\gamma}{4}\left(\frac{\Gamma_m}{\acute{P}a_0}\right)^2 \frac{\lambda_m\sinh\lambda_m\cosh\lambda_m}{\sin^2\frac{\acute{\beta}_m}{2}+\sinh^2\lambda_m} \qquad (3.33)$$

is obtained from equation (2.47).

3.1.3 Cross-Induced Kinetic Energies

The shedding of vorticity at the trailing edge in response to circulation variations is ultimately caused by the presence of unsteady perturbations. Vorticity waves, in the form of wakes being convected with the mean flow, and pressure waves, in the form of weak shock waves, are found to be of equal importance in the following section. For very small axial gaps, evanescent potential interactions can be significant, too.

If shedding of vorticity is being caused by the presence of weak shock waves or the evanescent potential field of the upstream blade row in an elementary stage, the entropy rise calculated with the kinetic energy (3.31) only is correct. As was shown

in subsection 2.3.2, propagating pressure waves and evanescent potential fields do not couple with vorticity waves upon dissipation. A very weak shock wave can be thought of as being composed of isentropic pressure waves with the vector sum of the local convection velocity and the local speed of sound pointing along the shock front.

Vorticity waves (wakes), however, can be both cause and consequence of unsteady voticity shedding at the trailing edge. The vorticity waves being convected through a cascade and causing a periodic circulation variation are of the same frequency and axial wavenumber as the vorticity shed at the trailing edge. In the calculation of the secondary kinetic energy (3.31), the velocities induced by the vorticity convected through the blade row and the kinetic energy associated with it, are not accounted for. There are three reasons for the neglect of these cross-induced contributions.

First, it is difficult to account analytically for cross-induced contributions in the complex geometries and flow fields that will be considered. The vorticity convected through a cascade adds to, or subtract from, the self-induced secondary kinetic energy (3.31) (depending on the phase relationship between convected and shed vorticity), giving the self-induced kinetic energy the character of a mean value. The self-induced kinetic energy is associated with velocities induced by a blade row's own trailing vortex sheets.

Second, for potential rotor/stator interaction in an elementary stage, the analysis by Kemp and Sears in [70] suggests that the cross-induced contributions (from the vorticity shed at the trailing edge of the upstream blade row) to the secondary kinetic energy beyond the downstream blade are of the same size as the self-induced contributions. For the upstream blade row, they were found to be negligible. The differing relative magnitudes of self-induced and cross-induced contributions were explained by the circulation amplitudes; the upstream blade rows showed unsteady circulation amplitudes which were a factor of ten larger than those of the downstream blade rows. In the simulations performed here, the circulation amplitudes were of the same order of magnitude, suggesting a second rationale for neglecting cross-induced contributions.

Third, in wake/rotor interaction, most of the wake unsteadiness originating at the trailing edge of the upstream blade row is in the lowest circumferential wavenumber. As a consequence, most of the unsteadiness in the (frame of reference of the) downstream blade row is at the fundamental (blade passing) frequency. In the convected frame beyond the trailing edge of the downstream blade row, most of the unsteadiness associated with the convected vorticity is therefore found at the fundamental streamwise wavenumber. While the shed vorticity induces a velocity field continuous in the streamwise ($\acute{x}-$)direction, it introduces a discontinuity in the normal ($\acute{y}-$)direction. This implies that the shed vorticity has energy in discrete normal wavenumbers spread over an infinite range, even if the incoming unsteadiness has its energy confined to the blade passing frequency. Due to the orthogonalities of sines and cosines, summarized in appendix C, there is no crosscoupling between the incoming convected vorticity and the higher harmonics of the shed vorticity in the normal ($\acute{y}-$)direction. It is therefore legitimate to ask how much of the secondary kinetic energy is in the higher spatial harmonics. To that end, the normal Fourier modes of the velocity field described by equations (3.29) and (3.30) have to be found. For the mth temporal mode, the normal wavenumbers downstream of the rotor are

$$k_n = \frac{\acute{\beta}_m + 2\pi n}{\left(\acute{P}/c\right)}. \tag{3.34}$$

For simplicity, and without loss of insight, it will be assumed that $\acute{\beta}_m$ is an integer multiple of 2π and that $\varphi_m = 0$.

$$\acute{\beta}_m = 2j\ \pi, \qquad j = \pm 1, \pm 2, ... \tag{3.35}$$

If the inter-wake phase angle were not taken to be zero, the determination of the Fourier coefficients would involve a summation over a finite number of blades. This is because the potential (3.28) is valid only over an interval of extent $\acute{P}$, while the integration to obtain the Fourier coefficients has to be carried out over an interval of periodicity. The Fourier coefficients are:

$$u_{mn,s} = \frac{2}{(\acute{P}/c)} \int_0^{\acute{P}/c} \tilde{u} \sin\left(k_n \frac{\acute{y}}{c}\right)\ d\left(\frac{\acute{y}}{c}\right) = -2(-1)^{|n|} \left(\frac{\Gamma_m}{\acute{P}}\right) \frac{k_m k_n}{k_m^2 + k_n^2} \sin\left(k_m \frac{\acute{x}}{c}\right) \tag{3.36}$$

$$u_{mn,c} = \frac{2}{(\acute{P}/c)} \int_0^{\acute{P}/c} \tilde{u} \cos\left(k_n \frac{\acute{y}}{c}\right) \; d\left(\frac{\acute{y}}{c}\right) = 0 \quad (3.37)$$

$$v_{mn,s} = \frac{2}{(\acute{P}/c)} \int_0^{\acute{P}/c} \tilde{v} \sin\left(k_n \frac{\acute{y}}{c}\right) \; d\left(\frac{\acute{y}}{c}\right) = 0 \quad (3.38)$$

$$v_{mn,c} = \frac{2}{(\acute{P}/c)} \int_0^{\acute{P}/c} \tilde{v} \cos\left(k_n \frac{\acute{y}}{c}\right) \; d\left(\frac{\acute{y}}{c}\right) = -2(-1)^{|n|} \left(\frac{\Gamma_m}{\acute{P}}\right) \frac{k_m^2}{k_m^2 + k_n^2} \cos\left(k_m \frac{\acute{x}}{c}\right) \quad (3.39)$$

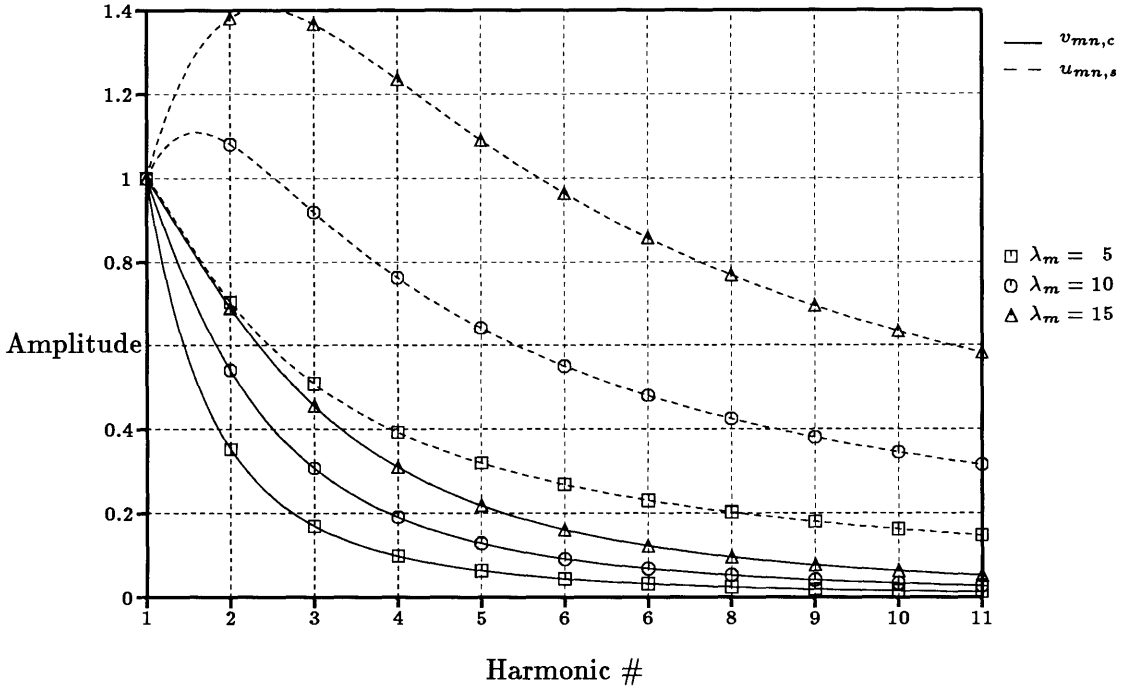

Figure 3.3: Relative magnitude of the spatial harmonics in the shed vorticity wake (first harmonic corresponds to the pitch of the upstream blade row)

Figure 3.3 shows the relative magnitude of the velocity harmonics $u_{mn,s}$ and $v_{mn,c}$, nondimensionalized by the respective first spatial harmonic, with the reduced frequency λ_m as a parameter. Note that for higher harmonics (large wavenumbers) $u_{mn,s} \sim 1/k_n$, which is consistent with the discontinuity of the streamwise velocity perturbation $\tilde{u}$ at the vortex sheet. Since the normal velocity perturbation $\tilde{v}$ is continuous everywhere, one finds $v_{mn,c} \sim 1/k_n^2$ for large wavenumbers. The quadratic decay is mandated by the discontinuity of its derivative at the vortex sheet. This is easily deduced from the potential equation in the form $(\partial\tilde{v}/\partial\acute{y}) = -(\partial\tilde{u}/\partial\acute{x})$. From equations (3.36) and (3.39),

one can calculate the spatial average of the secondary kinetic energy associated with a wavenumber k_n.

$$\overline{ke}_{mn} = \frac{1}{2}\left(\frac{\Gamma_m}{\acute{P}}\right)^2 \frac{k_m^2}{k_m^2 + k_n^2} \sim \frac{1}{1 + (\pi/\lambda_m)^2 n^2} \tag{3.40}$$

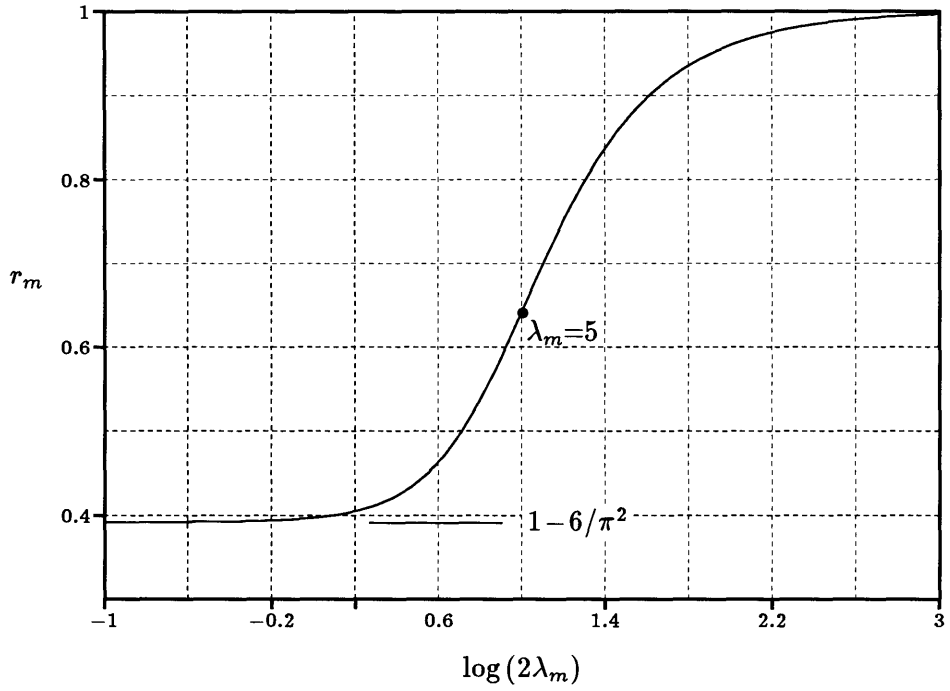

Figure 3.4: Relative amount of kinetic energy in higher spatial harmonics

Figure 3.4 shows the ratio

$$r_m = \frac{\sum_{n=2}^{\infty} \overline{ke}_{mn}}{\sum_{n=1}^{\infty} \overline{ke}_{mn}}. \tag{3.41}$$

versus the governing parameter λ_m. Even in the limit $\lambda_m \to 0$, i.e. for zero reduced frequency, there is a finite amount of secondary kinetic energy in higher spatial harmonics. The limiting case for $\lambda_m = 0$ leads to a value of

$$r_m = 1 - \frac{1}{\sum_{n=1}^{\infty}(1/n^2)} = 1 - \frac{6}{\pi^2} \approx 39.2\%. \tag{3.42}$$

In the cases considered in the next section, a typical value of λ_m is 5 and roughly 64% of the secondary kinetic energy is found in higher spatial harmonics.

3.2 Results — Unsteady Circulation Loss

The analytic model described in the previous section was applied to a number of blade rows and stages. The amplitudes of the unsteady circulation were calculated with the CFD-code UNSFLO by Giles [5, 6]. The simulations were run until the flow was periodic; then 50 instantaneous flow solutions equally-spaced in time were stored, from which the circulation amplitudes were determined. For a single blade row, unsteadiness due to upstream blade rows, (i.e. viscous wakes and potential disturbances), was modeled at the inflow boundary. Incoming wake models and potential disturbance models are described in [67].

3.2.1 Single-Stage, Large-Scale Turbine No. 2 at Cambridge

Hodson [69] conducted measurements of wake-generated unsteadiness in the rotor of a large-scale, low-speed, single-stage, air-driven turbine. As detailed in [69], the stage is a free-vortex design with zero exit swirl and high reaction. The uniform axial velocity at the stage inlet combined with radial equilibrium results in no curvature in the meridional plane. The flow at midspan can thus be regarded as two-dimensional. The 51 rotor blades are separated from 36 stator blades by an axial gap of about one rotor axial chord. In [42], Hodson computed the two-dimensional wake/rotor interaction with the data for the modeling of the incoming wake taken from [69].

Input Parameters		Others	
Inlet Flow Angle	2.1^o	Outlet Flow Angle α	-66.8^o
Exit Static Pressure	0.8956	Inlet Mach Number	0.14
Isentropic Exponent	1.4	Outlet Mach Number M_0	0.40
Stator Pitch/Rotor Pitch	1.417	Rotor Pitch	0.982
Rotor Speed V_R	0.3104	Reduced Frequency k_1	3.45

Table 3.1: Input parameters for the simulation of the Cambridge No.2 turbine

The input parameters for the simulation are in table 3.1. Pressures have been nondimensionalized by the inlet stagnation pressure, lengths by the rotor axial chord and velocities by the inlet stagnation speed of sound. Outlet flow angles as well as inlet and outlet Mach numbers are time-mean mass-averages in the frame of reference moving with the corresponding blade row. The wake model was identical to the one used by Hodson in [42]. The maximum velocity defect and the wake width were chosen such as to replicate the maximum velocity and the momentum deficit in figure 4 of [69]. No effort was made to account for the viscous decay of the wake in the experiment. In the absence of information about a potential disturbance acting on the rotor, it was not modeled. Given the large axial gap, it can be expected to be insignificant.

Wake only	
Wake Velocity Defect in [%]	4.6
Wake Width/Stator Pitch in [%]	30
Wake Angle (stator frame)	65.0^o
$\Gamma_1/\overline{\Gamma}$ in [%]	0.67
Entropy Rise $\Delta\overline{s}_1$	1.66×10^{-6}
Total Pressure Drop[1] $-\Delta\overline{p}_{t,1}$	5.80×10^{-6}
Efficiency Drop $-\Delta\eta_{s,E}/\eta_{s,E,D}$	$\approx 0.04\%$

Table 3.2: Unsteadiness parameters and results for the Cambridge No.2 turbine

The result of the simulation is summarized in table 3.2. With the harmonics of the circulation known, the entropy rise and the total pressure loss are obtained from equations (3.32) and (3.33), respectively. Section 2.5 relates the total pressure drop to the drop in the isentropic efficiency. Higher harmonics of the circulation ($\Gamma_m, m > 1$) did not contribute significantly and are not included in the above table. In the remainder of this chapter, higher harmonics have been found to be insignificant, i.e. more than a factor of 10 smaller than Γ_1, if they are not listed.

[1] Total pressure drop as defined here is not used in low speed flows. Instead, the total pressure drop is nondimensionalized by the dynamic head. It is used here to be in line with the chain of reasoning in chapter 2. The important measure is the efficiency drop.

3.2.2 Large Scale Rotating Rig (LSRR) at UTRC

The second case is a simulation of the flow through the rotor of a large-scale, axial-flow turbine model investigated experimentally by Joslyn, Dring, and Sharma [72]. It is a one and one-half stage turbine model consisting of 22 first vanes, 28 first blades, and 28 second vanes, representing the first three blade rows of the high-pressure turbine of a high bypass-ratio aircraft turbine. The Reynolds number of 5.6×10^6 and the absolute and relative flow angles are typical for current high-pressure turbine airfoils. The important input parameters for the simulation of the flow through the rotor are summarized in table 3.3.

Input Parameters		Others	
Inlet Flow Angle	48.9^o	Outlet Flow Angle α	-65.5^o
Exit Static Pressure	0.975	Inlet Mach Number	0.124
Isentropic Exponent	1.4	Outlet Mach Number M_0	0.200
Stator Pitch/Rotor Pitch	1.2727	Rotor Pitch	0.9578
Rotor Speed V_R	0.1137	Reduced Frequency k_1	2.92

Table 3.3: Input parameters for the LSRR simulation

In a first simulation, the incoming unsteadiness consisted of wakes only. The wake profile was Gaussian as described in [67]; the wake width and the maximum velocity defect were chosen to match the maximum velocity defect and the momentum defect at midspan downstream of the first vanes, which were documented in figure 6 of [72].

In a second simulation, a potential disturbance was superimposed upon the wake disturbance. The unsteady pressure amplitude of the potential disturbance was chosen such that it causes a potential velocity perturbation resembling the one shown in figure 6 of [72]. However, while the measurement station in the experiment is approximately $0.52\times$(axial chord) upstream of the rotor leading edge, the location of the potential disturbance was set at $0.15\times$(axial chord) in the simulation. Otherwise, the influence of the incoming potential disturbance on the rotor would have been negligible due to its strong exponential decay at low Mach numbers. Also, depending on the lo-

cation of the inflow boundary, where the potential disturbance is prescribed, it can add to or subtract from the wake effect on the circulation. The results of both simulations are in table 3.4.

Wake		Wake+Potential	
Wake Velocity Defect in [%]	15	Pressure Disturbance	3×10^{-3}
Wake Width/Stator Pitch in [%]	0.10	Disturbance Location	-0.15
Wake Angle (stator frame)	68.5^o		
$\Gamma_1/\overline{\Gamma}$ in [%]	0.57	$\Gamma_1/\overline{\Gamma}$ in [%]	0.68
Entropy Rise $\Delta\overline{s}_1$	1.23×10^{-5}	$\Delta\overline{s}_1$	1.72×10^{-5}
Total Pressure Drop $-\Delta\overline{p}_{t,1}$	4.32×10^{-5}	$-\Delta\overline{p}_{t,1}$	6.01×10^{-5}
Efficiency Drop $-\Delta\eta_{s,E}/\eta_{s,E,D}$	0.11%	$-\Delta\eta_{s,E}/\eta_{s,E,D}$	0.15%

Table 3.4: Unsteadiness parameters and results for the LSRR

3.2.3 Cold Air Turbine Stage at the DFVLR

Binder [73] used the L2F technique to measure the flow in cold air turbine test facility. The stage had 20 stator blades, 31 rotor blades, and an axial gap of 113% rotor axial chord; it was a scaled version of the first stage of an helicopter gas turbine.

The flow in the low aspect ratio, high hub-to-tip ratio stage was weakly transonic and showed a wake with a velocity defect of 6.5% and an angle of 70^o at midspan, 50% rotor axial chord upstream of the rotor leading edge. Potential interactions at this axial gap were found to be negligible. In the simulation, the unsteadiness at the rotor inlet boundary consisted of wakes only. The input parameters for the simulation are in table 3.5. Based on the velocity distribution at the rotor inlet measuring plane, documented in figure 5.7 of [73], a sinusoidal wake model, as described in [67], with a maximum velocity defect of 6.5% in the stator frame of reference was chosen.

Input Parameters		Others	
Inlet Flow Angle	46.7^o	Outlet Flow Angle α	-62^o
Exit Static Pressure	0.699	Inlet Mach Number	0.43
Isentropic Exponent	1.27	Outlet Mach Number M_0	0.65
Stator Pitch/Rotor Pitch	1.55	Rotor Pitch	0.822
Rotor Speed V_R	0.5765	Reduced Frequency k_1	4.25

Table 3.5: Input parameters for the DFVLR turbine simulation

Note that this case does not strictly satisfy the condition of homentropic flow required by Kelvin's Circulation Theorem (in compressible flow). Since the flow is not incompressible, as in the previous two cases, a viscous wake consists of a vorticity wave accompanied by an entropy wave.

Wake only	
Wake Velocity Defect in [%]	6.5
Wake Angle (stator frame)	70^o
$\Gamma_1/\overline{\Gamma}$ in [%]	2.83
Entropy Rise $\Delta\overline{s}_1$	3.56×10^{-4}
Total Pressure Drop $-\Delta\overline{p}_{t,1}$	1.67×10^{-3}
Efficiency Drop $-\Delta\eta_{s,E}/\eta_{s,E,D}$	0.24%

Table 3.6: Unsteadiness parameters and results for the DFVLR turbine

3.2.4 ACE Turbine Stage

This subsection shows the results obtained for a highly, loaded transonic high-pressure turbine stage, which has been investigated at MIT [50] and Oxford University [52, 54]. In the experiments, the objective was to closely simulate all the important nondimensional parameters of fluid mechanics and heat transfer in a modern high-pressure turbine stage, while reducing the initial turbine metal temperature. A detailed computational account of the inviscid stator/rotor interaction, dominated by weak shock waves, for almost identical input parameters is presented in [6]; it was briefly recounted in section 2.7. Table 3.7 lists the input parameters used in the simulation.

Input Parameters		Others	
Stator Inflow Angle	0.0^o	Stator Outflow Angle	73.5^o
Exit Static Pressure	0.27	Rotor Inflow Angle	56.7^o
Isentropic Exponent	1.28	Rotor Outflow Angle	-67.6^o
Stator Pitch/Rotor Pitch	0.8631	Rotor Pitch	1.399
Rotor Speed V_R	0.55	Stator Inlet Mach Number	0.14
Reduced Frequency k_1	2.38 (rotor)	Stator Outlet Mach Number	1.13
		Rotor Inlet Mach Number	0.59
		Rotor Outlet Mach Number	1.11

Table 3.7: Input parameters for the ACE turbine stage simulation

In the simulation, wake/rotor interaction is not accounted for. The potential interaction and the interaction of weak shock waves with the blade rows are the result of the simulation rather than being prescribed as boundary conditions. This case relies on the fact that weak shock waves are almost isentropic with $\Delta s \sim (M-1)^3$ to satisfy the requirement of homentropic flow in Kelvin's Circulation Theorem. Table 3.8 lists the results.

Stator		Rotor	
$\Gamma_1/\overline{\Gamma}$ in [%]	0.61	$\Gamma_1/\overline{\Gamma}$ in [%]	2.19
Entropy Rise		$\Delta\overline{s}_1$	7.01×10^{-4}
Total Pressure Drop		$-\Delta\overline{p}_{t,1}$	3.21×10^{-3}
$\Gamma_2/\overline{\Gamma}$ in [%]	0.27	$\Gamma_2/\overline{\Gamma}$ in [%]	1.02
Entropy Rise		$\Delta\overline{s}_2$	2.60×10^{-4}
Total Pressure Drop		$-\Delta\overline{p}_{t,2}$	1.19×10^{-3}
$\Gamma_3/\overline{\Gamma}$ in [%]	0.07	$\Gamma_3/\overline{\Gamma}$ in [%]	0.20
Entropy Rise		$\Delta\overline{s}_3$	1.55×10^{-5}
Total Pressure Drop		$-\Delta\overline{p}_{t,3}$	7.07×10^{-5}
$\Gamma_4/\overline{\Gamma}$ in [%]	0.07	$\Gamma_4/\overline{\Gamma}$ in [%]	0.25
Entropy Rise		$\Delta\overline{s}_4$	3.11×10^{-5}
Total Pressure Drop		$-\Delta\overline{p}_{t,4}$	1.42×10^{-4}
$\Gamma_5/\overline{\Gamma}$ in [%]		$\Gamma_5/\overline{\Gamma}$ in [%]	0.13
Entropy Rise		$\Delta\overline{s}_5$	1.12×10^{-5}
Total Pressure Drop		$-\Delta\overline{p}_{t,5}$	5.12×10^{-5}
$\Gamma_6/\overline{\Gamma}$ in [%]		$\Gamma_6/\overline{\Gamma}$ in [%]	0.10
Entropy Rise		$\Delta\overline{s}_6$	8.15×10^{-6}
Total Pressure Drop		$-\Delta\overline{p}_{t,6}$	3.27×10^{-5}
Entropy Rise		$\sum_{m=1}^{6} \Delta\overline{s}_m$	$\approx 1.3 \times 10^{-3}$
Total Pressure Drop		$\sum_{m=1}^{6} -\Delta\overline{p}_{t,m}$	$\approx 4.7 \times 10^{-3}$
Efficiency Drop		$-\Delta\eta_{s,E}/\eta_{s,E,D}$	$\approx 0.30\%$

Table 3.8: Results for the ACE turbine stage

As a consequence of the shock wave/blade row interaction, comparatively large unsteady lift amplitudes are expected; Giles [6] reported a 40% peak-to-peak variation in the rotor lift for almost identical input parameters. Nevertheless, the circulation amplitudes ($\Gamma_i/\overline{\Gamma}$) of the rotor remain small. At 5.5% of the mean, the peak-to peak

variation in the circulation is one order of magnitude less than the lift variation. The increased importance of higher harmonics of the rotor unsteady circulation is the result of shock waves which represent localized disturbances with a significant content of higher-order temporal modes. Since the stator is choked, the unsteady stator circulation is substantially smaller.

3.2.5 NASA Stage 67 Compressor

The NASA Stage 67 is a low aspect ratio, single-stage, transonic, axial-flow compressor designed and experimentally investigated at the NASA Lewis Research Center [74, 75, 76]. It consists of 22 rotor blades separated from 34 stator blades by an axial gap of 78% rotor axial chord. At a rotor tip Mach number of 1.38, strong shocks are present in the rotor passage. Shang [77] used UNSFLO to calculate the flow through the stage at midspan with the input parameters inferred from the experiments at NASA Lewis.

Input Parameters		Others	
Rotor Inflow Angle	59.9^o	Rotor Outflow Angle	39.7^o
Exit Static Pressure	0.8103	Stator Inflow Angle	-44.7^o
Isentropic Exponent	1.4	Stator Outflow Angle	3.5^o
Rotor Pitch/Stator Pitch	1.55	Rotor Pitch	0.808
Rotor Speed V_R	0.8335	Rotor Inlet Mach Number	1.106
Reduced Frequency k_1	21.5 (stator)	Rotor Outlet Mach Number	0.624
		Stator Inlet Mach Number	0.668
		Stator Outlet Mach Number	0.457

Table 3.9: Input parameters for the NASA stage 67 simulations

The case considered here is a stage with purely potential interaction between blade rows. The strength of the potential interaction strongly depends on the size of the gap separating the two blade rows. A wide range of gap sizes exist in compressors and the gap itself varies from hub to tip. To be in line with modern compressor designs, the

axial gap had been set to 10% and 20%. The results are listed in table 3.10.

Gap in % rotor axial chord	10	Gap	20
$\Gamma_1/\overline{\Gamma}$ in [%] (rotor)	2.08	$\Gamma_1/\overline{\Gamma}$ in [%] (rotor)	0.69
$\Gamma_1/\overline{\Gamma}$ in [%] (stator)	0.90	$\Gamma_1/\overline{\Gamma}$ in [%] (stator)	0.44
Entropy Rise $\Delta\overline{s}_1$	1.06×10^{-5}	$\Delta\overline{s}_1$	2.54×10^{-6}
Total Pressure Drop $-\Delta\overline{p}_{t,1}$	3.73×10^{-5}	$-\Delta\overline{p}_{t,1}$	8.90×10^{-6}
$\Gamma_2/\overline{\Gamma}$ in [%] (stator)	0.80	$\Gamma_2/\overline{\Gamma}$ in [%] (stator)	0.41
Entropy Rise $\Delta\overline{s}_2$	1.68×10^{-5}	$\Delta\overline{s}_2$	4.42×10^{-6}
Total Pressure Drop $-\Delta\overline{p}_{t,2}$	5.89×10^{-5}	$-\Delta\overline{p}_{t,2}$	1.55×10^{-5}
$\Gamma_3/\overline{\Gamma}$ in [%] (stator)	0.49	$\Gamma_3/\overline{\Gamma}$ in [%] (stator)	0.24
Entropy Rise $\Delta\overline{s}_3$	9.47×10^{-6}	$\Delta\overline{s}_3$	2.27×10^{-6}
Total Pressure Drop $-\Delta\overline{p}_{t,3}$	3.31×10^{-5}	$-\Delta\overline{p}_{t,3}$	7.95×10^{-6}
$\Gamma_4/\overline{\Gamma}$ in [%] (stator)	0.14	$\Gamma_4/\overline{\Gamma}$ in [%] (stator)	0.07
Entropy Rise $\Delta\overline{s}_4$	1.03×10^{-6}	$\Delta\overline{s}_4$	2.58×10^{-7}
Total Pressure Drop $-\Delta\overline{p}_{t,4}$	3.61×10^{-6}	$-\Delta\overline{p}_{t,4}$	9.01×10^{-7}
$\sum_{m=1}^{4} \Delta\overline{s}_m$	$\approx 4.0 \times 10^{-5}$	$\sum_{m=1}^{4} \Delta\overline{s}_m$	$\approx 1.0 \times 10^{-5}$
$\sum_{m=1}^{4} -\Delta\overline{p}_{t,m}$	$\approx 1.4 \times 10^{-4}$	$\sum_{m=1}^{4} -\Delta\overline{p}_{t,m}$	$\approx 3.5 \times 10^{-5}$
Efficiency Drop $-\Delta\eta_{s,C}/\eta_{s,C,D}$	$\approx 0.03\%$	$-\Delta\eta_{s,C}/\eta_{s,C,D}$	$< 0.01\%$

Table 3.10: Results for the NASA stage 67 simulations

This case, aside from the compressible nature of the flow, comes closest to the assumptions made by Sears and Kemp[11, 15]. Another simulation performed by Shang and documented in [77] indicates that the unsteadiness induced by rotor wake/stator interaction is of the same order of magnitude.

3.3 Summary — Unsteady Circulation Loss

The typical magnitude of the unsteady circulation amplitudes in incompressible flow was estimated at 5% of the mean by Keller [10]. In their incompressible considerations within the limits of thin-airfoil theory, Kemp and Sears [11] concluded that the amplitudes are, generally, substantially less than 5%. The values found in this thesis for realistic geometries in compressible flow suggest that 5% is an upper bound for the unsteady circulation amplitude. Typical values were on the order of 1% with larger values for highly loaded blade rows, small axial gaps, and high turning. Even the rotor of the ACE turbine stage, for which a 40% peak-to-peak variation in the lift was reported [6], shows only a 5.5% peak-to-peak variation in the circulation. In stator/rotor interaction simulations, the circulation amplitudes of the upstream and the downstream blade rows were of the same order of magnitude, which contrasts with the results of [11]; there the unsteady circulation of the upstream blade row was found to be a factor of 10 larger. In the ACE turbine stage it was only one fourth, and in the NASA stage 67 it was twice the magnitude of the circulation amplitude of the downstream blade row.

Wake/rotor interaction and weak shock wave/blade row interaction are the most important mechanisms leading to an unsteady circulation. Potential interaction is only important for very small axial gaps between blade rows.

Keller [10] calculated the ratio K_v of the kinetic energy in the trailing vorticity to the steady power required to turn, or delivered by, the rotor; he found values of $0.04 < K_v < 0.01$ for various configurations and circulation amplitudes of 5%. In line with the smaller circulation amplitudes, the losses here are smaller than suggested by Keller. In the turbine stages considered, the dissipation of the secondary kinetic energy associated with trailing vorticity led to a drop in the isentropic stage efficiency of up to 0.24% through wake/rotor interaction. Dissipation of the secondary kinetic energy in the vorticity trailing the rotor of the ACE turbine stage, where the unsteady interaction is dominated by weak shock waves, led to a drop in the stage efficiency of 0.30%. In the NASA stage 67 compressor, the efficiency drop was much less than in the ACE-turbine

case because it is missing the shock wave/blade row interaction. The smallest gap of 10% axial chord resulted in a 0.03% drop in the isentropic efficiency only.

With turbine efficiencies generally beyond 90%, these results imply that Unsteady Circulation Loss represents a small unsteady loss mechanism. The profile loss typically accounts for one half of the losses in a turbine [53]; unsteady operating conditions can cause an increase of 50% or more [9] if the character of the boundary layer changes. Thus, one expects efficiencies in unsteady flow to decrease by roughly 2% as a consequence of this (strongly nonlinear) loss mechanism alone. Unsteady Circulation Loss is comparably small; they only account for a small part of the steady loss or the unsteady loss. Also, it are certainly small compared to the uncertainty in measured efficiencies.

No further work is suggested on the subject of Unsteady Circulation Loss because its magnitude has been clearly established and was found to be small.

Chapter 4

Unsteady Viscous Loss

Unsteady Viscous Loss is loss with a non-zero time-mean due to viscous dissipation of energy associated with the unsteady part of the flow field. Subsequently, it will be shown that the primary locus of dissipation, in real turbomachinery flows, is in unsteady boundary layers rather than in the freestream. Before comparing the relative importance of unsteady loss in the freestream and the boundary layers, it is necessary to clarify the concept of an unsteady boundary layer and to introduce the relevant length scales and time scales. Figures 4.1 to 4.4 serve to illustrate the loss mechanism.

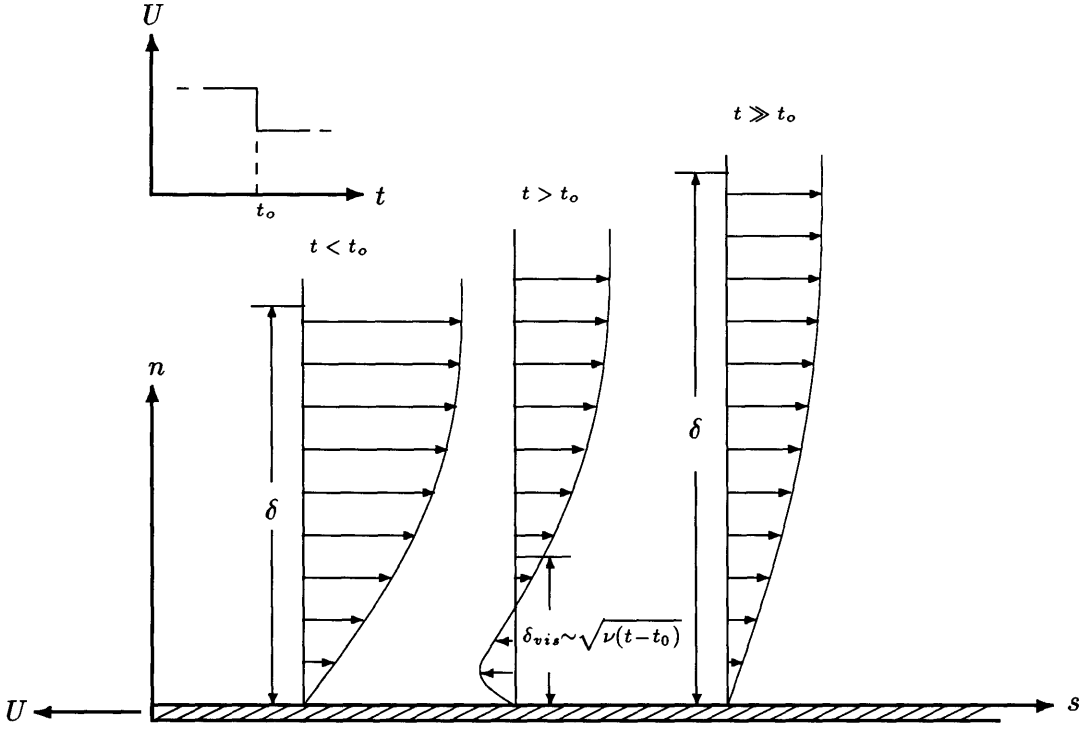

Figure 4.1: Steady boundary layer subject to a discontinuous freestream velocity

Figure 4.1 shows a boundary layer on a flat plate translating to the left in an incompressible fluid. The velocity profiles are given in a frame of reference fixed to the plate. At $t=t_o$, its velocity changes discontinuously. In the outer region far from the wall, the initial response will be a shift of the velocity profile. Generation of vorticity is confined

to the wall and spreads out with a rate characterized by the viscous time constant T_{vis},

$$T_{vis} = \frac{\delta^2}{\nu}, \tag{4.1}$$

where δ represents the boundary layer thickness. T_{vis} gives the time it takes viscous effects to make themselves felt across the boundary layer. The normal distance to which viscous effects have spread within a set time is characterized by the viscous length scale

$$\delta_{vis} \sim \sqrt{\nu\,(t - t_0)}. \tag{4.2}$$

An isentropic pressure (velocity) disturbance in the freestream will have a similar effect on a stationary flat plate. Since an isentropic pressure disturbance does not change the local vorticity in an incompressible flow, the initial response in the outer region will again be a mere shift of the velocity profile, while viscous effects spread out from the boundary. For compressible boundary layers with non-aligned static pressure and density gradients, vorticity will also be created within the boundary layer, but this just slightly modifies the above description.

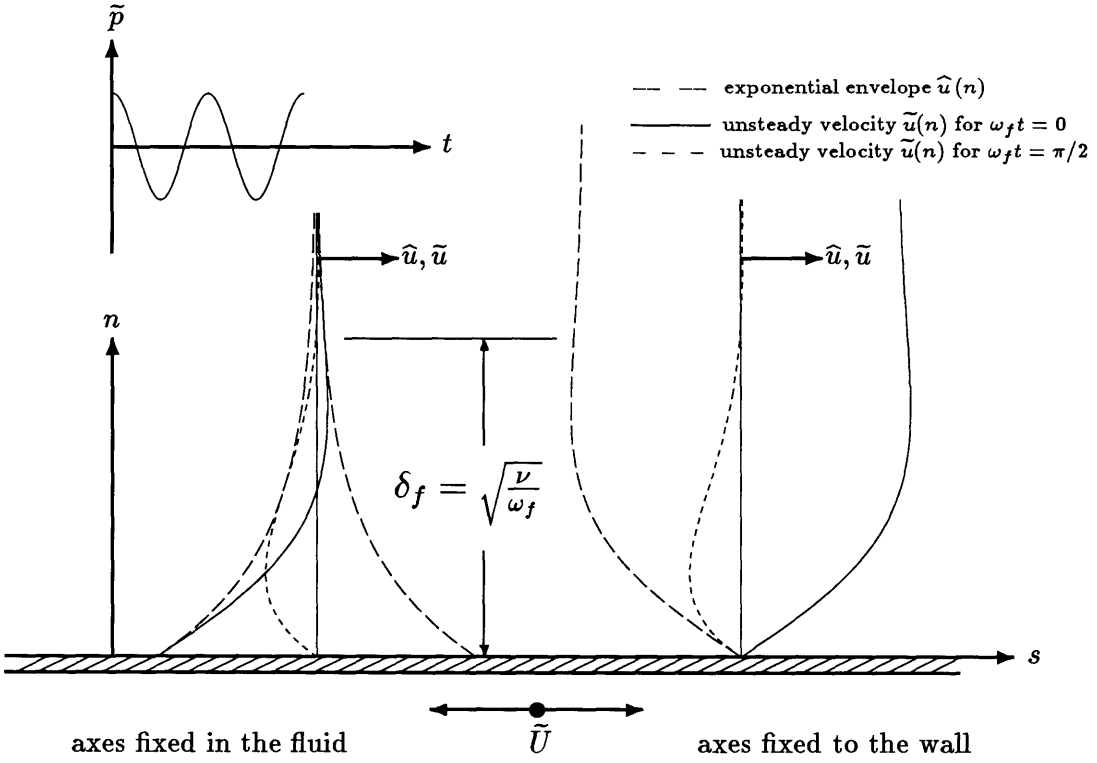

Figure 4.2: Unsteady boundary layer on an oscillating wall

The unsteady velocity distribution induced by a wall oscillating harmonically with forcing frequency ω_f, i.e. Stokes' second problem, is depicted in figure 4.2. In the left half of figure 4.2, the velocity distribution, as seen in the stationary frame of reference, has been sketched for two particular instants during a period T_f. Analogous to the previous example, one can define a length scale to characterize the extent to which unsteady viscous effects spread into the flow during a period.

$$\delta_f = \sqrt{\frac{\nu}{\omega_f}} \sim \sqrt{\nu T_f} \tag{4.3}$$

The right half of the figure shows the unsteady velocity distribution in the frame of reference fixed to the plate. The same velocity distribution relative to a frame of reference fixed to the plate can be obtained by allowing the freestream static pressure gradient to vary harmonically with forcing frequency ω_f, if the characteristic length l_f of the pressure disturbance is much larger than the unsteady boundary layer thickness.

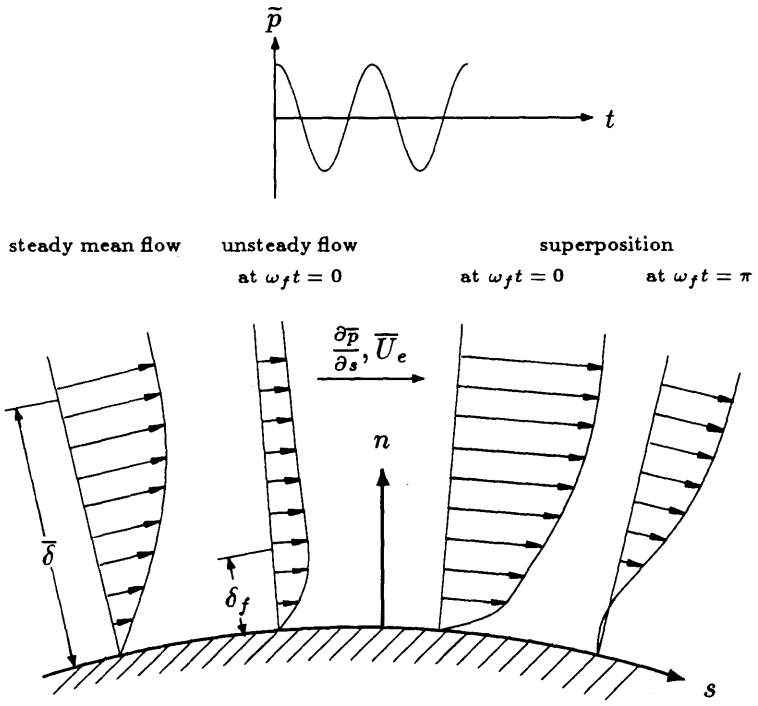

Figure 4.3: Unsteady boundary layer on a blade surface

In a turbomachine, figure 4.3, one will have both a steady and an unsteady boundary layer together with a mean-flow pressure gradient, and a freestream which no longer

satisfies $M_e \ll 1$; the forcing frequency becomes the blade passing frequency or one of its higher harmonics. The unsteady stator/rotor interaction can generate strong pressure waves. In the immediate neighborhood of the wall, a harmonic pressure disturbance will still induce an unsteady velocity distribution as found in Stokes' second problem of figure 4.2 for sufficiently high reduced frequencies [79][1] Away from the wall, the unsteady velocities will increasingly be influenced by the non-zero (and generally turbulent) mean flow and, possibly, compressibility effects. In the outer region beyond the boundary layer, the response to a harmonic pressure disturbance will be purely potential.

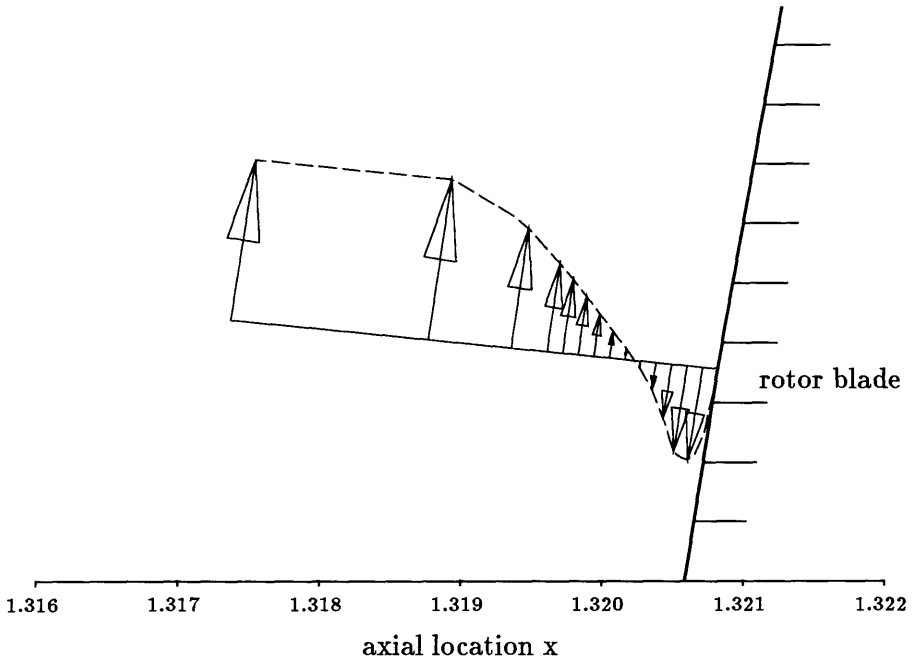

Figure 4.4: Unsteady boundary layer on a blade — simulation of the ACE turbine stage at $(t/T) = 0.9$

Unsteady boundary layers, including regions of reversed attached flow[2] have been observed in numerical simulations. Figure 4.4 shows instantaneous velocity vectors in the boundary layer on the rotor of the ACE turbine stage introduced in section 2.7; the location is near the leading edge of the rotor blade, marked by an arrow in figure 2.12.

[1] see section 4.3

[2] For a definition of unsteady separation and unsteady reversed, attached flows consult [78].

The locus and the mechanism of unsteady (viscous) dissipation are of pivotal importance to this chapter. The energy associated with the unsteady part of the flow field is dissipated either in the freestream or in unsteady boundary layers at the blades, the hub and the tip. To compare the relative importance of these two loss mechanisms, the following order-of-magnitude argument in laminar flow is instructive:

In the freestream, the velocity gradient is set by the unsteady velocity $\vec{\tilde{U}}_e = [\tilde{u}_e, \tilde{v}_e]^T$, and the characteristic length l_f of the disturbance.

$$\left|\nabla \vec{\tilde{U}}_e\right| \sim \left|\frac{\tilde{U}_e}{l_f}\right| \tag{4.4}$$

The subscript e denotes a quantity in the freestream (at the edge of the boundary layer). If one assumes the presence of (linear) entropy waves, vorticity waves or pressure waves (propagating approximately in or against the freestream direction), the characteristic lengths become the wavelengths $\lambda_{f,i}$

$$\begin{aligned} \frac{\lambda_{f1,2}}{c_a} &= \frac{2\pi}{k_e}, \\ \text{and} \quad \frac{\lambda_{f3,4}}{c_a} &= \frac{2\pi}{k_e}\frac{(1 \pm M_e)}{M_e}, \end{aligned} \tag{4.5}$$

and $\vec{\tilde{U}}_e$ is replaced by $\tilde{u}_e$. The reduced frequency k_e is defined in terms of the blade passing frequency ω_f, the local mean velocity in the freestream $\overline{U}_e$, and the blade axial chord c_a as

$$k_e = \frac{\omega_f c_a}{\overline{U}_e}. \tag{4.6}$$

Near the wall, a harmonic disturbance will give rise to an unsteady boundary layer of a thickness characterized by δ_f and hence

$$\left|\frac{\partial \tilde{u}}{\partial n}\right| \sim \left|\frac{\tilde{u}_e}{\delta_f}\right|. \tag{4.7}$$

To obtain a meaningful measure of dissipation, one has to integrate (the time-means of) the unsteady dissipation functions (which are proportional to the viscosity and the squares of the above velocity gradients) to account for the different extents of boundary layer and freestream. Assuming that a wave typically travels one axial chord between

reflections, one finds that viscous dissipation in the freestream is negligible if

$$\left(\frac{\delta_f}{\lambda_f}\right)^2 \left(\frac{c}{\delta_f}\right) \ll 1. \tag{4.8}$$

With the definition of the unsteady boundary layer thickness δ_f in (4.3) and equations (4.5), one can rewrite equation (4.8) as

$$\frac{1}{4\pi^2}\, k_e \sqrt{\frac{k_e}{Re}} \ll 1,$$

$$\text{and} \quad \frac{1}{4\pi^2}\, k_e \sqrt{\frac{k_e}{Re}} \frac{M_e^2}{(1 \pm M_e)^2} \ll 1, \tag{4.9}$$

where the Reynolds number defined by $Re = (\rho_e \overline{U}_e c_a / \mu_e)$. For the Reynolds numbers encountered in turbomachinery applications, this inequality is easily satisfied. Thus, the locus of unsteady viscous dissipation is in unsteady boundary layers, and not in the freestream.

In turbulent flow, the argument is less straightforward, because it depends on the relative level of the turbulent viscosity in the freestream and the boundary layer. However, unless the level of turbulent viscosity in the freestream by far exceeds the one characterizing the boundary layer, inequalities (4.9) still hold.

4.1 Analytical Approach

The initial step in the analytical approach taken in this section is to linearize the governing viscous equations about their time-mean. Taking the first-order perturbation equations to their asymptotic high-reduced-frequency limit at the wall, the momentum equation decouples. Driven by the unsteady pressure gradients, it yields the unsteady streamwise velocity distribution near the wall. With the unsteady velocities in the boundary layer known, the time-mean of the dominating term in the second-order unsteady dissipation function can be calculated and related to a drop in the time-mean isentropic efficiency.

4.1.1 Governing Equations

In the streamline-oriented Cartesian coordinate system (s, n) of figure 4.3, the problem is described by the continuity equation

$$\frac{\partial \rho}{\partial t} + \rho\left(\frac{\partial u}{\partial s} + \frac{\partial v}{\partial n}\right) + u\frac{\partial \rho}{\partial s} + v\frac{\partial \rho}{\partial n} = 0, \tag{4.10}$$

the streamwise momentum equation in conjunction with the stress/strain relations in a Newtonian fluid

$$\frac{\partial u}{\partial t} + u\frac{\partial u}{\partial s} + v\frac{\partial u}{\partial n} = \frac{1}{\rho}\left(-\frac{\partial p}{\partial s} + \frac{\partial \sigma_{ss}}{\partial s} + \frac{\partial \tau_{sn}}{\partial n}\right), \tag{4.11}$$

$$\sigma_{ss} = \mu\frac{2}{3}\left(2\frac{\partial u}{\partial s} - \frac{\partial v}{\partial n}\right) \quad \text{and} \quad \tau_{sn} = \mu\left(\frac{\partial u}{\partial n} + \frac{\partial v}{\partial s}\right), \tag{4.12}$$

the energy equation in conjunction with the definition of the dissipation function

$$\rho c_p\left(\frac{\partial T}{\partial t} + u\frac{\partial T}{\partial s} + v\frac{\partial T}{\partial n}\right) = \frac{\partial p}{\partial t} + u\frac{\partial p}{\partial s} + v\frac{\partial p}{\partial n} + \frac{\partial}{\partial s}\left(\kappa\frac{\partial T}{\partial s}\right) + \frac{\partial}{\partial n}\left(\kappa\frac{\partial T}{\partial n}\right) + \Phi \tag{4.13}$$

and

$$\Phi = \mu\left[2\left(\frac{\partial u}{\partial s}\right)^2 + 2\left(\frac{\partial v}{\partial n}\right)^2 + \left(\frac{\partial v}{\partial s} + \frac{\partial u}{\partial n}\right)^2 - \frac{2}{3}\left(\frac{\partial u}{\partial s} + \frac{\partial v}{\partial n}\right)^2\right], \tag{4.14}$$

and the equation of state

$$p = \rho R T. \tag{4.15}$$

Because of the boundary layer character of the problem under consideration, the normal momentum equation has been replaced by the assumption $(\partial p/\partial n) = 0$.

4.1.2 Linearization

Linearizing the velocity components and the thermodynamic variables around their time-mean, the first-order perturbation equations become

$$\frac{\partial \tilde{\rho}}{\partial t} + \overline{\rho}\left(\frac{\partial \tilde{u}}{\partial s} + \frac{\partial \tilde{v}}{\partial n}\right) + \tilde{\rho}\left(\frac{\partial \overline{u}}{\partial s} + \frac{\partial \overline{v}}{\partial n}\right) + \overline{u}\frac{\partial \tilde{\rho}}{\partial s} + \overline{v}\frac{\partial \tilde{\rho}}{\partial n} + \tilde{u}\frac{\partial \overline{\rho}}{\partial s} + \tilde{v}\frac{\partial \overline{\rho}}{\partial n} = 0, \tag{4.16}$$

$$\frac{\partial \tilde{u}}{\partial t} + \overline{u}\frac{\partial \tilde{u}}{\partial s} + \tilde{u}\frac{\partial \overline{u}}{\partial s} + \overline{v}\frac{\partial \tilde{u}}{\partial n} + \tilde{v}\frac{\partial \overline{u}}{\partial n} =$$

$$= \frac{1}{\overline{\rho}}\left[-\frac{\partial \tilde{p}}{\partial s} + \frac{\partial \tilde{\sigma}_{ss}}{\partial s} + \frac{\partial \tilde{\tau}_{sn}}{\partial n} + \frac{\tilde{\rho}}{\overline{\rho}}\left(\frac{\partial \overline{p}}{\partial s} - \frac{\partial \overline{\sigma}_{ss}}{\partial s} - \frac{\partial \overline{\tau}_{sn}}{\partial n}\right)\right], \tag{4.17}$$

$$\tilde{\sigma}_{ss} = \mu\frac{2}{3}\left(2\frac{\partial\tilde{u}}{\partial s} - \frac{\partial\tilde{v}}{\partial n}\right) \quad \text{and} \quad \tilde{\tau}_{sn} = \mu\left(\frac{\partial\tilde{u}}{\partial n} + \frac{\partial\tilde{v}}{\partial s}\right), \tag{4.18}$$

$$\overline{\rho}c_p\left(\frac{\partial\tilde{T}}{\partial t} + \overline{u}\frac{\partial\tilde{T}}{\partial s} + \overline{v}\frac{\partial\tilde{T}}{\partial n} + \tilde{u}\frac{\partial\overline{T}}{\partial s} + \tilde{v}\frac{\partial\overline{T}}{\partial n}\right) + \tilde{\rho}c_p\left(\overline{u}\frac{\partial\overline{T}}{\partial s} + \overline{v}\frac{\partial\overline{T}}{\partial n}\right) =$$

$$= \frac{\partial\tilde{p}}{\partial t} + \overline{u}\frac{\partial\tilde{p}}{\partial s} + \overline{v}\frac{\partial\tilde{p}}{\partial n} + \tilde{u}\frac{\partial\overline{p}}{\partial s} + \tilde{v}\frac{\partial\overline{p}}{\partial n} + \frac{\partial}{\partial s}\left(k\frac{\partial\tilde{T}}{\partial s}\right) + \frac{\partial}{\partial n}\left(k\frac{\partial\tilde{T}}{\partial n}\right) + \tilde{\Phi}_1, \tag{4.19}$$

$$\tilde{\Phi}_1 = 2\mu\left[2\frac{\partial\overline{u}}{\partial s}\frac{\partial\tilde{u}}{\partial s} + 2\frac{\partial\overline{v}}{\partial n}\frac{\partial\tilde{v}}{\partial n} + \right.$$

$$\left. + \left(\frac{\partial\overline{v}}{\partial s} + \frac{\partial\overline{u}}{\partial n}\right)\left(\frac{\partial\tilde{v}}{\partial s} + \frac{\partial\tilde{u}}{\partial n}\right) - \frac{2}{3}\left(\frac{\partial\overline{u}}{\partial s} + \frac{\partial\overline{v}}{\partial n}\right)\left(\frac{\partial\tilde{u}}{\partial s} + \frac{\partial\tilde{v}}{\partial n}\right)\right], \tag{4.20}$$

and

$$\tilde{T} = \frac{1}{\overline{\rho}R}\left(\tilde{p} - \frac{\overline{a}^2}{\gamma}\tilde{\rho}\right). \tag{4.21}$$

The laminar viscosity μ and the laminar thermal conductivity κ have been assumed to remain constant at their mean values in the freestream.

4.1.3 Nondimensionalization

All variables are normalized using time-mean quantities at the boundary layer edge and the blade axial chord.

$$\begin{aligned} u &\rightarrow \frac{u}{\overline{U}_e} & v &\rightarrow \frac{v}{\overline{U}_e} \\ p &\rightarrow \frac{p}{\overline{\rho}_e\overline{U}_e^2} & T &\rightarrow \frac{T}{\overline{T}_e} & \rho &\rightarrow \frac{\rho}{\overline{\rho}_e} \\ s &\rightarrow \frac{s}{c_a} & n &\rightarrow \frac{n}{c_a} & t &\rightarrow \omega_f t \end{aligned} \tag{4.22}$$

With this nondimensionalization, the linearized equations may be written as

$$k_e\frac{\partial\tilde{\rho}}{\partial t} + \overline{\rho}\left(\frac{\partial\tilde{u}}{\partial s} + \frac{\partial\tilde{v}}{\partial n}\right) + \tilde{\rho}\left(\frac{\partial\overline{u}}{\partial s} + \frac{\partial\overline{v}}{\partial n}\right) + \overline{u}\frac{\partial\tilde{\rho}}{\partial s} + \overline{v}\frac{\partial\tilde{\rho}}{\partial n} + \tilde{u}\frac{\partial\overline{\rho}}{\partial s} + \tilde{v}\frac{\partial\overline{\rho}}{\partial n} = 0, \tag{4.23}$$

$$k_e\frac{\partial\tilde{u}}{\partial t} + \overline{u}\frac{\partial\tilde{u}}{\partial s} + \tilde{u}\frac{\partial\overline{u}}{\partial s} + \overline{v}\frac{\partial\tilde{u}}{\partial n} + \tilde{v}\frac{\partial\overline{u}}{\partial n} =$$

$$= -\frac{1}{\overline{\rho}}\frac{\partial\tilde{p}}{\partial s} + \frac{1}{\overline{\rho}}\left(\frac{\partial\tilde{\sigma}_{ss}}{\partial s} + \frac{\partial\tilde{\tau}_{sn}}{\partial n}\right) + \frac{\tilde{\rho}}{\overline{\rho}^2}\frac{\partial\overline{p}}{\partial s} - \frac{\tilde{\rho}}{\overline{\rho}^2}\left(\frac{\partial\overline{\sigma}_{ss}}{\partial s} + \frac{\partial\overline{\tau}_{sn}}{\partial n}\right), \tag{4.24}$$

$$\tilde{\sigma}_{ss} = \frac{1}{Re}\frac{2}{3}\left(2\frac{\partial\tilde{u}}{\partial s} - \frac{\partial\tilde{v}}{\partial n}\right) \quad \text{and} \quad \tilde{\tau}_{sn} = \frac{1}{Re}\left(\frac{\partial\tilde{u}}{\partial n} + \frac{\partial\tilde{v}}{\partial s}\right), \tag{4.25}$$

$$\overline{\rho}\left(k_e\frac{\partial\tilde{T}}{\partial t} + \overline{u}\frac{\partial\tilde{T}}{\partial s} + \tilde{u}\frac{\partial\overline{T}}{\partial s} + \overline{v}\frac{\partial\tilde{T}}{\partial n} + \tilde{v}\frac{\partial\overline{T}}{\partial n}\right) + \tilde{\rho}\left(\overline{u}\frac{\partial\overline{T}}{\partial s} + \overline{v}\frac{\partial\overline{T}}{\partial n}\right) =$$

$$= (\gamma - 1) M_e^2 \left[k_e \frac{\partial \tilde{p}}{\partial t} + \overline{u} \frac{\partial \tilde{p}}{\partial s} + \overline{v} \frac{\partial \tilde{p}}{\partial n} + \tilde{u} \frac{\partial \overline{p}}{\partial s} + \tilde{v} \frac{\partial \overline{p}}{\partial n} \right] +$$

$$+ \frac{1}{PrRe} \left[\frac{\partial}{\partial s} \left(\mu \frac{\partial \tilde{T}}{\partial s} \right) + \frac{\partial}{\partial n} \left(\mu \frac{\partial \tilde{T}}{\partial n} \right) \right] + \tilde{\Phi}_1, \quad (4.26)$$

$$\tilde{\Phi}_1 = \frac{2}{Re} \left[2 \frac{\partial \overline{u}}{\partial s} \frac{\partial \tilde{u}}{\partial s} + 2 \frac{\partial \overline{v}}{\partial n} \frac{\partial \tilde{v}}{\partial n} + \left(\frac{\partial \overline{v}}{\partial s} + \frac{\partial \overline{u}}{\partial n} \right) \left(\frac{\partial \tilde{v}}{\partial s} + \frac{\partial \tilde{u}}{\partial n} \right) - \right.$$

$$\left. - \frac{2}{3} \left(\frac{\partial \overline{u}}{\partial s} + \frac{\partial \overline{v}}{\partial n} \right) \left(\frac{\partial \tilde{u}}{\partial s} + \frac{\partial \tilde{v}}{\partial n} \right) \right], \quad (4.27)$$

and

$$\tilde{T} = \frac{1}{\overline{\rho}} \left(\gamma M_e^2 \tilde{p} - \frac{\tilde{\rho}}{\overline{\rho}} \right). \quad (4.28)$$

To arrive at the nondimensional energy equation (4.26), the definition of the Prandtl number,

$$Pr = \mu \frac{c_p}{\kappa}, \quad (4.29)$$

has been used.

4.1.4 High-Reduced-Frequency Limit

The high-reduced-frequency limit is characterized by a reduced frequency

$$k_e \gg 1. \quad (4.30)$$

The reduced frequencies of modern turbomachines typically are at the upper end of the middle-frequency range ($0.05 < k_e < 5$). The low-frequency limit clearly does not apply. The high-reduced-frequency limit may only strictly apply for disturbances at higher harmonics of the blade passing frequency. Here, the high-reduced-frequency limit includes the inequalities

$$\delta_f / \overline{\delta} \ll 1, \quad (4.31)$$

$$\lambda_f / c_a \ll 1, \quad (4.32)$$

and

$$\delta_f / \lambda_f \ll 1. \quad (4.33)$$

Inequality (4.31) states that normal derivatives of unsteady quantities dominate over normal derivatives of steady quantities, because the unsteady boundary layer is much thinner than its steady counterpart. Inequality (4.32) allows one to neglect streamwise

mean-flow derivatives because the wavelength of the disturbance is much less than the blade axial chord. Inequality (4.33) states that the wavelength of the disturbance is far greater than the unsteady boundary layer thickness. It allows for the neglect of unsteady streamwise derivatives in the presence of unsteady normal derivatives and for the assumption of $(\partial\tilde{p}/\partial n)=0$. Together, inequalities (4.32) and (4.33) imply that the length scale describing the evolution of the steady boundary layer (the blade axial chord), as well as the wavelength, are much larger than the thickness of the unsteady boundary layer. In other words, parallel mean flow can be assumed because both the steady boundary layer and the driving disturbance appear constant on the length scale of the unsteady boundary layer. The errors incurred by the application of the high-reduced-frequency limit in turbomachinery flows are addressed in sections 4.2 and 4.3.

Inequalities (4.31) to (4.33) implicitly depend on the reduced frequency. For simplicity, consider a laminar boundary layer on a flat plate with zero mean pressure gradient. The mean boundary layer thickness is approximately

$$\frac{\overline{\delta}}{s} \approx \frac{5}{\sqrt{Re_s}}, \tag{4.34}$$

where Re_s is the Reynolds number formed with the local distance from the leading edge. Assuming that the unsteadiness consists of pressure waves (propagating approximately in or against the freestream), inequalities (4.31) to (4.33) take on the form

$$\frac{\delta_f}{\overline{\delta}} \approx \frac{1}{5}\sqrt{\frac{1}{k_e}} \ll 1, \tag{4.35}$$

$$\frac{\lambda_f}{c_a} \approx \frac{2\pi}{k_e}\,\frac{(1 \pm M_e)}{M_e} \ll 1, \tag{4.36}$$

$$\text{and} \quad \frac{\delta_f}{\lambda_f} \approx \frac{5}{2\pi}\sqrt{\frac{k_e}{Re}}\,\frac{M_e}{(1 \pm M_e)} \ll 1 \tag{4.37}$$

in the high-frequency limit. To derive the last two relations, the definition of the wavelength $\lambda_{3,4}$ (4.5) has been used. Inequalities (4.35) and (4.36) hold for high reduced frequencies and may only be strictly satisfied for higher harmonics of the blade passing frequency. Inequality (4.37) is least critical because it relies on the large Reynolds number in turbomachinery. A typical value of the Reynolds number in modern turbomachinery is $Re_s \approx O(10^6)$.

4.1.5 High-Frequency Limit of the Momentum Equation

Applying the inequalities of subsection 4.1.4 to the normalized momentum equation (4.24), the following terms drop out:

$$k_e\frac{\partial\tilde{u}}{\partial t}+\overline{u}\frac{\partial\tilde{u}}{\partial s}+\cancel{\tilde{u}\frac{\partial\overline{u}}{\partial s}}^{(4.30,4.32)}+\cancel{\overline{v}\frac{\partial\overline{u}}{\partial n}}^{(4.30,4.32)}+\tilde{v}\frac{\partial\overline{u}}{\partial n}$$

$$=-\frac{1}{\overline{\rho}}\frac{\partial\tilde{p}}{\partial s}+\frac{1}{\overline{\rho}}\left(\cancel{\frac{\partial\tilde{\sigma}_{ss}}{\partial s}}^{(4.33)}+\frac{\partial\tilde{\tau}_{sn}}{\partial n}\right)+\cancel{\frac{\tilde{\rho}}{\overline{\rho}^2}\frac{\partial\overline{p}}{\partial s}}^{(4.32)}-\frac{\tilde{\rho}}{\overline{\rho}^2}\left(\cancel{\frac{\partial\overline{\sigma}_{ss}}{\partial s}}^{(4.32)}+\cancel{\frac{\partial\overline{\tau}_{sn}}{\partial n}}^{(4.31)}\right)$$

$$\tilde{\tau}_{sn}=\frac{1}{Re}\left(\frac{\partial\tilde{u}}{\partial n}+\cancel{\frac{\partial\tilde{p}}{\partial s}}^{(4.33)}\right)$$

The numbers above the arrows refer to inequalities (4.30) to (4.33) and give the reasoning for the neglect of individual terms. Inequalities (4.30) and (4.32) leave the unsteady term and two convective terms dominant on the left-hand side. In the freestream, only first of these convective terms remains; the second will be shown to be the dominant convective term near the wall. On the right-hand side, only the driving unsteady pressure term and the unsteady shear term remain.

4.1.6 Free-Stream and Near-Wall Approximation

In the high-frequency limit near the wall, the momentum equation simplifies further. Due to inequality (4.31), the first of the remaining convective terms becomes small compared to the unsteady term. While the unsteady shear ($\partial u/\partial s$) can be proportional to the reduced frequency k_e, as is the case for a propagating pressure wave, the mean streamwise velocity $\overline{u}$ approaches zero. The second convective term approaches zero because of inequality (4.30) and because the normal velocity perturbation $\tilde{v}$ vanishes at the wall. The high-frequency limit of the momentum equation near the wall becomes

$$k_e\frac{\partial\tilde{u}}{\partial t}-\frac{1}{\overline{\rho}_w}\frac{\partial\tilde{\tau}_{sn}}{\partial n}=-\frac{1}{\overline{\rho}_w}\frac{\partial\tilde{p}}{\partial s}. \tag{4.38}$$

The subscript w denotes a quantity at the wall. With the definition of the unsteady shear stress $\tilde{\tau}_{sn}$, the streamwise momentum equation near the wall can be written as

$$k_e \frac{\partial \tilde{u}}{\partial t} - \frac{1}{Re}\frac{1}{\overline{\rho}_w}\frac{\partial^2 \tilde{u}}{\partial n^2} = -\frac{1}{\overline{\rho}_w}\frac{\partial \tilde{p}}{\partial s} \tag{4.39}$$

in laminar flow. Equation (4.39) describes a Stoke's layer driven by an unsteady pressure gradient.

In the freestream, normal derivatives of steady quantities vanish and the streamwise momentum equation takes the form

$$k_e \frac{\partial \tilde{u}}{\partial t} + \frac{\partial \tilde{u}}{\partial s} = -\frac{\partial \tilde{p}}{\partial s} \tag{4.40}$$

in laminar flow. Note that the mean streamwise velocity $\overline{u}$ approaches unity in the freestream.

4.1.7 Streamwise Velocities in the High-Frequency Limit

Since (4.39) and (4.40) are linear constant coefficient equations, the principle of superposition can be used. Any disturbance can be decomposed into its individual (temporal) Fourier modes. After the solutions to the individual modes have been found, the response to the original disturbance may be obtained by superposition. The driving pressure disturbance, decomposed into its individual modes, is given by

$$\tilde{p} = \sum_{m=1}^{\infty} \hat{p}_m(s)\ e^{-imt}. \tag{4.41}$$

This is the form which will be used when the loss model is driven by unsteady pressure gradients obtained from a simulation. To evaluate the accuracy of the analytic loss model or the modeling accuracy of numerical simulations, a propagating (or convected) disturbance of the form

$$\tilde{p} = \sum_{m=1}^{\infty} \hat{p}_m\ \exp\{im\,(k_s s - t)\} \tag{4.42}$$

will be used. The variable $\hat{p}_m$ denotes the complex amplitude of the mth time-harmonic

of the static pressure, and k_s the streamwise wavenumber of the first harmonic[3]. The same functional forms, (4.41) or (4.42), are assumed for all linearized variables. For the mth harmonic, the solution in the viscous Stoke's sublayer near the wall is

$$\widetilde{u}_m = -\frac{1}{\overline{\rho}_w}\frac{1}{k_e}\frac{i}{m}\left(1-\exp\left\{-(1-i)\sqrt{\frac{mk_e\overline{\rho}_w}{2}\,Re}\;\;n\right\}\right)\frac{\partial\widehat{p}_m}{\partial s}\,e^{-imt} \tag{4.43}$$

for a pressure disturbance of the form (4.41), and

$$\widetilde{u}_m = \frac{1}{\overline{\rho}_w}\frac{k_s}{k_e}\left(1-\exp\left\{-(1-i)\sqrt{\frac{mk_e\overline{\rho}_w}{2}\,Re}\;\;n\right\}\right)\widehat{p}_m\,\exp\{im(k_s s-t)\} \tag{4.44}$$

for a wave-type disturbance (4.42). The first exponent in equations (4.43) and (4.44) can be rewritten as

$$-(1-i)\sqrt{\frac{mk_e\overline{\rho}_w}{2}\,Re}\;\;n = -(1-i)\sqrt{\frac{m}{2}}\,\frac{n}{\delta_f} \tag{4.45}$$

in terms of the unsteady boundary layer thickness δ_f.

Far from the wall, the unsteady velocity asymptotes to

$$\widetilde{u} = \frac{k_s}{k_e-k_s}\,\widehat{p}_m\,\exp\{im(k_s s-t)\} \tag{4.46}$$

for a wave-type disturbance.

Figure 4.5 illustrates the above solutions for an upstream propagating wave over a laminar (adiabatic) flat plate at zero pressure gradient. The 'exact' solution was obtained by solving the linearized equations (4.70) to (4.75) discussed in the numerical evaluation of modeling errors in section 4.3. In the viscous Stokes sublayer close to the wall, the velocity distribution is well represented by equation (4.44). The agreement increases with the ratio $(\overline{\delta}/\delta_f)$ and decreases with the Mach number, because equation (4.39) assumes zero mean flow at the edge of the unsteady boundary layer and an incompressible mean flow. Due to the neglect of the convection, which becomes important away from the wall, it asymptotes to the wrong unsteady velocity. The correct magnitude of the unsteady velocity in the freestream is given by equation (4.46).

[3] In keeping with the high-frequency limit, inequality (4.33), and the boundary layer approximation, $(\partial\overline{p}/\partial n)=(\partial\widetilde{p}/\partial n)=0$, the normal dependence of the unsteady pressure through a wavenumber k_n has been omitted.

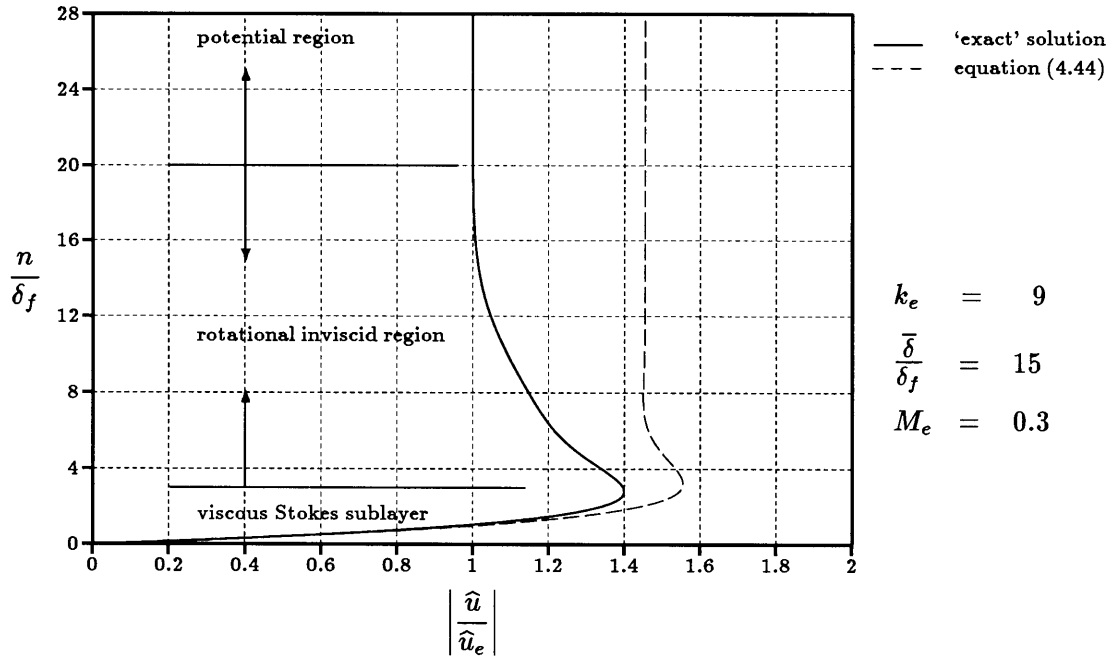

Figure 4.5: Unsteady streamwise velocity distribution as a function of the wall distance

4.1.8 Unsteady Dissipation

Note that the linearized dissipation function $\widetilde{\Phi}_1$ (4.27) has a zero time-mean. The extra unsteady dissipation with non-zero time-mean, $\widetilde{\Phi}_2$, is of second order; it is obtained from the definition of the dissipation function (4.14).

$$\widetilde{\Phi}_2 = \frac{1}{Re}\left[2\left(\frac{\partial \widetilde{u}}{\partial s}\right)^2 + 2\left(\frac{\partial \widetilde{v}}{\partial n}\right)^2 + \left(\frac{\partial \widetilde{v}}{\partial s} + \frac{\partial \widetilde{u}}{\partial n}\right)^2 - \frac{2}{3}\left(\frac{\partial \widetilde{u}}{\partial s} + \frac{\partial \widetilde{v}}{\partial n}\right)^2\right] \tag{4.47}$$

Applying inequalities (4.30) to (4.33) and remembering that $\widetilde{v} \ll \widetilde{u}$ in the unsteady boundary layer, the following terms can be neglected in the high-frequency limit:

$$\widetilde{\Phi}_2 = \frac{1}{Re}\left[2\left(\frac{\partial \widetilde{v}}{\partial s}\right)^{2\,(4.33)} + 2\left(\frac{\partial \widetilde{v}}{\partial n}\right)^2_{(\widetilde{v}\ll\widetilde{u})} + \left(\frac{\partial \widetilde{v}}{\partial s}\right)^{2\,(4.33)} + \frac{\partial \widetilde{u}}{\partial n}\right)^2 - \frac{2}{3}\left(\frac{\partial \widetilde{u}}{\partial s}\right)^{(4.33)} + \frac{\partial \widetilde{v}}{\partial n}\right)^2_{(\widetilde{v}\ll\widetilde{u})}\Bigg]$$

The dominating contribution in the high-frequency limit comes from the normal derivative of the unsteady streamwise velocity.

$$\widetilde{\Phi}_2 = \frac{1}{Re}\left(\frac{\partial \widetilde{u}}{\partial n}\right)^2 \tag{4.48}$$

Taking the time mean of (4.48),

$$\overline{\tilde{\Phi}}_2 = \frac{1}{2\pi}\int_0^{2\pi} \tilde{\Phi}_2 \, dt = \frac{1}{Re} \overline{\left[\sum_{m1=1}^{\infty} \Re\left(\frac{\partial \tilde{u}_{m1}}{\partial n}\right)\right]\left[\sum_{m2=1}^{\infty} \Re\left(\frac{\partial \tilde{u}_{m2}}{\partial n}\right)\right]}, \tag{4.49}$$

one obtains

$$\overline{\tilde{\Phi}}_2 = \frac{1}{Re} \sum_{m=1}^{\infty} \overline{\left[\Re\left(\frac{\partial \tilde{u}_m}{\partial n}\right)\right]^2} = \frac{1}{2Re} \sum_{m=1}^{\infty} \left|\frac{\partial \tilde{u}_m}{\partial n}\right|^2 . \tag{4.50}$$

Due to the orthogonality of harmonic functions (appendix C), the time-mean of the unsteady dissipation may be calculated mode by mode and summed subsequently. With equation (4.43), the dissipation function (4.50) can be rewritten in the form

$$\overline{\tilde{\Phi}}_{2,m} = \frac{1}{2mk_e\overline{\rho}_w} \left|\frac{\partial \hat{p}_m}{\partial s}\right|^2 \exp\left\{-\sqrt{2m}\frac{n}{\delta_f}\right\} \tag{4.51}$$

for the mth harmonic; it gives the time-mean dissipation per unit volume induced by the mth harmonic of the pressure disturbance. Since the major part of the dissipation occurs in the region of high gradients near the wall, equation (4.51) is integrated from the wall into the freestream to obtain the losses per unit surface area due to the mth harmonic.

$$\overline{\tilde{\Phi}}_{2i,m} = \frac{1}{2\pi}\int_0^{2\pi}\left[\int_0^{\infty} \tilde{\Phi}_{2,m}\, dn\right] dt = \frac{1}{2mk_e\overline{\rho}_w}\sqrt{\frac{1}{2mk_e\overline{\rho}_w}\frac{1}{Re}}\left|\frac{\partial \hat{p}_m}{\partial s}\right|^2 \tag{4.52}$$

For a propagating-wave-type disturbance (4.42), equation (4.52) takes the form

$$\overline{\tilde{\Phi}}_{2i,m} = \frac{1}{2\pi}\int_0^{2\pi}\left[\int_0^{\infty} \tilde{\Phi}_m\, dn\right] dt = \frac{1}{2\overline{\rho}_w}\left(\frac{k_s}{k_e}\right)^2\sqrt{\frac{mk_e}{2\overline{\rho}_w}\frac{1}{Re}}\ |\hat{p}_m|^2 \sim (mk_e)^{\frac{1}{2}} . \tag{4.53}$$

Figure 4.6 compares the rate of dissipation per unit volume rate of the 'exact' solution and the high-frequency-limit solution depicted in figure 4.5. The 'exact' solution was calculated from the full second-order dissipation function (4.47). The high-frequency-limit solution includes only the dominant term. The difference in the integrated dissipation rate $\overline{\tilde{\Phi}}_2$ in figure 4.6 is about 10% of the 'exact' solution for this choice of parameters.

In the high-frequency limit, the normal distribution of the unsteady velocity and the dissipation rate depend only on local quantities. It is $\overline{\tilde{\Phi}}_{2i,m}$, in conjunction with the local mean flow state at the wall, that is necessary to calculate the total pressure loss and the entropy rise per unit surface area. In order to evaluate the unsteady dissipation,

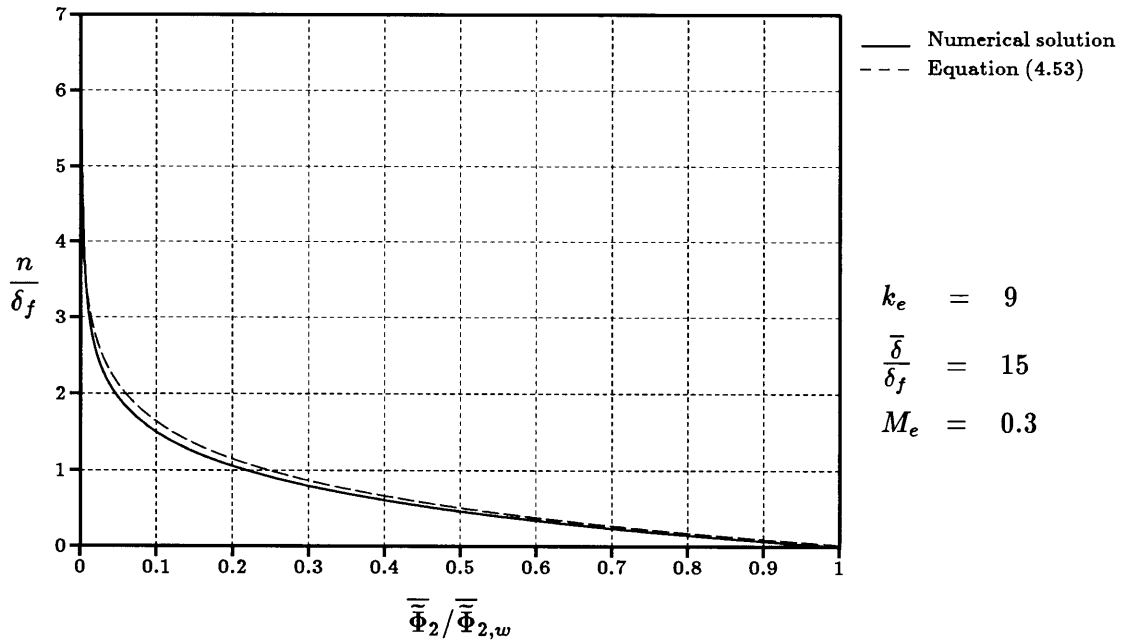

Figure 4.6: Dissipation rate for the 'exact' solution and the high-frequency limit

the Fourier modes of the driving static pressure or static pressure gradient along a blade surface need to be known. These may be the result of an experiment or a numerical simulation. In the latter case the algorithm does not have to include viscous effects. Unless the unsteadiness is related to viscosity (or significantly affected by it), an inviscid simulation will suffice[4]

4.1.9 Unsteady Viscous Loss and Efficiency

The results of section 2.5, relating the dissipation of unsteady waves to the efficiency via an entropy rise and a total pressure loss, are not immediately applicable to the result of subsection 4.1.8. First of all, the dissipation of (energy associated with) unsteady (pressure) waves does not happen at a constant mean flow state. Instead of being dissipated beyond the outlet of the stage, the energy is dissipated within the blade passage. Secondly, due to the reheat effect, the total pressure loss and the entropy rise are less than for a case in which the same amount of energy is dissipated beyond the

[4]Boundary layers at the trailing edge, for example, will likely alter the unsteady circulation response to potential perturbations.

outlet. Part of the dissipation can be recovered because it was turned into heat at a pressure level higher than the outlet pressure.

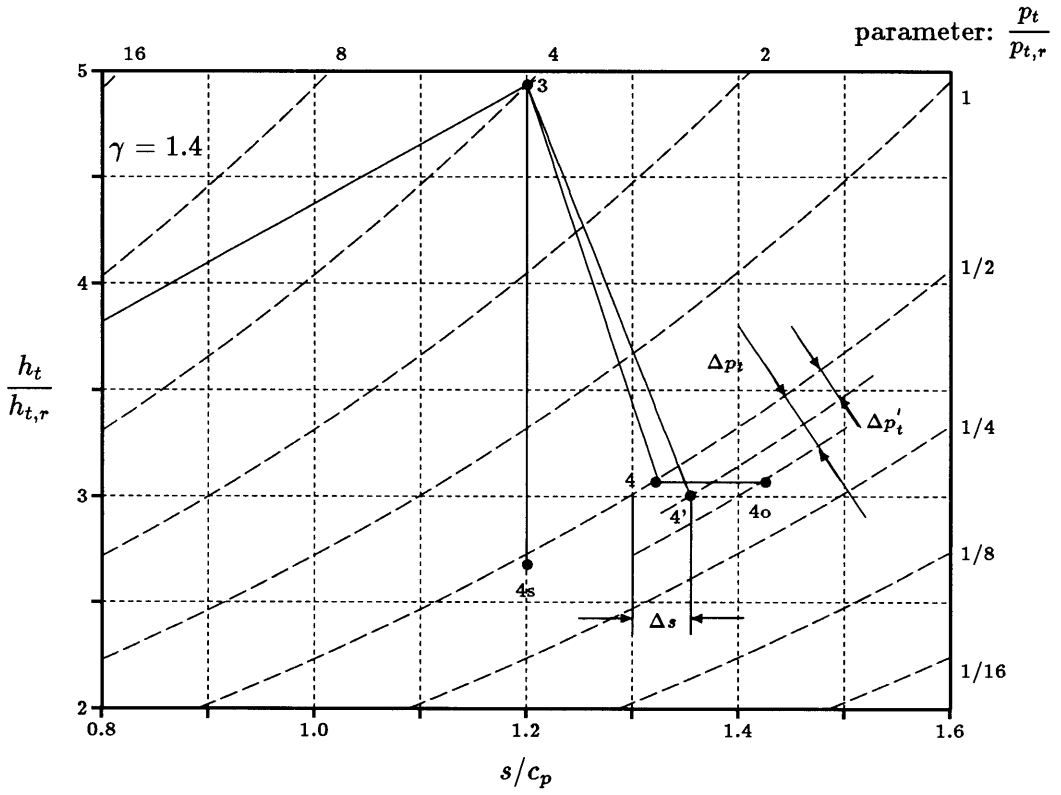

Figure 4.7: $h_t - s$ diagram for an ideal gas — revisited and magnified

The h-s diagram is slightly modified from figure 2.6. Figure 4.7 illustrates the changes for a turbine; all quantities have to be interpreted as time-mean mass-averages. The line connecting points 3 and 4 represents an expansion during which no unsteady modes are dissipated within the blade passage. The dissipation happens beyond the outlet at constant total temperature between points 3 and $4o$. None of this dissipation can be recovered. In the presence of Unsteady Viscous Loss in the blade boundary layers, line $3-4'$, the entropy rise is slightly higher. Due to the reheat effect of dissipation at a temperature above the outlet temperature, part of the dissipated energy, put into the mean flow in the form of heat, can be recovered and turned into mechanical work. Consequently, the difference in total enthalpy (total temperature) along path $3-4'$ must be slightly larger than along path $3-4-4o$; the total pressure loss $\Delta p_t'$ is less than the one which would have occurred if the same amount of energy had been dissipated at the outlet pressure.

In equation (2.38) of subsection 2.3.2, the entropy rise is written in terms of the primitive variables associated with individual unsteady waves. For the unsteady loss mechanism considered here, the dissipated energy is known directly from the second-order dissipation function (4.52) in the unsteady boundary layer. The time-mean of the mass-average specific entropy rise is

$$\Delta\overline{s}_m = \oint \frac{d\overline{q}_m}{c_p\overline{T}_w} = \frac{1}{P\,\overline{\rho u}} \oint \frac{d\overline{\tilde{\Phi}}_{2i,m}}{c_p\overline{T}_w}, \tag{4.54}$$

with the average mass-flux $\overline{\rho u}$ through a blade passage defined as

$$\overline{\rho u} = \int_0^1 \int_0^1 (\rho u)\; d\left(\frac{y}{P}\right)\; d\left(\frac{t}{T}\right). \tag{4.55}$$

This is the entropy rise that results from the dissipation of energy associated with unsteady waves in unsteady boundary layers. The reheat effect is captured by the mean static temperature at the blade surface, $\overline{T}_w$, in the denominator of equation (4.54). The higher T_w, the less the entropy rises per unit dissipated energy[5]. This entropy rise, or the equivalent total pressure loss,

$$\Delta p'_{t,m} = \frac{\gamma-1}{\gamma} \oint \frac{d\overline{q}_m}{c_p\overline{T}_w} = \frac{\gamma}{\gamma-1}\,\frac{1}{P\,\overline{\rho u}} \oint \frac{d\overline{\tilde{\Phi}}_{2i,m}}{c_p\overline{T}_w}, \tag{4.56}$$

are used to calculate the efficiency drop from equations (2.53) or (2.56).

4.2 Analytical Evaluation of Modeling Errors

A typical value for the reduced frequency in turbomachinery is $k_e \approx 5$. The high-frequency limit cannot be applied without consideration of the errors involved. The analytic error analysis in this section determines which of the neglected convective terms dominate the errors in laminar flow and how they scale with dimensionless parameters. A numerical error analysis in section 4.3 will quantify the effect of the high-frequency limit on the accuracy of the predicted dissipation $\overline{\tilde{\Phi}}_{2i}$ in laminar and turbulent flow.

[5]The dissipation and the resulting frictional heating happen locally in the boundary layer. There will be an additional entropy rise when the associated temperature nonuniformities are smoothed out, but this is a higher-order effect.

4.2.1 Convective Terms in the Momentum Equation — Global

The focus of the analytic error evaluation is the streamwise momentum equation which has decoupled from the continuity equation and the energy equation in the near-wall approximation of the high-frequency limit. In comparison to the retained unsteady term, the neglected convective terms on the left-hand side of the streamwise momentum equation (4.17) have the magnitudes

$$\tilde{u}\frac{\partial \overline{u}}{\partial s}\Big/\frac{\partial \tilde{u}}{\partial t} \sim \frac{\overline{U}_e}{\omega_f c_a} = \frac{1}{k_e}, \tag{4.57}$$

$$\overline{u}\frac{\partial \tilde{u}}{\partial s}\Big/\frac{\partial \tilde{u}}{\partial t} \sim \frac{\overline{U}_e}{\omega_f \lambda_f} = \frac{1}{k_e}\frac{c_a}{\lambda_f}, \tag{4.58}$$

$$\overline{v}\frac{\partial \tilde{u}}{\partial n}\Big/\frac{\partial \tilde{u}}{\partial t} \sim \frac{\overline{V}_e}{\omega_f \delta_f} = \frac{1}{k_e}\frac{\overline{V}_e}{\overline{U}_e}\frac{c_a}{\delta_f}, \tag{4.59}$$

$$\text{and} \quad \tilde{v}\frac{\partial \overline{u}}{\partial n}\Big/\frac{\partial \tilde{u}}{\partial t} \sim \frac{\overline{U}_e}{\omega_f \overline{\delta}}\frac{\tilde{v}_e}{\tilde{u}_e} = \frac{1}{k_e}\frac{\tilde{v}_e}{\tilde{u}_e}\frac{c_a}{\overline{\delta}}. \tag{4.60}$$

These estimates describe the boundary layer as a whole rather than details near the wall. Only the magnitude of the convective terms (4.57) and (4.60) can be estimated easily and their neglect justified in the high-frequency limit. Note that $\tilde{v}_e \ll \tilde{u}_e$ in (4.60). Also, in incompressible flow, where $(\overline{V}_e/\overline{U}_e) \sim (\overline{\delta}/c_a)$, (4.59) can be rewritten as

$$\overline{v}\frac{\partial \tilde{u}}{\partial n}\Big/\frac{\partial \tilde{u}}{\partial t} \sim \frac{1}{\sqrt{k_e}}. \tag{4.61}$$

For a pressure wave (propagating in or against the streamwise direction), (4.58) can be written as

$$\overline{u}\frac{\partial \tilde{u}}{\partial s}\Big/\frac{\partial \tilde{u}}{\partial t} \sim \frac{M_e}{1 \pm M_e}. \tag{4.62}$$

The above estimates suggest that the errors introduced by neglecting the convective terms in the momentum equation are at least of magnitude M_e and $(1/\sqrt{k_e})$, stemming from the neglect of the convective terms (4.58) and (4.59), respectively. In particular, for a propagating pressure wave, the convective term (4.58) can be of the same order of magnitude as the unsteady term, independent of the reduced frequency.

In a typical turbomachinery application, the flow will neither satisfy $M_e \ll 1$, nor will the square root of the reduced frequency satisfy $\sqrt{k_e} \gg 1$. It seems that there is no

merit in applying the proposed loss model in a turbomachinery environment. However, (4.57) to (4.60) pose conditions across the boundary layer as a whole and do not focus on details close to the wall.

4.2.2 Convective Terms in the Momentum Equation — Near the Wall

The emphasis is on the near-wall region because it is there that the unsteady gradients and the unsteady loss are large. From the time-mean continuity equation (4.10) and its first-order perturbation (4.16), one can derive that

$$\overline{u} \sim n, \qquad \widetilde{u} \sim n,$$

$$\overline{v} \sim n^2, \qquad \text{and} \qquad \widetilde{v} \sim n$$

hold for an adiabatic (or isothermal) wall. Also, one finds that the first-order perturbation of the continuity equation near the wall is

$$\frac{\partial \widetilde{v}}{\partial n} \approx -k_e \, \frac{1}{\overline{\rho}} \, \frac{\partial \widetilde{\rho}}{\partial t}. \tag{4.63}$$

All of the neglected convective terms in the linearized momentum equation (4.17) are $O(n^2)$, except for the term $\widetilde{v}(\partial \overline{u}/\partial n)$ which is $O(n)$. Its neglect will cause the largest error in the near-wall region. Using a Taylor series expansion of the unsteady velocity distribution (4.44) at the wall and the continuity equation (4.63), the ratio (4.60) can be written as

$$\widetilde{v}\frac{\partial \overline{u}}{\partial n} \Big/ \frac{\partial \widetilde{u}}{\partial t} \approx \frac{\overline{\rho}_w}{\rho_e} \, \frac{k_e}{k_s} \, \frac{\partial \overline{u}}{\partial n} \, M_e^2 \, \frac{\delta_f}{c_a}. \tag{4.64}$$

For a pressure wave propagating (in or against the freestream) over a laminar flat plate boundary layer with $(\partial \overline{u}/\partial n) \approx 0.332\sqrt{Re/s}$, the argument can be made more precise:

$$\widetilde{v}\frac{\partial \overline{u}}{\partial n} \Big/ \frac{\partial \widetilde{u}}{\partial t} \approx 0.332 \, \frac{M_e \, (1 \pm M_e)}{\sqrt{k_e s}} \tag{4.65}$$

In the high-reduced-frequency limit, the dominant of the neglected convective terms, $\widetilde{v}(\partial \overline{u}/\partial n)$ is of order $O\left(M_e/\sqrt{k_e}\right)$ relative to the unsteady term. Note that the validity of this argument is restricted to the near-wall region; details are found in appendix H.

4.3 Numerical Evaluation of Modeling Errors

While the analytical error considerations in laminar flow provide insight into which of the neglected convective terms dominate the error in the near-wall region and/or the freestream, and how they scale with dimensionless parameters, it was desired to get a quantitative measure of the error in the integrated dissipation $\overline{\tilde{\Phi}}_{2i}$, in particular for turbulent flows.

Due to the magnitude of the Reynolds number, inequality (4.33) is always satisfied for turbomachinery flows encountered in practice. However, since the longest wavelength in a turbomachine is typically on the order of a blade chord, inequality (4.32) may only be valid for higher spatial harmonics. For finite reduced frequency, the unsteady boundary layer starts spreading away from the wall and inequality (4.31) is not satisfied.

4.3.1 Model Problem

In order to quantify the effect of the high-reduced-frequency limit and the near-wall approximation, a FORTRAN-code was written to solve the linearized equations describing a flat plate boundary layer subject to a harmonic pressure disturbance. The pressure disturbance at the boundary layer edge is a pressure wave propagating at an arbitrary non-zero angle θ relative to the surface normal.

As was shown in section 4.2, the two main effects in laminar flow not captured in the loss model proposed in section 4.1 are the unsteady compression of the boundary layer near the wall, and convection in the freestream. In turbulent flow, the proposed loss model can be accurate only if the unsteady boundary layer is confined to the laminar sublayer. All three concerns are addressed by the model problem illustrated in figure 4.8.

As long as $\delta_f \ll c_a$ holds, however, the mean flow appears constant (and parallel) on the length scales characterizing the steady and the unsteady boundary layer. This assumption, together with a small steady and unsteady boundary layer thickness compared to the wavelength, reduces the model problem to one dimension.

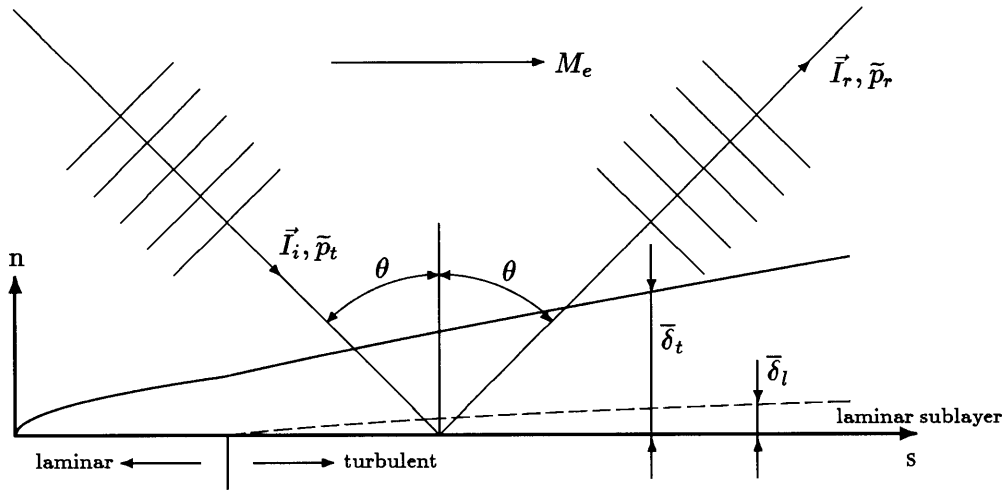

Figure 4.8: Model problem for the numerical evaluation of modeling errors

The incoming and the reflected pressure wave of figure 4.8 are described by

$$\begin{aligned} \tilde{p}_i &= \hat{p} \exp\{i(k_s s - k_n n - i\omega_f t)\} \\ \text{and} \quad \tilde{p}_r &= \hat{p} \exp\{i(k_s s + k_n n - i\omega_f t)\}. \end{aligned} \tag{4.66}$$

The unsteady pressure in the boundary layer is set by the freestream. There, the propagation of a pressure wave is governed by

$$\left(1 - M_e^2\right) \frac{\partial^2 \tilde{p}}{\partial s^2} + \frac{\partial^2 \tilde{p}}{\partial n^2} = 2 \frac{M_e}{\overline{a}_e} \frac{\partial^2 \tilde{p}}{\partial s \partial t} + \frac{1}{\overline{a}_e^2} \frac{\partial^2 \tilde{p}}{\partial t^2}, \tag{4.67}$$

which leads to the dispersion relation

$$\left(\frac{\omega_f}{\overline{a}_e}\right)^2 - 2M_e k_s \left(\frac{\omega_f}{\overline{a}_e}\right) - \left[(1 - M_e^2)k_s^2 + k_n^2\right] = 0, \tag{4.68}$$

and to the nondimensional streamwise wavenumbers

$$k_s = k_e M_e \sin\theta \frac{-M_e \sin\theta \pm \sqrt{1}}{1 - M_e^2 \sin^2\theta}. \tag{4.69}$$

The signs '+' and '−' again correspond to downstream and upstream propagating pressure waves.

Governing Linearized Equation

The linearized equations being solved are obtained from equations (4.16) to (4.21).

$$k_e \frac{\partial \tilde{\rho}}{\partial t} + \overline{\rho}\left(\frac{\partial \tilde{u}}{\partial s} + \frac{\partial \tilde{v}}{\partial n}\right) + \overline{u}\frac{\partial \tilde{\rho}}{\partial s} + \tilde{v}\frac{\partial \overline{\rho}}{\partial n} = 0 \quad (4.70)$$

$$k_e \frac{\partial \tilde{u}}{\partial t} + \overline{u}\frac{\partial \tilde{u}}{\partial s} + \tilde{v}\frac{\partial \overline{u}}{\partial n} = -\frac{1}{\overline{\rho}}\frac{\partial \tilde{p}}{\partial s} + \frac{1}{\overline{\rho}}\frac{\partial \tilde{\tau}_{sn}}{\partial n} - \frac{\tilde{\rho}}{\overline{\rho}^2}\frac{\partial \overline{\tau}_{sn}}{\partial n} \quad (4.71)$$

$$\tilde{\tau}_{sn} = \mu \frac{\partial \tilde{u}}{\partial n} \quad (4.72)$$

$$\overline{\rho} c_p \left(k_e \frac{\partial \tilde{T}}{\partial t} + \overline{u}\frac{\partial \tilde{T}}{\partial s} + \tilde{v}\frac{\partial \overline{T}}{\partial n}\right) = \frac{\partial \tilde{p}}{\partial t} + \overline{u}\frac{\partial \tilde{p}}{\partial s} + \frac{\partial}{\partial s}\left(k\frac{\partial \tilde{T}}{\partial s}\right) + \frac{\partial}{\partial n}\left(k\frac{\partial \tilde{T}}{\partial n}\right) + \tilde{\Phi}_1 \quad (4.73)$$

$$\tilde{\Phi}_1 = \frac{2}{Re}\left(\frac{\partial \tilde{u}}{\partial n} + \frac{\partial \tilde{v}}{\partial s}\right)\frac{\partial \overline{u}}{\partial n} \quad (4.74)$$

$$\tilde{T} = \frac{1}{\overline{\rho}}\left(\gamma M_e^2 \tilde{p} - \frac{\tilde{\rho}}{\overline{\rho}}\right) \quad (4.75)$$

As discussed in section 4.2, equations (4.70) to (4.74) assume parallel mean flow because the (streamwise) evolution of the boundary layer is a higher order effect. In keeping with the high-frequency limit, inequality (4.33), and the boundary layer approximation, the unsteady pressure is assumed constant across the boundary layer. This is implemented by setting the normal wavenumber k_n to zero in equations (4.66).

Boundary Conditions

The boundary condition on the unsteady velocities at the wall is

$$\tilde{u}_w = \tilde{v}_w \equiv 0. \quad (4.76)$$

At an adiabatic wall the condition on the unsteady temperature is

$$\frac{\partial \tilde{T}_w}{\partial n} \equiv 0, \quad (4.77)$$

from which follows

$$\frac{\partial \tilde{\rho}_w}{\partial n} \equiv 0 \quad (4.78)$$

with the boundary layer assumption. For a wall at constant temperature, the boundary condition are

$$\widetilde{T}_w \equiv 0 \quad \text{and} \quad \frac{\widetilde{\rho}_w}{\overline{\rho}_w} = \frac{\widetilde{p}}{\overline{p}}. \tag{4.79}$$

At infinity, the boundary conditions for a wave propagating in the freestream are

$$\widetilde{u}_e = -\widetilde{p}\,\frac{k_s}{k_s - k_e} \quad \text{and} \quad \frac{\partial \widetilde{v}_e}{\partial n} = 0, \tag{4.80}$$

$$\widetilde{T}_e = \frac{\gamma - 1}{\gamma}\,\frac{\widetilde{p}}{\overline{p}}, \quad \text{and} \quad \widetilde{\rho}_e = \frac{1}{\gamma}\frac{\widetilde{p}}{\overline{p}}. \tag{4.81}$$

Mean Flow Profiles

All mean profiles were taken to be identical to the corresponding profiles in steady flow. In experiments, for example [79, 80], the mean flow has generally been found to be unaffected by the oscillations, even for finite disturbance amplitudes. Exceptions to this behavior have been observed at high frequencies close to the turbulent bursting frequency and for very large amplitudes [81].

In laminar flow, the mean velocity profile was obtained as the solution of the Falkner-Skan equations. In turbulent flow, a three-layer model with the inner law in Spalding's formulation [82] and a law of the wake in Coles' formulation [83] was used. Both the laminar and the turbulent velocity profile are strictly valid for incompressible flow only, but were used regardless of the freestream Mach number. The use of incompressible velocity profiles in compressible flow was mandated by the unavailability of explicit formulae or simple codes which could be used to calculate the velocity profiles for arbitrary Mach numbers and Reynolds numbers. In laminar flow, considerable thickening of the boundary layer occurs for Mach numbers larger than unity (at constant Reynolds number), resulting in a reduction of the velocity gradients[84]. In turbulent flow, there is the additional complication that turbulent viscosity profiles corresponding to the velocity profiles are also needed. The mean temperature and density profiles were obtained from the mean velocity profiles with the assumption of an unity Prandtl number. However, the Prandtl numbers $Pr \equiv Pr_t = 0.72$ were used for the unsteady flow field.

The laminar viscosity μ and the conductivity κ were fixed at their mean values; their variation under the influence of the unsteady flow field is a higher-order effect. For turbulent flow, a simple algebraic turbulence model and an intermittency factor defined by Klebanoff [85] were used to prescribe the turbulent viscosity distribution. In the inner region, the turbulent viscosity was given by the viscosity distribution corresponding to Spalding's turbulent velocity profile [82]. In the outer region, the turbulent viscosity had the constant value $\mu_t = 0.0168 \overline{\rho}_e \overline{U}_e \overline{\delta}^*$. Since the model problem for the numerical evaluation of modeling errors is one-dimensional, there is no other choice than using an algebraic model. One-equation models or two-equation models of turbulence would require two dimensions to allow for streamwise transport equations. Investigators do not agree whether a simple algebraic model can adequately represent the turbulence structure in unsteady flow. While [86] reports fair agreement between experimentally and numerically determined velocity profiles and finds an algebraic model superior to an one-equation model, [87, 88] discount it as inadequate, in particular at high frequencies and for large unsteady amplitudes. The mean turbulent viscosity acts on the mean flow and the unsteady perturbations, i.e. the turbulent viscosity distribution is assumed constant at its mean value[6].

4.3.2 Code Verification in Laminar Flow

For a laminar, incompressible flow over a flat plate at zero pressure gradient, where the mean boundary layer thickness is

$$\overline{\delta}(x) \approx \frac{5s}{\sqrt{Re_s}}, \tag{4.82}$$

the ratio $(\overline{\delta}/\delta_f)$ is a function of the reduced frequency only.

$$\frac{\overline{\delta}}{\delta_f} \approx 5\sqrt{k_e} \tag{4.83}$$

The dependence on the Reynolds number drops out.

[6] Turbulent dissipation of kinetic energy first raises the turbulent kinetic energy $KE = \overline{(u'^2 + v'^2)}$, which in turn increases the turbulent viscosity μ_t. Only then is it turned into heat and causes an entropy rise. This effect is not captured in the model.

The laminar portion of the code was verified by comparison to Lighthill's analytical work [89] on oscillatory boundary layers in an incompressible mean flow. Figure 4.9 illustrates a case with a reduced frequency k_e=0.8, or equivalently a ratio $(\overline{\delta}/\delta_f)$=4.47; the agreement is seen to be excellent. In the limit $M_e \to 0$, the high-reduced-frequency limit and the near-wall approximation are exact, regardless of the ratio $(\overline{\delta}/\delta_f)$.

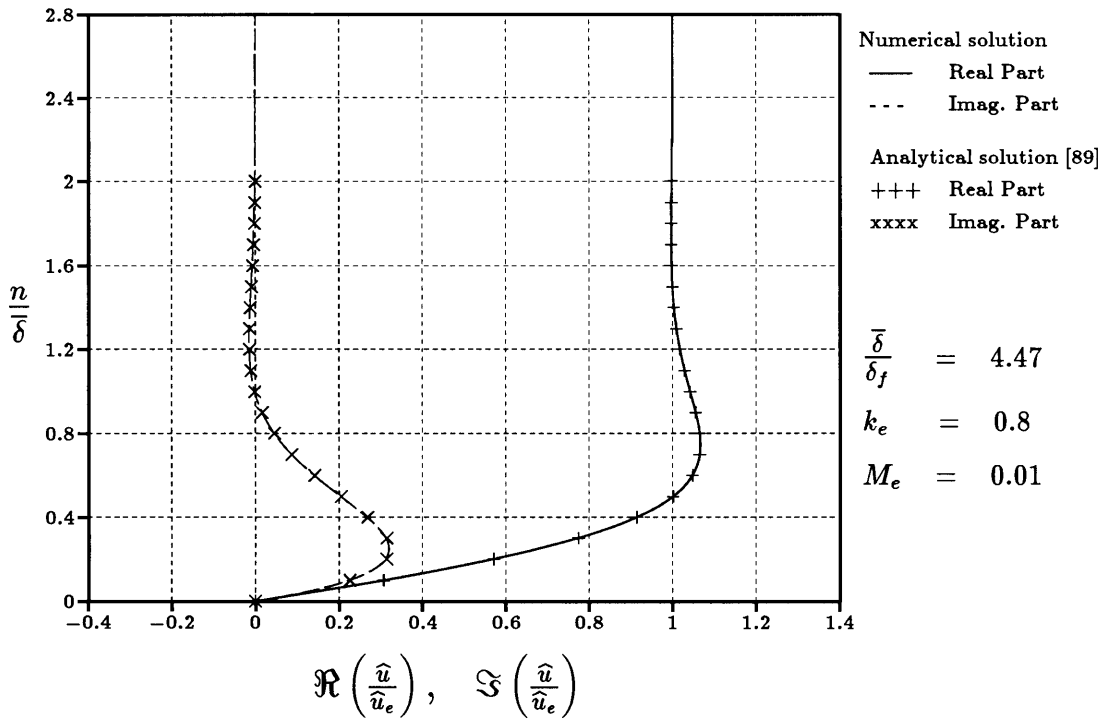

Figure 4.9: Comparison to Lighthill's analytic solution in laminar flow

In the high-frequency limit, equation (4.44) is the exact solution to (4.17) for finite (n/δ_f) regardless of the freestream Mach number. Figure 4.10 shows a comparison between the 'exact', numerical solution and the analytical solution for a Mach number of $M_e = 0.3$ and reduced frequencies of $k_e = 1, 4, 16, 64$. The velocities have been normalized by

$$|\widehat{u}_e| = \frac{k_s}{k_e}\frac{|\widehat{p}|}{\overline{\rho}_w}, \tag{4.84}$$

that is, by the magnitude of the unsteady velocity at the edge of the unsteady boundary layer in the high-frequency limit (4.44). The distance from the wall, n, has been normalized by the unsteady boundary layer thickness δ_f. On this normal scale, all solutions in

the high-frequency limit collapse one the solid lines. It is seen that the unsteady velocity distribution approaches the on predicted by the high-frequency limit for high reduced frequencies and finite values of (n/δ_f), regardless of the freestream Mach number. For high reduced frequencies, the differences are located at large values of (n/δ_f), where the 'exact' solution veers off to meet the boundary conditions in the freestream. The differences are almost imperceptible for the imaginary part of the solutions.

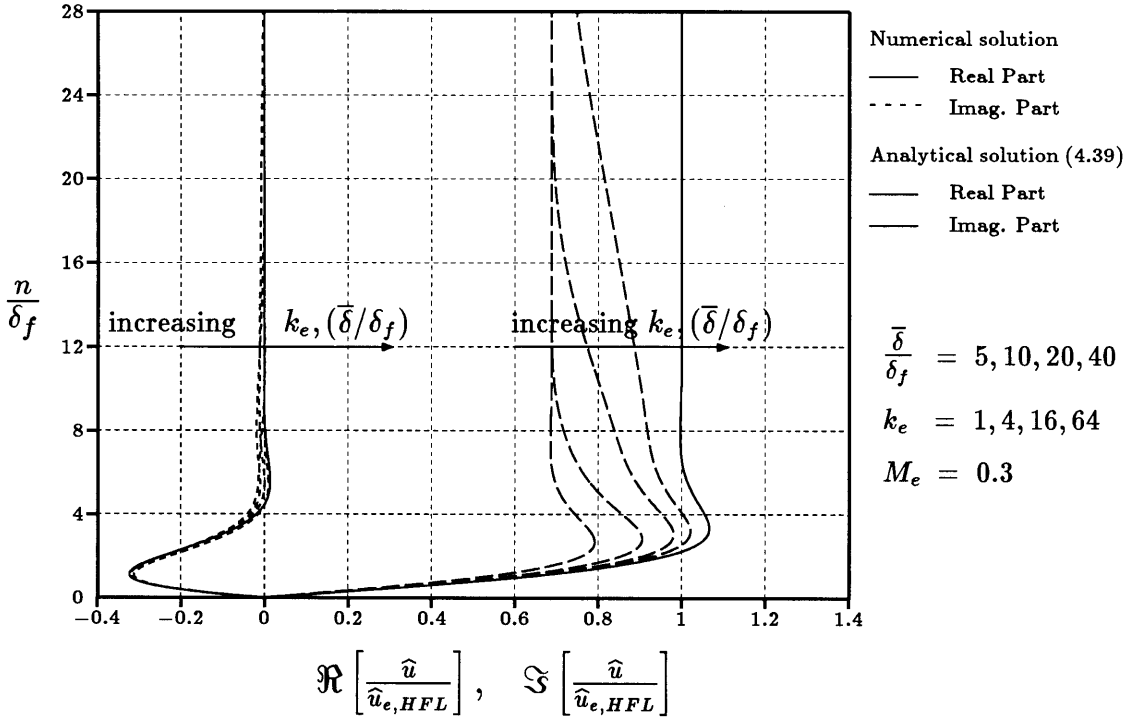

Figure 4.10: Comparison between 'exact' numerical solution and high-frequency limit

4.3.3 Errors in the Integrated Dissipation for Laminar Flow

The result of the numerical evaluation of modeling errors in laminar flow is summarized in figure 4.11, which quantifies the errors introduced by the near-wall approximation in the high-reduced-frequency limit.

It shows the ratio of the integrated dissipation $\overline{\widetilde{\Phi}}_{2i}$ calculated in the high-frequency limit (HFL) to the value calculated with the full linearized equations (4.70) to (4.75), for a pressure wave propagating parallel to the wall ($\theta = \pm 90^o$). In the limit $M_e \to 0$,

or $k_e, (\overline{\delta}/\delta_f) \to \infty$, the HFL model yields the correct dissipation. The lower the reduced frequency for a non-zero freestream Mach number, the greater is the deviation of the integrated dissipation calculated in the high-frequency limit. This is a consequence of the unsteady boundary layer spreading away from the wall into the steady boundary layer with a non-zero streamwise velocity where convective terms in equation (4.71) become significant. For the same reason, equation (4.39) does not yield the proper asymptotic value of the unsteady velocity in the freestream, as was shown in figure 4.5. With the velocity magnitude in the unsteady boundary layer off, the unsteady viscous dissipation must behave accordingly. Depending on the orientation of the pressure wave vector, the high-frequency limit yields an integrated dissipation greater than the value of the full linearized model (upstream propagating waves) or less (downstream propagating waves).

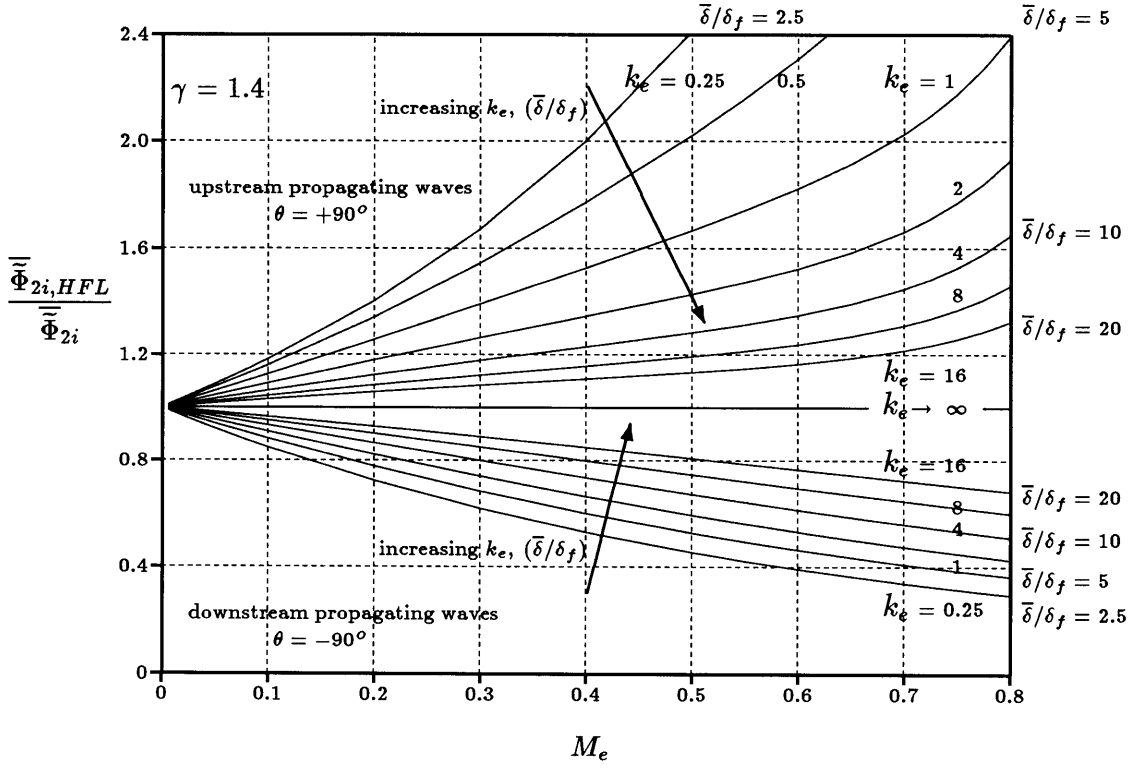

Figure 4.11: High-frequency-limit model and 'exact' laminar model dissipation

A different angle θ between the direction of wave propagation and the surface normal increases the wavelength and the decreases the pressure gradient driving the unsteady boundary layer. A non-zero mean pressure gradient influences the result primarily through a change in the mean shear and an associated change in the ratio $(\overline{\delta}/\delta_f)$.

4.3.4 Code Verification in Turbulent Flow

In turbulent flow over a flat plate at zero pressure gradient, the boundary layer thickness is given by

$$\overline{\delta} \approx \frac{0.37s}{Re_s^{1/5}}. \tag{4.85}$$

The ratio $(\overline{\delta}/\delta_f)$ now depends on the Reynolds number and the reduced frequency.

$$\frac{\overline{\delta}}{\delta_f} \approx 0.37\sqrt{k_e}\, Re^{3/10} \tag{4.86}$$

The mean flow, however, reaches a major fraction of the freestream velocity in the laminar sublayer already. Therefore, it is more instructive to consider the ratio $(\overline{\delta}_l/\delta_f)$, where $\overline{\delta}_l$ is a measure of the laminar sublayer thickness. In turbulent flow, the laminar sublayer extends no further than

$$\overline{\delta}_l \approx 30\, l_t, \tag{4.87}$$

where l_t is the characteristic length scale of turbulence defined as

$$l_t = \frac{\nu_w}{u_\tau}. \tag{4.88}$$

The wall friction velocity u_τ is defined by

$$u_\tau = \sqrt{\frac{\tau_w}{\rho_w}}. \tag{4.89}$$

The turbulent velocity fluctuations are characterized by u_τ and the eddy size by l_t. Through its dependence on the wall shear, the above definition of the laminar sublayer thickness in turbulent flow is valid in flows with pressure gradients, and is independent of the Reynolds number as well. In experiments with flat plate boundary layers in incompressible channel flows, Binder and Kueny [79] found that the unsteady laminar wall shear calculated in the near-wall approximation of the high-frequency limit, is a good approximation for $(\overline{\delta}_l/\delta_f) > 4.2$. In the parameter range $4.2 > (\overline{\delta}_l/\delta_f) > 2.8$, they observed only slight deviations in the phase. In the range $(\overline{\delta}_l/\delta_f) < 2.8$, the unsteady wall shear increased above the laminar value. Appendix I compares the turbulent length scale and time scale to the length scale of the unsteady boundary layer and the forcing time scale in incompressible flow.

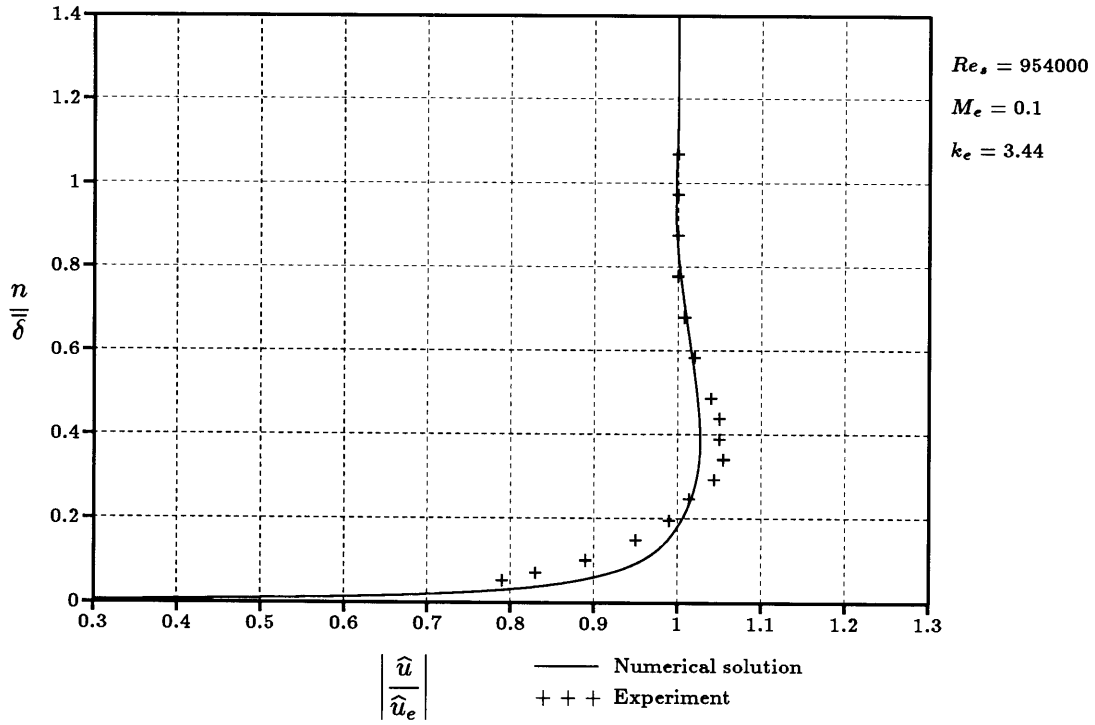

Figure 4.12: Comparison to Cousteix's experiment — unsteady streamwise velocity

Verification of the turbulent portion of the code was complicated by the fact that no experiments were found that used a propagating wave type disturbance in the freestream. In a first test, it was verified that the code reproduced the laminar solution for reduced frequencies high enough to confine the unsteady boundary layer to the laminar sublayer of the mean flow; this test is not presented here. Cousteix, Desopper, and Houdeville [90] conducted experiments in which the freestream velocity in a subsonic wind tunnel varied sinusoidally in response to a rotating vane at the exit. For the wind tunnel's resonance frequency, they examined the unsteady boundary layer at four axial locations. While the mean flow velocity was practically constant, the freestream velocity perturbation was a strong function of the axial position; the phase change along the axial direction was less than what would be seen for a propagating pressure wave. However, as long as the reduced frequencies of experiment and numerical solution match, the results can be compared. In the linear regime, the magnitude of the driving unsteady pressure gradient does not influence the velocity distribution. To allow a comparison, the experimental and the numerical unsteady velocity distributions were normalized by their respective freestream values.

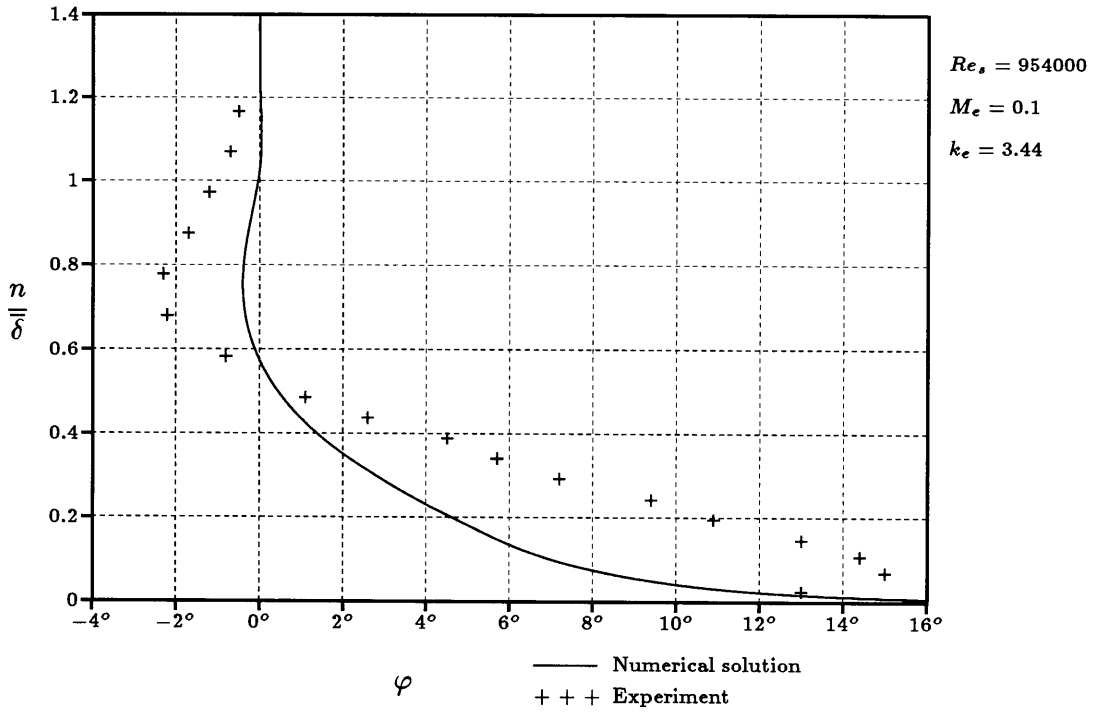

Figure 4.13: Comparison to Cousteix's experiment — unsteady velocity phase

Figures 4.12 and 4.13 show a comparison to the experiments of Cousteix [90]. The agreement in the unsteady streamwise velocity is acceptable in the view of the modeling shortcomings. The maximum velocity overshoot occurs roughly at the same distance from the wall; its magnitude is only 3% instead of the experimentally observed 6%. In addition, the unsteady velocity gradient outside the laminar sublayer is steeper in the numerical solution.[7]

The phase angles of the unsteady velocity are in qualitative agreement. The maximum overshoot (towards negative phase angles) is at the correct location but too small. Closer to the wall, the computed values are offset towards lower $(n/\overline{\delta})$ while the maximum phase angle is approximately correct.

Similar observations have been made in other comparisons to between numerical and experimental results [80, 86]. In particular, [86] contains a numerical and experimental study which also uses an algebraic turbulence model.

[7] This may be due to an increase in the turbulent viscosity from the turbulent kinetic energy production (mean-flow kinetic energy dissipation).

4.3.5 Errors in the Integrated Dissipation for Turbulent Flow

Figure 4.11 is valid only in a laminar mean flow. The flows encountered in practice, however, will almost always be (transitional or) turbulent, and the unsteady boundary layer can extend well beyond the laminar sublayer. In figures 4.14 and 4.15 error due to the assumption of a laminar mean flow in the high-frequency-limit model appears superimposed upon the error due to a finite reduced frequency. These figures show

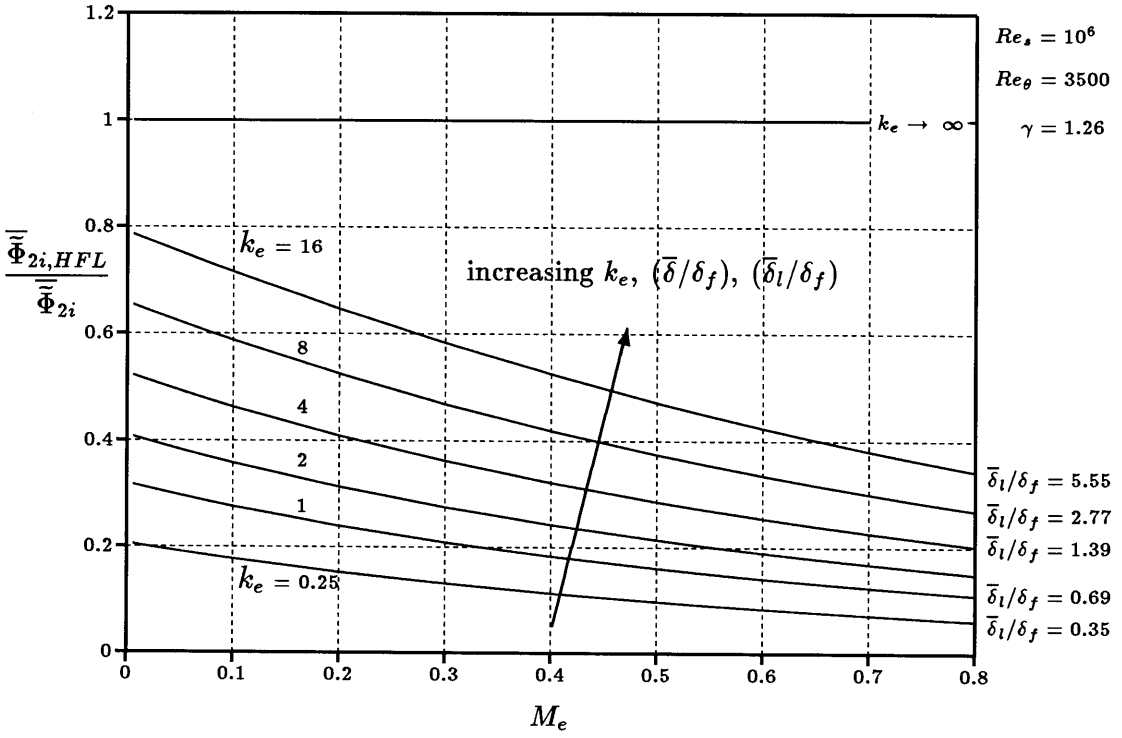

Figure 4.14: High-frequency-limit model and 'exact' turbulent model dissipation — downstream propagating pressure waves

the ratio of the integrated dissipation $\overline{\tilde{\Phi}}_{2i}$ calculated in the high-frequency limit (HFL) to the 'exact' turbulent dissipation calculated numerically. Figure 4.14 is valid for a downstream propagating wave, figure 4.15 for an upstream propagating wave. As opposed to the case with a laminar mean flow, the high-frequency-limit solution is not exact in the limit $M_e \to 0$, any more. The turbulent nature of the mean flow introduces additional errors into the high-frequency-limit model, which is an inherently laminar model. For high reduced frequencies, the turbulent dissipation again approaches the

value predicted by the high-frequency-limit model, although this is not evident within the range of reduced frequencies displayed. Except for upstream propagating waves at high Mach numbers, its tendency is to underestimate the integrated dissipation.

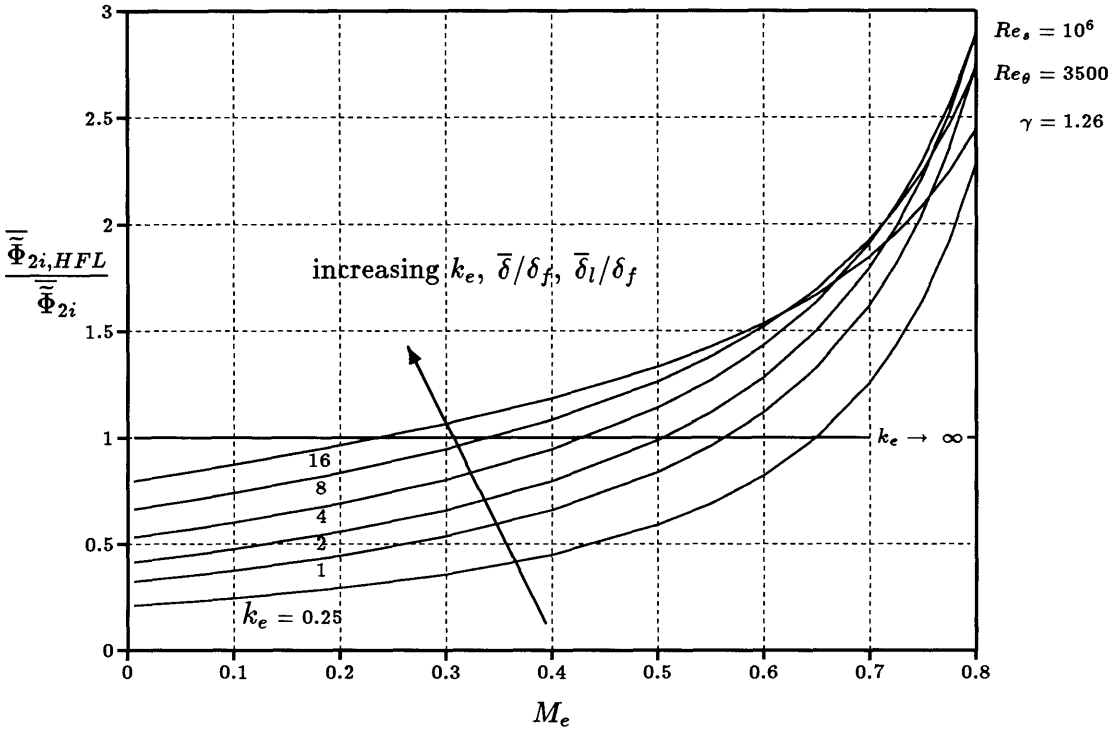

Figure 4.15: High-frequency-limit model and 'exact' turbulent model dissipation — upstream propagating pressure waves

Figure 4.16 illustrates this with plots of the unsteady streamwise velocity at a Mach number of M_e=0.8 for reduced frequencies $k_e = 0.25, 1, 4, 16$, and 64. It can be expected that the 'exact' turbulent solution in the near-wall region starts to approach the HFL solution if the ratio (δ_l/δ_f) exceeds $O(1)$. At a Reynolds number of Re=10^6, the aforementioned reduced frequencies correspond to $(\overline{\delta}_l/\delta_f) \approx 0.35, 0.69, 1.39, 2.77$, and 5.55. For a ratio $(\overline{\delta}_l/\delta_f) \approx 3$, the shape of the unsteady velocity distribution in figure 4.16 changes from the fuller turbulent profile to the laminar profile of the HFL solution; it takes an even higher ratio $(\overline{\delta}_l/\delta_f)$ to have quantitative agreement in the maximum of the unsteady streamwise velocity. Figure 4.17 is identical to figure 4.16 except that the scales have been changed to allow details at the wall to be examined more closely.

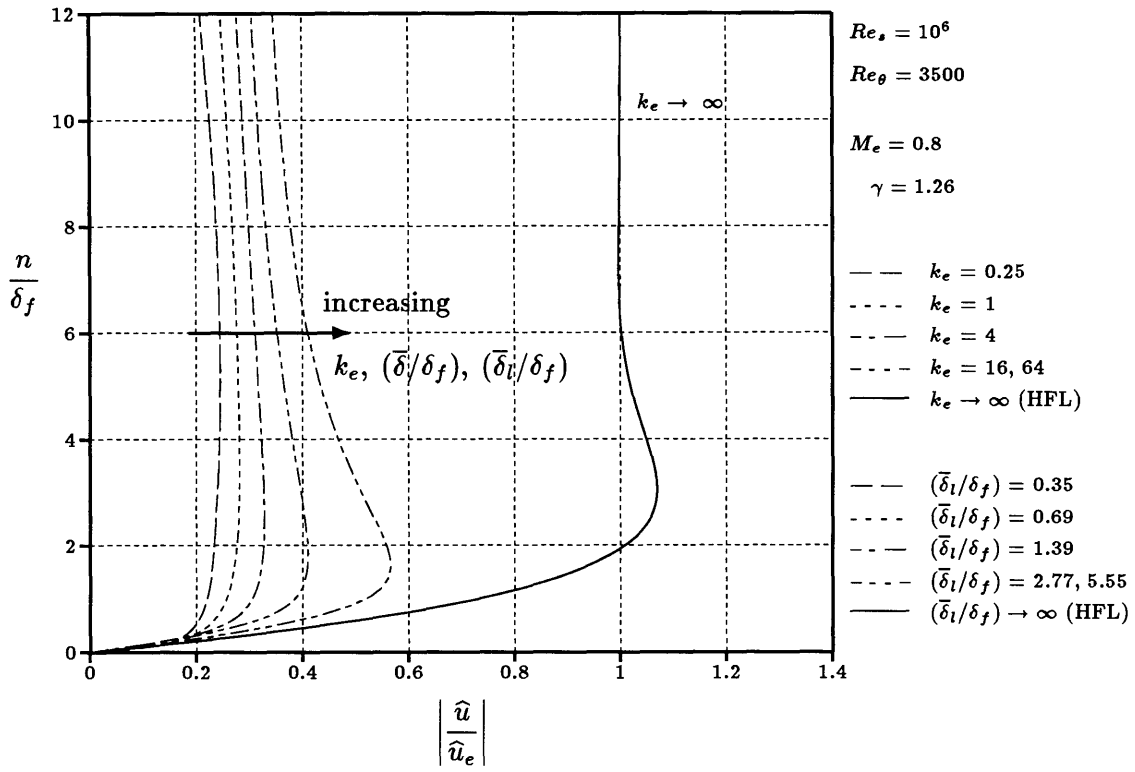

Figure 4.16: Unsteady streamwise velocity distribution in a turbulent mean flow — upstream propagating pressure waves

Returning to the dissipation in figures 4.14 and 4.15, one notices that the ratio $(\overline{\overline{\Phi}}_{2i,HFL}/\overline{\overline{\Phi}}_{2i})$ for a downstream propagating wave in turbulent flow behaves similar to the corresponding ratio in laminar flow. With higher reduced frequency and lower Mach number, the high-frequency limit is more accurate. The behavior of the ratio $(\overline{\overline{\Phi}}_{2i,HFL}/\overline{\overline{\Phi}}_{2i})$ for an upstream propagating wave, however, differs from the behavior of the corresponding ratio in laminar flow. In the limit $M_e \to 0$, the ratio is less than one and matches the value for a downstream propagating wave; the rate of unsteady dissipation in a turbulent mean flow is higher than the rate in a laminar mean flow. The (laminar) high-frequency model underpredicts the velocity gradients and the viscosity in a turbulent mean flow and thus arrives at too low an integrated dissipation for finite reduced frequencies. As the Mach number increases, this ratio rises above one because the high-frequency limit overpredicts the magnitude of the unsteady velocity in the freestream; it is the relative magnitude of these two effects that governs the behavior of the ratio $(\overline{\overline{\Phi}}_{2i,HFL}/\overline{\overline{\Phi}}_{2i})$ in figure 4.15.

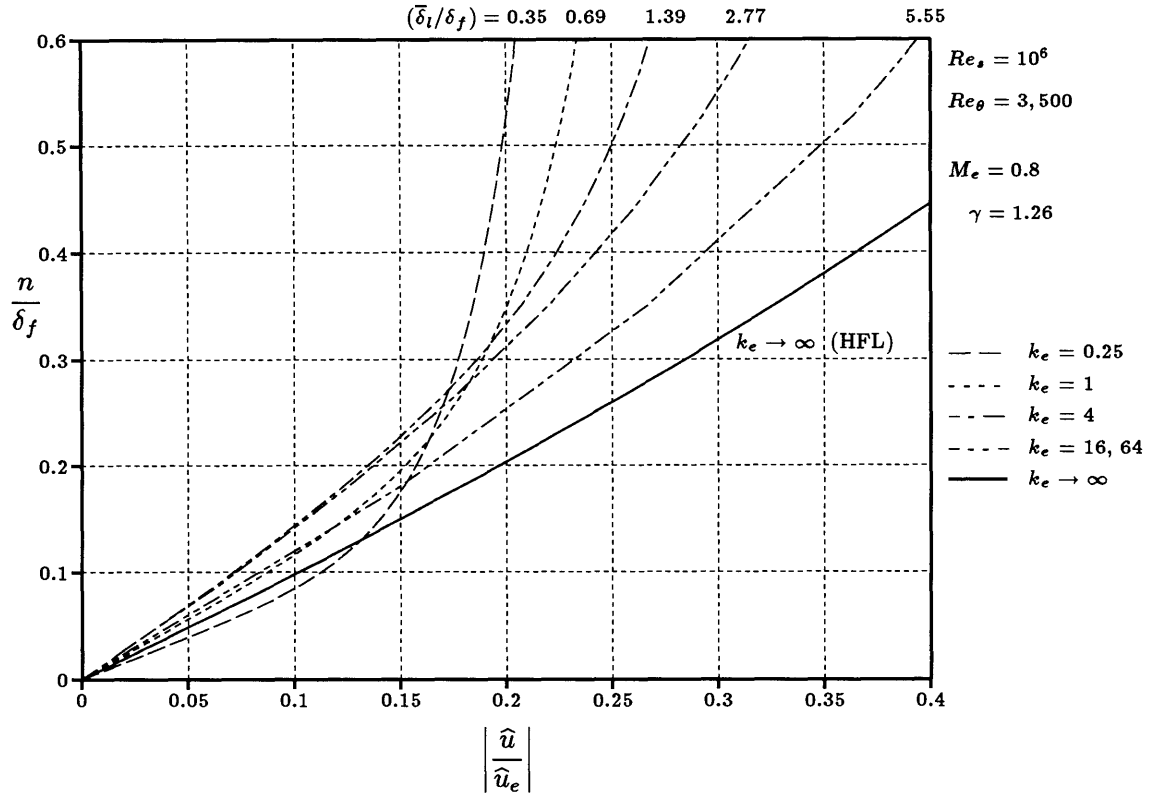

Figure 4.17: Unsteady streamwise velocity distribution near the wall in a turbulent mean flow — upstream propagating pressure waves

It is puzzling, at first, that there is a (Mach-number dependent) range of reduced frequencies in figure 4.15 for which the ratio $(\overline{\overline{\Phi}}_{2i,HFL}/\overline{\overline{\Phi}}_{2i})$ moves away from unity when the reduced frequency is increased and moves back towards unity beyond that range. This behavior can be explained with the help of figures 4.16 and 4.17. The major part of the unsteady viscous dissipation occurs near the wall and is locally proportional to the square of the velocity gradient and the viscosity. As a first approximation, the integrated dissipation is set by the magnitude of the dissipation and the normal extent over which it acts. On the normal scale (n/δ_f), the unsteady velocity gradient in figure 4.17 is steepest for low reduced frequencies, i.e for a laminar sublayer thickness much less than the unsteady boundary layer thickness. It is steeper than the unsteady velocity gradient in a laminar mean flow, the same way the steady velocity gradient is steeper in a turbulent mean flow than in a laminar mean flow. As the reduced frequency is increased, the ratio $(\overline{\delta}_l/\delta_f)$ increases and the velocity gradient eventually equals the one in the high-frequency limit and the turbulent viscosity approaches the laminar

viscosity. The high-frequency-limit solution is the same for all reduced frequencies on the scales chosen for figure 4.17. This effect depends mainly on the ratio $(\overline{\delta}_l/\overline{\delta})$ and moves $(\overline{\overline{\Phi}}_{2i,HFL}/\overline{\overline{\Phi}}_{2i})$ towards higher values as the reduced frequency is increased; the turbulent dissipation increases less rapidly than the dissipation predicted by the high-reduced-frequency model. The change of behavior for higher reduced frequencies comes about because of a second effect, seen in figure 4.16. When the reduced frequency is sufficiently high, the maximum of the unsteady turbulent velocity approaches the value predicted in the high-frequency limit before it veers off to match the boundary condition in the freestream. Thus, the extent over which the gradient acts becomes larger and $(\overline{\overline{\Phi}}_{2i,HFL}/\overline{\overline{\Phi}}_{2i})$ moves towards unity. This effect depends primarily on the Mach number because it sets the freestream velocity disturbance via equation (4.46) and tends to move the ratio of losses towards unity. For $M_e \rightarrow 0$, this effect vanishes. Regardless of the Mach number, the ratio $(\overline{\overline{\Phi}}_{2i,HFL}/\overline{\overline{\Phi}}_{2i})$ always approaches unity for sufficiently high reduced frequencies.

4.4 Unsteady Loss in the ACE Turbine Stage

The ACE turbine stage is a highly loaded, transonic high-pressure turbine stage, which has been tested at MIT [50]. A 2D-version of the rotor profile was investigated at Oxford University [52, 54]. Its design is representative of modern high-pressure turbine stages. A detailed computational account of the inviscid stator/rotor interaction is presented in [6]; subsection 3.2.4 summarized the shock wave/blade row interaction. The parameters in this simulation were similar to the parameters of subsection 3.2.4 except that the code, UNSFLO, was run in the viscous mode [7], the rotor speed increased, and the back pressure lowered slightly. The computational grid as well as the pressure contours for the steady and the unsteady viscous simulation were shown in section 2.7.

Table 4.1 lists the input parameters. Lengths have been nondimensionalized by the stator axial chord, the rotor speed by the inlet stagnation speed of sound, and the outlet static pressure by the inlet stagnation pressure. The Reynolds number $Re_{i,t}$ is formed with inlet stagnation quantities (upstream of the stator row) and the stator axial chord.

Rotor Axial Chord $c_{a,R}$		0.762
Stator Pitch P_S		1.344
Rotor Pitch P_R		0.778
Axial Gap		0.318
Inlet Flow Angle		0^o
Rotor Speed V_R		0.737
Ratio of Specific Heats γ		1.26
Outlet Static Pressure p_o		0.234
Stator	suction surface $x < 0.60$	laminar
	suction surface $x > 0.65$	turbulent
	pressure surface $x < 0.4$	laminar
	pressure surface $x > 0.5$	turbulent
Rotor Blades		turbulent
Reynolds Number $Re_{i,t} = (\rho_{i,t} a_{i,t} c_{a,S} / \mu_{i,t})$		2.256×10^6

Table 4.1: Input parameters for the ACE turbine stage simulation

The increased rotor speed in conjunction with the lower backpressure led to slightly stronger trailing edge shock waves and reduced the mean rotor inflow angle from the design inflow angle of 58^o to 48^o, matching the experiments of Johnson et al. [54]. The linear velocity analysis for this stage can be regarded as a viscous complement to the investigation of Johnson et al., who studied the surface heat transfer fluctuations in response to a passing shock wave.

In experiments by Ashworth et al. [52], the rotor boundary layer was found to be laminar over most of the suction surface for low levels of freestream turbulence and in the absence of wakes and shock waves. The pressure surface boundary layer was transitional. Bar passing experiments, to simulate stator wakes and shock waves, showed that widely spaced wakes and shock waves temporarily trip the boundary layer, which will relax back to a laminar state after the disturbance has passed. For a bar spacing resembling engine conditions, the boundary layer is transitional or turbulent. In the simulation, the flow was prescribed to be turbulent from the rotor leading edge on. The turbulence

model was an algebraic model in the formulation of Cebeci and Smith [91]; all blades were modeled as adiabatic blades.

4.4.1 Application of the Unsteady Viscous Loss Model

Predicted Loss

The loss model based on the near-wall approximation in the high-frequency limit, described in section 4.1, was applied to the ACE turbine stage. The input required for the model are the time-harmonics of the pressure gradient along the blade surfaces. These may be the result of an inviscid or a viscous simulation, although the dominating effect of the rotor passing through the oblique shock waves of the stator is captured inviscidly[8]

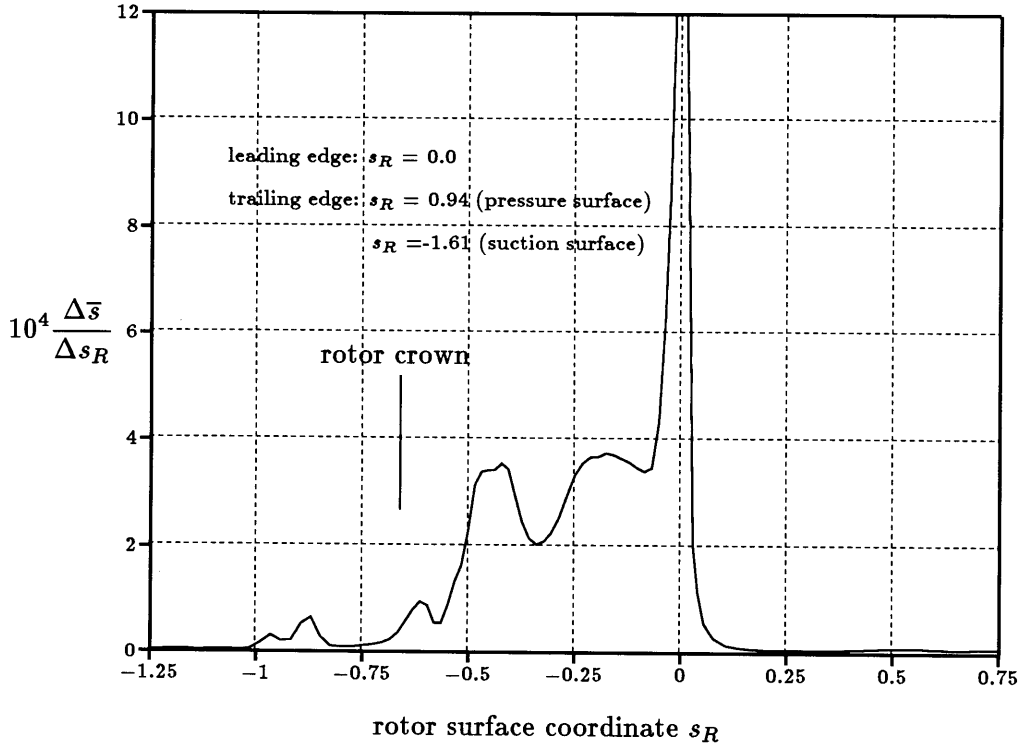

Figure 4.18: Entropy rise per unit surface length on the ACE rotor

[8] In both cases, numerical smoothing will affect the unsteady pressure amplitudes. See subsection 4.4.3 for details.

Figure 4.18 shows the distribution of the time-mean, mass-average entropy rise $\Delta\overline{s}$, defined in equation (4.54), per unit surface length Δs_R along a rotor blade. A value of s_R=0 corresponds to the rotor leading edge; positive and negative values correspond to pressure and suction sides, respectively[9] The dissipation is concentrated on the suction surface between the rotor leading edge and the crown, where the pressure gradient fluctuates in response to shock wave passing/reflection. Note that figure 2.14 shows a pronounced rise of the (time-mean, mass-average) entropy in the rotor passage between the leading edge and the crown. The integrated entropy rise for a rotor blade is $\Delta\overline{s} = 2.8 \times 10^{-4}$, which is equivalent to a total pressure loss $\Delta\overline{p}_t = -1.3 \times 10^{-3}$. The above numbers translate into an isentropic efficiency drop $\Delta\eta_{s,E}/\eta_{s,E,D} = -0.09\%$. Of the total, 70% is at the blade passing frequency and 16% in the second harmonic. Table 4.2 shows the contribution of individual harmonics to the entropy rise.

total entropy rise $\sum_m \Delta\overline{s}_m$	2.8×10^{-4}	100%
blade passing frequency	1.96×10^{-4}	70.1%
2^{nd} harmonic	0.45×10^{-4}	16.1%
3^{rd} harmonic	0.10×10^{-4}	3.6%
4^{rd} harmonic	0.11×10^{-4}	4.0%
5^{th} harmonic	0.07×10^{-4}	2.5%
all higher harmonics	0.10×10^{-4}	3.7%

Table 4.2: Modal contributions to the Unsteady Viscous Loss of the ACE rotor

The Unsteady Viscous Loss on a stator was more than a factor of ten smaller than the loss on a rotor; the stator passage is choked and the unsteady interaction between shock waves and blade rows is much stronger in the rotor blade row.

Loss Model Errors

Figures 4.14 and 4.15 identified the parameters governing the error in the integrated dissipation predicted by the high-frequency-limit model in turbulent flow. They are the

[9] see figure 2.12

ratio of laminar sublayer thickness to unsteady boundary layer thickness, $(\overline{\delta}_l/\delta_f)$, and the freestream Mach number M_e. These figures illustrated computations for a flow at zero mean pressure gradient. Nevertheless, they can be used to estimate the error for the ACE turbine stage, which has a strong favorable mean pressure gradient in the primary region of Unsteady Viscous Loss. A mean pressure gradient enters through the wall shear velocity u_τ in the definition of the laminar sublayer thickness (4.88). This definition is valid for arbitrary pressure gradients, Reynolds numbers, and Mach numbers. Calculating the laminar sublayer thickness in the primary region of Unsteady Viscous Loss from the wall shear of the steady simulation gives a thickness ratio of $(\overline{\delta}_l/\delta_f)\approx 1.2$ for the unsteady boundary layer at the blade passing frequency. The freestream Mach number in the primary loss region is $M_e\approx 0.65$ (in the rotor frame of reference). Therefore, figure 4.14 suggests that the Unsteady Viscous Loss predicted for the ACE turbine stage could be up to five times the nominal value of $\Delta\overline{s}=2.8\times10^{-4}$. Figure 4.15 implies that the loss model, when applied to the ACE turbine stage, overpredicts the actual Unsteady Viscous Loss by no more than a factor of 1.5.

4.4.2 Efficiencies in the Numerical Simulation

The unsteady loss can also be inferred by comparing a steady and an unsteady viscous simulation for the same profile. In a steady simulation, the stator outflow is averaged at the interface to provide a spatially uniform and steady rotor inflow condition. The efficiencies can be calculated from the time-mean, mass-average total pressures and temperatures at the inlet boundary, the interface, and the outlet boundary. With the total pressures and temperatures known, the isentropic efficiency may be calculated from equation (2.49). Table 4.3 lists the isentropic efficiencies. Streamflux-average efficiencies include the mixing loss from the dissipation of unsteady waves beyond the rotor outlet boundary. The higher stage efficiency in the unsteady case is a direct consequence of the mixing loss at the steady interface, as was discussed in section 2.7.

Detailed measurements of total temperature and total pressure with the spatial and temporal resolution required to deduce the steady or the unsteady efficiency for this

stage are not available. Moreover, the experimental error bands would be of the same order of magnitude as the numerical difference in efficiency between the steady and the unsteady simulation. An indication that the calculated stage efficiency is realistic can be obtained from a combined experimental and numerical study of a single stage of comparable Reynolds number and total pressure ratio reported in [53]. While the efficiencies are 2% to 3% less in [53], they include endwall loss, tip clearance loss, and secondary flow loss, which are shown to add up to roughly one half of the total loss.

$\eta_{s,E}$	steady	unsteady
stage	93.58 %	94.06 %
stage *(streamflux-averaged)*	93.04 %	93.21 %
rotor	97.73 %	96.48 %
rotor *(streamflux-averaged)*	97.13 %	95.59 %

Table 4.3: Isentropic efficiencies for the steady and the unsteady ACE simulation

The Unsteady Viscous Loss on the rotor blade surface is small compared to the total loss in an unsteady viscous simulation. Nominally, i.e. at an isentropic efficiency drop of $(\Delta\eta_{s,E}/\eta_{s,E})$=−0.09%, it accounts for only 1.43% of the total loss in the stage[10](or the deviation of the stage efficiency from unity). Including the error bounds, it can account for 1% to 7.1% of the total loss. The unsteady rotor efficiency is 1.25% less than the steady rotor efficiency. The predicted Unsteady Viscous Loss could account for about one third of this drop in the efficiency within the error bounds stated.

For an experiment that compared identical profiles in steady and in unsteady flow, that is, in a linear cascade and in a stage, Hodson [9] reported an increase of 50% in the rotor profile loss for the unsteady case. This was found to be due to the nature of the boundary layer changing in sympathy with the passing of stator wakes. In the simulation of the ACE turbine stage, the loss of the rotor blade row is 55% higher in unsteady flow than in steady flow. Barring turbulence modeling, mechanisms that can increase the loss in the unsteady simulation include unsteady shock waves [18], shock

[10]see figure 2.14

wave/boundary layer interaction, unsteady boundary layers, and numerical smoothing in the freestream. In the steady as well as in the unsteady simulation, the boundary layer was prescribed turbulent from the rotor leading edge on. Thus, there are no changes in the transition point location or in the boundary layer character. The transition point on the stator was also fixed. No separation, be it shock-induced or not, was found in either simulation. While the magnitude of the loss increase in unsteady flow is in line with [9], the mechanism is different. Neither Unsteady Viscous Loss nor a change in the nature of the boundary layer character can account for the loss increase in unsteady flow.

4.4.3 The Role of Numerical Smoothing

Questions remain about the exact magnitude of the Unsteady Viscous Loss. However, they cannot explain the loss increase in unsteady flow, even if the errors of the loss model are accounted for. The mechanisms behind the loss increase in the unsteady simulation remain unclear, but there are indications that numerical smoothing in the freestream plays an important role. Numerical smoothing, explicitly added to or implicit in a code, is necessary to stabilize numerical simulations of the (inviscid) Euler equations. In UNSFLO, the flow is governed by the Euler equations on the H-Grid through the blade passages[11] and by the Thin-Shear-Layer approximation of the Navier-Stokes equations in the O-Grid around the blade surfaces. The H-grid roughly coincides with the freestream, the core flow, while all blade boundary layers are contained within the O-grid. In the O-grid, numerical smoothing is not necessary to stabilize the code; in fact, it would corrupt the solution in the boundary layer.

Should numerical smoothing be an important player in the loss increase, there are two implications. First, the simulation may not dissipate unsteady (pressure) waves primarily in unsteady boundary layers, as happens in physical flows[12] but in the freestream. Second, the unsteady pressure gradients acting on the blade surfaces, which are the input to the loss model, may have been diminished prematurely, reducing the predicted level of Unsteady Viscous Loss.

[11] Strictly speaking, it is not an H-grid because of the triangular cells at the inflow and outflow boundaries. See figure 2.15.

[12] see introduction to chapter 4

The indications suggesting that numerical smoothing in the freestream plays an important role in unsteady simulations are as follows:

First, it is difficult to detect more than three shock wave reflections in the visualization of an unsteady simulation. To see whether such a small number is physically realistic, the rate of amplitude attenuation due to dissipation in unsteady boundary layers and due to numerical smoothing in the freestream will be estimated and compared.

Second, in figure 2.14, the entropy rise between rotor crown and trailing edge is steeper in the unsteady simulation. Neither the steady nor the unsteady simulation showed any separation and the predicted Unsteady Viscous Loss is small in this region.

Third, the difference between the mass-average and the streamflux-average isentropic rotor efficiency is about 0.6% in the steady case and 0.9% in the unsteady case. The streamflux-average efficiency is less because it includes mixing losses downstream of the rotor. The larger difference in the unsteady case is a consequence of the presence of unsteadiness in the form of pressure waves, vorticity waves, and entropy waves at the rotor exit. According to the inviscid simulations of subsection 3.2.4, the dissipation of vorticity shed at the rotor trailing edge (Unsteady Circulation Loss) alone should have accounted for a mixing loss of 0.3% in the isentropic efficiency.

The action of numerical smoothing in the freestream (the H-Grid) could explain these observations. The following analytical and numerical considerations confirm that numerical smoothing is the main mechanism leading to increased loss in unsteady simulations.

Attenuation of Pressure Waves at Boundaries

At the introduction to this chapter, it was shown that the energy associated with unsteady waves is dissipated primarily in unsteady boundary layers. However, the rate at which the wave amplitudes are attenuated remains to be determined. Based on the results of section 4.1, the attenuation of a pressure wave in laminar flow can be estimated. Figure 4.19 illustrates the model problem graphically.

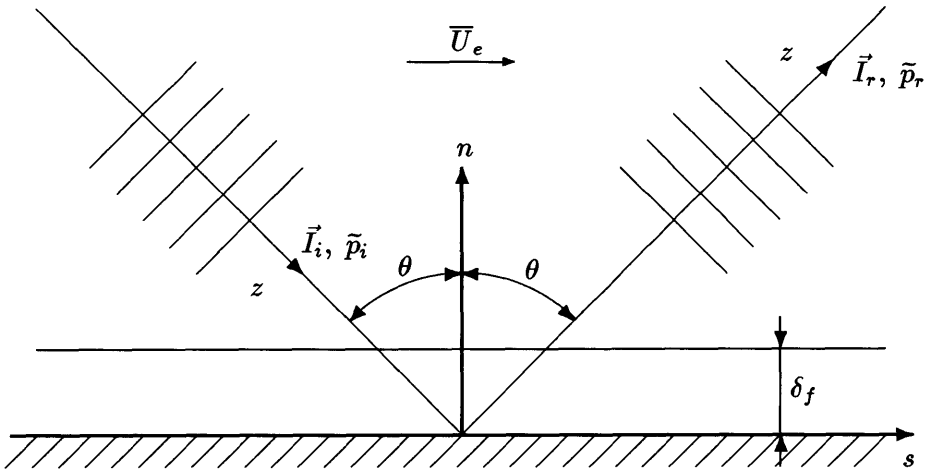

Figure 4.19: Attenuation of an acoustic wave in an unsteady boundary layer

An incoming pressure wave at an angle of incidence θ to the surface normal,

$$\tilde{p}_i \;=\; \hat{p}\,\exp\{i\;(k_s s - k_n n - t)\}\,, \tag{4.90}$$

causes a reflected wave

$$\tilde{p}_r \;=\; (1-\beta)\;\hat{p}\,\exp\{i\;(k_s s + k_n n - t)\;+\;i\,\varphi\}\,, \tag{4.91}$$

where the amplitude attenuation factor β and the phase angle φ depend on the complex impedance $\mathbf{R}$ of the unsteady boundary layer which dissipates part of the wave energy.

$$\mathbf{R} \;=\; \frac{\tilde{p}_r}{\tilde{p}_i} \;=\; (1-\beta)\;e^{+\,i\,\varphi} \tag{4.92}$$

Recalling that $\delta_f \ll \lambda_f$ by (4.33), one can make the simplifying assumptions

$$k_n \delta_f \;\ll\; 1 \tag{4.93}$$

$$\text{and} \quad \varphi \;\ll\; 1 \tag{4.94}$$

at the edge of the unsteady boundary layer.

The incident as well as the reflected wave induce an unsteady streamwise velocity distribution in the boundary layer. Due to inequalities (4.93) and (4.94), those are nearly in phase. For an incompressible mean flow, the unsteady velocity gradient in the boundary layer is approximately

$$\frac{\partial \tilde{u}}{\partial n} \approx (2-\beta)\,(1-i)\left(\frac{k_s}{k_e}\right)\sqrt{\frac{k_e Re}{2}}\,\exp\left\{-\frac{(1-i)}{\sqrt{2}}\frac{n}{\delta_f}\right\}\,\hat{p}\,\exp\{i\,(k_s s - t)\} \quad (4.95)$$

from equation (4.44). The rate of dissipation per unit surface area in response to the unsteady velocity gradient (4.95) is obtained from (4.53) as

$$\bar{\bar{\Phi}}_{2i} = \frac{(2-\beta)^2}{2k_e}\sqrt{\frac{1}{2k_e}\frac{1}{Re}}\left|\frac{\partial \hat{p}}{\partial s}\right|^2. \quad (4.96)$$

The average rate of acoustic energy incident per unit surface area is given by the acoustic intensity

$$\bar{\bar{I}}_i \cos\theta \approx \frac{1}{2}\,|\hat{p}_i \hat{v}_i| \approx \frac{1}{2}\,|\hat{p}_i|^2\,M_e\,\cos\theta, \quad (4.97)$$

while the average rate of acoustic energy reflected per unit surface area is

$$\bar{\bar{I}}_r \cos\theta \approx \frac{1}{2}\,(1-\beta)^2\,|\hat{p}_r \hat{v}_r| \approx \frac{1}{2}\,(1-\beta)^2\,|\hat{p}_r|^2\,M_e\,\cos\theta. \quad (4.98)$$

The above acoustic intensities, strictly valid only for $M_e = 0$, are used for simplicity. Since the objective is an order-of-magnitude argument, these simplification will not compromise the subsequent conclusions; other consistent simplifications will be made. Balancing incoming intensity, reflected intensity, and unsteady viscous dissipation, one obtains

$$\left[1-(1-\beta)^2\right]\,M_e \cos\theta = \left(\frac{k_s}{k_e}\right)^2\sqrt{\frac{1}{2}\frac{k_e}{Re}}\,(2-\beta)^2. \quad (4.99)$$

Since β is small by definition, the solution of interest is found as

$$\beta_1 = M_e\sqrt{2\,\frac{k_e}{Re}}\,\tan\theta\sin\theta. \quad (4.100)$$

The relation $(k_s/k_e)^2 \approx M_e^2$, obtained from equation (4.69) in the limit $M_e \to 0$, has been used in the above result. Alternatively, equation (4.100) can be expressed in the form

$$\beta_1 = \sqrt{2\left(\frac{M_e}{Re}\right)\left(\frac{2\pi}{\lambda_f}\right)}\,\tan\theta\sin\theta. \quad (4.101)$$

In appendix J, the same result is derived via the high-reduced-frequency limit of the linearized momentum equation; it also shows how the two approaches are related.

The longest nondimensional wavelength λ_f in a turbomachine typically is $O(1)$. Assuming Reynolds and Mach numbers typical of turbomachines, and $\tan\theta \sin\theta$ of $O(1)$, one expects to see $O(10^2)$ reflections before a wave amplitude is halved. In a (viscous or inviscid) simulation of the ACE turbine stage, however, no more than three reflections can be detected. The approximations made in the loss model and in the above order-of-magnitude argument can not account for a difference of two orders of magnitude in the number of reflections; that small a number of reflections is unphysical.

Numerical Smoothing in the Free Stream

The propagation of a pressure wave in the freestream beyond the boundary layers is modeled numerically by the convection-diffusion equation

$$\frac{\partial \widetilde{p}}{\partial t} + (1 \pm M_e \sin\theta)\frac{\partial \widetilde{p}}{\partial z} = \frac{1}{Re}\frac{\partial^2 \widetilde{p}}{\partial z^2} + \epsilon_2 \Delta \mathbf{S} \frac{\partial^2 \widetilde{p}}{\partial z^2} - \epsilon_4 \Delta^3 \frac{\partial^4 \widetilde{p}}{\partial z^4}, \tag{4.102}$$

where z is a coordinate along the direction of wave propagation; Δ denotes the mesh spacing. Here, the time t has been nondimensionalized by the axial chord and the speed of sound in the freestream. Numerical smoothing, necessary to stabilize numerical simulations of the Euler equations, has been added on the right-hand side. The time-rate of decay of the amplitude due to second-difference smoothing for shock wave capturing is

$$\beta_2 \sim \epsilon_2 \, \Delta \, k^2, \tag{4.103}$$

where ϵ_2 denotes the corresponding smoothing coefficient and k the wavenumber in the direction of propagation. The factor $\epsilon_2 \Delta$ plays the role of an inverse Reynolds number. In smooth-flow regions, second-difference smoothing is turned off by the pressure switch $\mathbf{S}$ ($0 \leq \mathbf{S} \leq 1$). There, the time-rate of decay due to the remaining fourth-difference smoothing is

$$\beta_4 \sim \epsilon_4 \, \Delta^3 \, k^4. \tag{4.104}$$

Assuming that a wave typically travels one axial chord between two successive reflections, the time in between two reflection is $t \approx 1$ for moderate Mach numbers. Thus, β_2 and β_4 also represent the amplitude attenuation factors due to numerical smoothing between reflections. Alternatively, they may be written as

$$\beta_2 \sim \epsilon_2 \Delta (2\pi/\lambda_f)^2 \quad \text{and} \quad \beta_4 \sim \epsilon_4 \Delta^3 (2\pi/\lambda_f)^4, \tag{4.105}$$

which shows the strong bias of fourth-difference smoothing towards short wavelengths. Typical values of the smoothing coefficients are $\epsilon_2 = 10^{-1}$ and $\epsilon_4 = 10^{-2}$, respectively. A standard value of the mesh spacing is $\Delta = 3 \times 10^{-2}$.

For the longest wavelength with λ_f of $O(1)$, fourth-difference smoothing in between two successive reflections results in an amplitude attenuation which is an order of magnitude smaller than the attenuation caused by dissipation in an unsteady boundary layer upon reflection. Second-difference smoothing results in an attenuation of $O(10\%)$ if not switched off. For higher spatial harmonics, that is shorter wavelengths, fourth-difference numerical smoothing in the freestream will start to dominate over dissipation in unsteady boundary layers due to its strong inverse dependence on the wavelength. The attenuation coefficient β_4 of the sixth harmonic approaches $O(1)$ for the above choice of Δ and ϵ_4.

This implies that numerical smoothing will dissipate waves prematurely in the freestream unless the wavelength is on the order of an axial chord or more. Weak shock waves, which dominate the unsteady interaction in the ACE turbine stage, have most of their energy in higher spatial harmonics and are subject to strong numerical dissipation, even in the absence of second-difference smoothing. The unsteady pressure gradients acting on the boundary layer, which are the input to the high-frequency-limit model, are diminished prematurely in the freestream and the level of unsteady dissipation is underpredicted. Numerical smoothing in the freestream can explain the discrepancy between the number of reflections expected based on the Unsteady Viscous Loss in the boundary layer and the number of reflections observed in an unsteady simulation. To prevent numerical smoothing from dissipating unsteady waves prematurely in the freestream, the smoothing coefficients ϵ_i and/or the grid spacing Δ must be reduced. In

many CFD-codes, like the MacCormack method [64], numerical smoothing is implicit in the formulation. Its level cannot be adjusted (other than increasing it by adding explicit smoothing). In all formulations, a minimum level of smoothing is necessary to stabilize the simulation. Thus, increasing the grid resolution, i.e reducing the grid spacing at the expense of CPU-time, remains as the only viable solution in many applications.

4.4.4 Entropy Rise in the Simulation

Figure 4.20 shows the time-mean, mass-average entropy, defined in equation (2.58), in the freestream of the rotor passage; both the steady and the unsteady viscous simulation are shown. For simplicity, the freestream was assumed to coincide with the H-grid in the rotor passage. While the freestream extends into the O-grid around the rotor blades, it is only the flow on the H-grid that is subject to numerical smoothing.

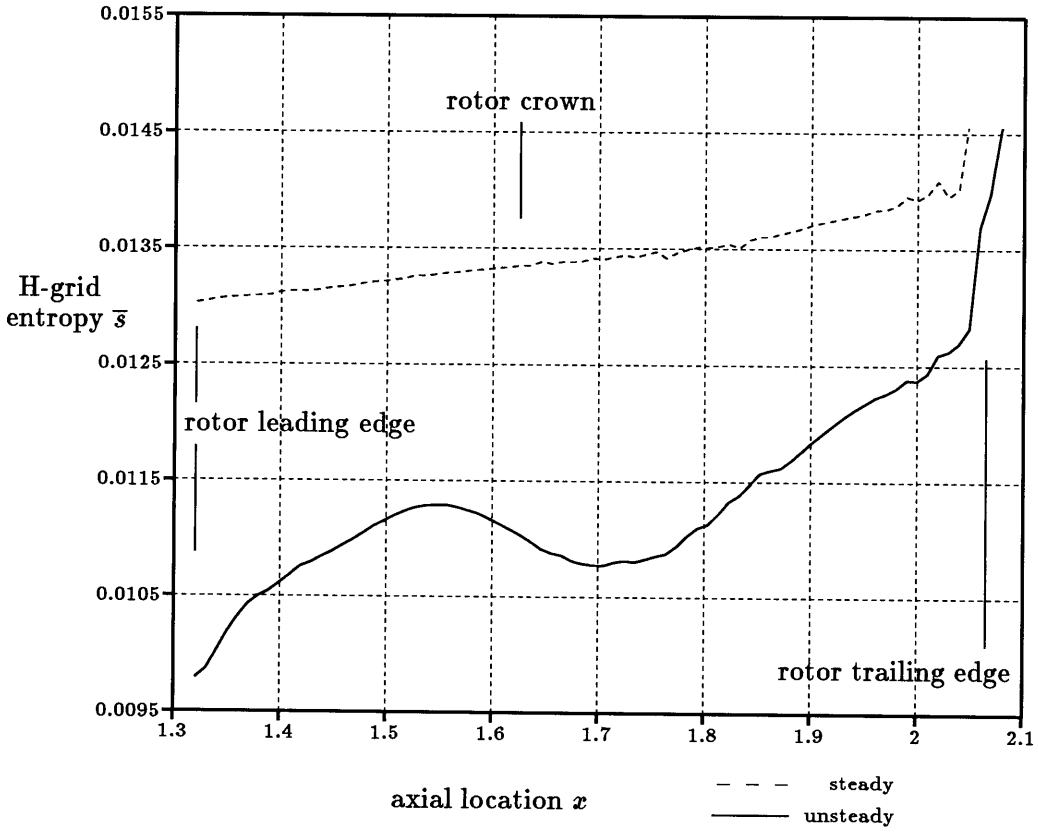

Figure 4.20: Average entropy in the rotor passage H-grid (the freestream)

The entropy rise between the rotor leading edge and the rotor trailing edge in the unsteady simulation is about three times as large as in the steady simulation. Clearly, the locus of loss increase in the unsteady simulation is in the freestream, with the primary mechanism being numerical smoothing.

Both figure 2.14 and figure 4.20 show regions in which the average entropy is axially decreasing. The decrease happens in the freestream (on the H-grid), as is seen from figure 4.20. In figure 2.14, the decrease is masked by the monotonically rising average entropy in the boundary layer contained in the O-grid. While it is not clear what mechanism causes the decrease in average entropy, it is a numerical artifact most likely linked to numerical smoothing. By its very nature, numerical smoothing mixes out the flow. In uniform mean flow, a control-volume argument as presented in chapter 2 can be used to calculate the associated entropy rise. Moreover, the entropy is guaranteed to rise monotonically in the axial direction. Second-difference smoothing mimics the action of the physical viscosity; fourth-difference smoothing has no physical counterpart in real flows. The control-volume argument allows no conclusion about the path a fluid particle's entropy takes in an unsteady nonuniform flow subject to fourth-difference numerical smoothing.

The entropy rise in the freestream cannot be discounted as a numerical artifact without physical implication. The argument was made in detail in section 2.4. While the mechanisms and the locus of unsteady loss differ in numerical simulations and real physical flows, the entropy rise in the freestream of a numerical simulation, and the associated loss, are *possibly* indicative of the level of Unsteady Viscous Loss that would be seen in the boundary layer in the absence of numerical smoothing. As was pointed out in section 2.4, the entropy rise associated with the dissipation of unsteady waves does not depend on the mechanism of dissipation. While numerical smoothing shifts the locus of dissipation into the freestream, the associated entropy rise is expected to be approximately correct. The statement is not an unqualified one because the entropy rise still depends on the mean flow state at the locus of dissipation.

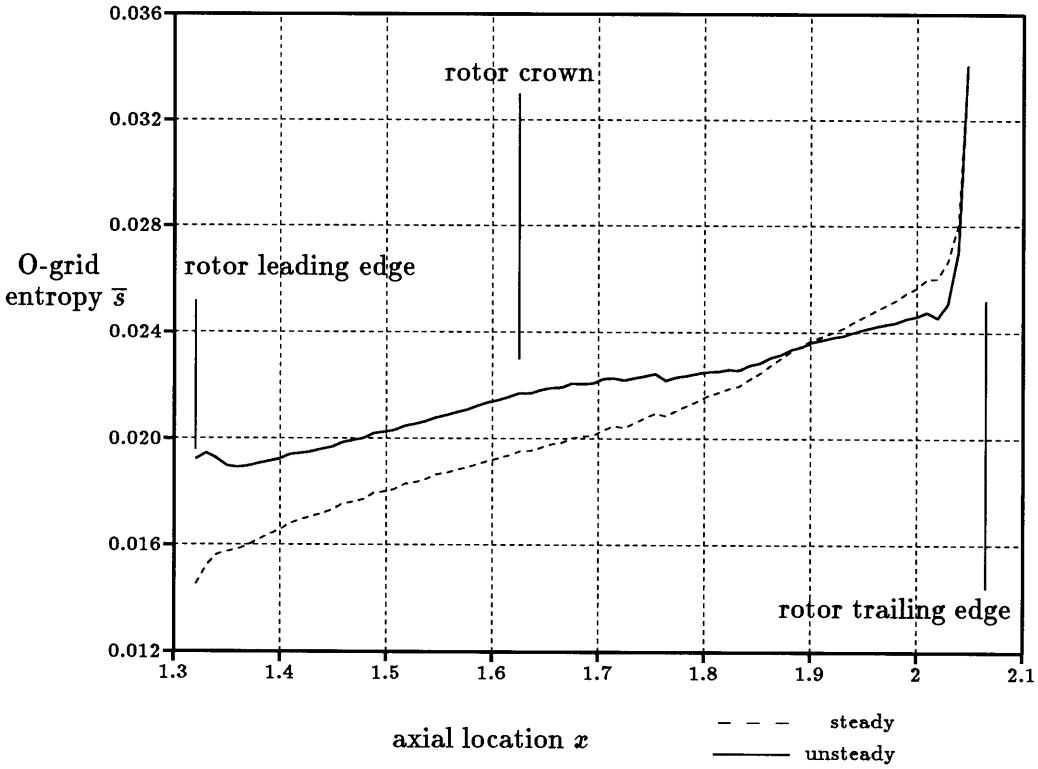

Figure 4.21: Average entropy in the O-grid (boundary layers) around the rotor blades

Figure 4.21 shows the average entropy in the O-grid. In the steady simulation, the mass-average entropy at the leading edge only slightly exceeds the uniform entropy level after mixing at the interface. Surprisingly, the time-mean mass-average entropy at the leading edge is higher in the unsteady simulation, but rises more slowly. As a consequence of the predicted Unsteady Viscous Loss, one would expect to see a steeper rise between leading edge and rotor crown in the unsteady simulation. At their nominal level, Unsteady Viscous Loss causes a rise of $\Delta\overline{s} = 2.8 \times 10^{-4}$ based on the time-mean axial mass-flux through a rotor passage. The Unsteady Viscous Loss, however, happens locally near the rotor blade surface. Based on the mass-flux in the O-grid, the average entropy rise is $O(10^{-3})$, nominally. On the entropy scale of figure 4.21, an entropy rise of $O(10^{-3})$ is still small. The major problem in interpreting figure 4.21 is the fact that the boundary between O-grid and H-grid is not a streamline. Thus, fluid is entrained in or passes out of the O-grid. The associated change in the average entropy of the O-grid masks any entropy rise due to Unsteady Viscous Loss. Without computing streamlines, it is not possible to separate the effects of entrainment and Unsteady Viscous Loss.

The blade surface itself is a streamline. Thus, a surface entropy plot does not suffer from entrainment effects. Figure 4.22 shows the time-mean entropy on the rotor surface. In the unsteady case, the mean entropy rises faster along the front portion of the suction surface, which could be attributed to Unsteady Viscous Loss. While the Unsteady Viscous Loss occurs in the near-wall region, the exact magnitude of the associated rise in the surface entropy is not known. It is not possible to determine whether the difference between the steady and the unsteady entropy rise corresponds to the generation of Unsteady Viscous Loss. On the pressure surface, there is an almost constant offset between the entropy in the steady and the unsteady case. Its magnitude roughly matches the entropy rise due to the mixing loss at the steady interface.

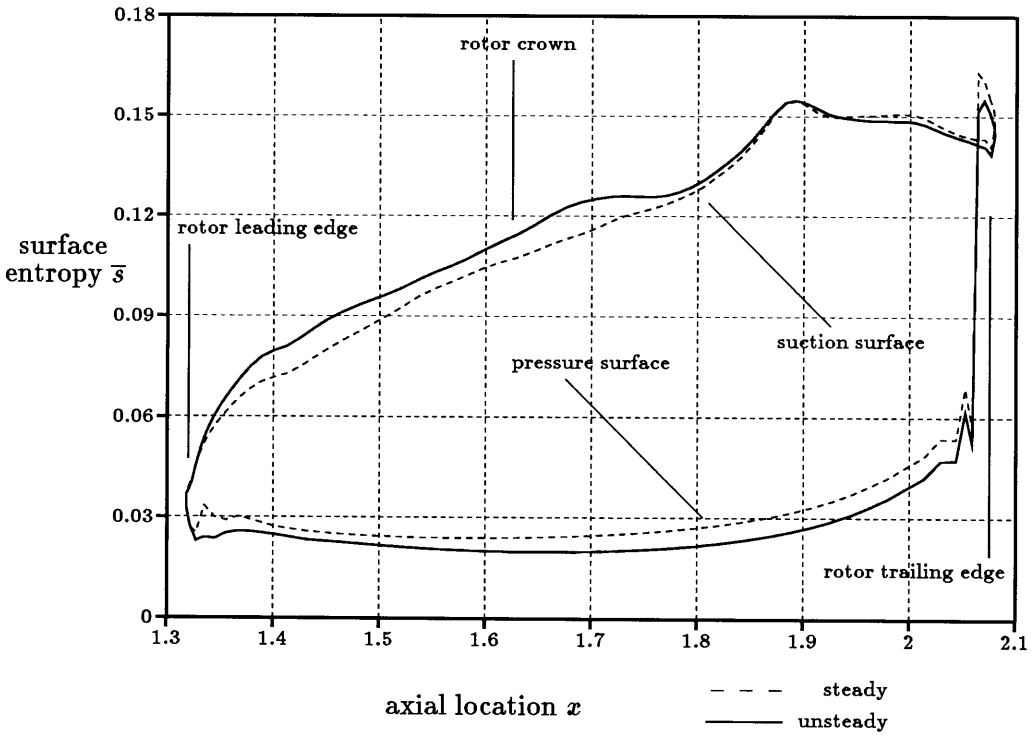

Figure 4.22: Time-mean rotor surface entropy

While Unsteady Viscous Loss could be one explanation for the difference between steady and unsteady surface entropy, it could also be due to the migration of stator wake fluid to the suction surface. Due to its velocity defect in the stator frame, the wake has a slip velocity perpendicular to the freestream in the rotor frame. Wake fluid

of higher entropy piles up on the suction side, while freestream fluid with lower entropy drifts to the pressure side.

4.5 Summary — Unsteady Viscous Loss

Based on a near-wall approximation in the high-reduced-frequency limit, a model for the Unsteady Viscous Loss with a non-zero time-mean has been formulated. The loss is due to dissipation in unsteady boundary layers driven by unsteady pressure gradients. The errors introduced into the loss model by a departure from the high-reduced frequency limit have been examined in laminar and turbulent mean flows; at high freestream Mach numbers in turbulent flow, they can be appreciable.

The loss model was applied to the ACE turbine stage, which exhibits strong interaction between oblique shock waves and the rotor blade row. The Unsteady Viscous Loss was found to be small. Nominally, i.e. without taking the loss model errors into consideration, they account for only 1.4% of the total loss in an unsteady simulation of the flow through the stage. The error band for this case is significant, allowing for an Unsteady Viscous Loss up to five times the nominal level. At that level, Unsteady Viscous Loss would be of the same magnitude as the Unsteady Circulation Loss. While still small compared to the total loss of an unsteady simulation, it could account for a third of the unsteady loss increase in the rotor passage. The ACE turbine stage is representative of current high-pressure turbine designs but its level of unsteadiness is at the upper end of the range found in turbomachinery. Generally, the level of unsteadiness, and the associated Unsteady Viscous Loss, are lower.

The loss in the rotor passage is 55% higher in the unsteady simulation than in the steady simulation. Neither the Unsteady Viscous Loss nor a change in the boundary layer character account for the magnitude of the loss increase. The dominant mechanism of loss increase was found to be numerical smoothing in the freestream. Numerical simulations damp unsteady waves by way of numerical smoothing in the freestream,

and not in unsteady boundary layers, as do real flows. As a consequence, the computed pressure gradients, which drive the model for the Unsteady Viscous Loss, can be diminished prematurely, reducing the predicted loss. While the loss increase in unsteady flow occurs in the wrong location, its level is *possibly* indicative of the Unsteady Viscous Loss that would otherwise be seen in the boundary layer. To prevent numerical smoothing from dominating, the level of numerical smoothing in simulations must be decreased. If numerical smoothing is implicit to a code, its smoothing coefficients cannot be adjusted and the grid spacing needs to be reduced.

In the simulation, it proved difficult to separate the effect of Unsteady Viscous Loss from the effects of other phenomena, in particular in the presence of numerical smoothing. At its small (nominal) magnitude, it is easily masked. The uncertainty about its exact magnitude averaged over the blade passage or the boundary layer, and lack of knowledge about its effect on the surface entropy further complicate the identification of Unsteady Viscous Loss in the simulation.

Chapter 5
Concluding Remarks

This thesis reports an analytical and numerical investigation of the second-order effects of unsteadiness on the efficiency of turbomachines, using linear, two-dimensional models. The main themes of the thesis are the identification of the physical nature and the location of unsteady loss mechanisms, the magnitude of the associated losses and their effect on the time-mean efficiency, and the assessment of the modeling accuracy of numerical simulations with respect to unsteady losses.

5.1 Summary

The thesis research consisted of three distinct parts, corresponding to chapters 2, 3, and 4. The scope and the results for each chapter are briefly summarized below.

5.1.1 Chapter 2 — Unsteadiness and Loss

Chapter 2 established, for the first time in a rigorous mathematical manner, a link between the dissipation (mixing out) of unsteadiness in a compressible flow in two dimensions and the efficiency of a turbomachine. A novel approach, involving an asymptotic analysis and a control-volume argument for a flow governed by the linearized Euler equations, related the dissipation of an arbitrary combination of unsteady waves in a uniform mean flow to an entropy rise. The entropy rise was in turn related to a change in the turbomachine performance through a linearization of the isentropic efficiency.

The unsteady waves permitted in an inviscid, compressible, linearized flow in two dimensions are convected entropy and vorticity waves and propagating, or evanescent, pressure waves. In an unsteady nonuniform flow, the time-mean of the flux-average entropy is the only loss measure with a sound physical foundation. The separate contributions to the second-order entropy rise (upon dissipation) from waves of different frequency, wave number, and physical nature were explained. It was proved that contributions from waves of different physical nature do not crosscouple and that evanescent pressure waves do not contribute to the mixing loss.

The dependence of the accuracy of the predicted entropy rise on the wave amplitudes was investigated by comparison to the numerically determined (nonlinear) entropy rise.

The loss model was employed for the first analysis of mixing loss at the stator/rotor interface of a steady simulation. At the interface, the nonuniform stator outflow is averaged to provide steady, uniform rotor inflow conditions. For the case examined, a viscous simulation of a high-pressure turbine stage called the ACE turbine stage, the mixing loss accounted for about 20% of the stage entropy rise in the steady simulation. The linear model identified the contributions from pressure waves, vorticity waves, and entropy waves to the mixing loss. The agreement between the predicted mixing loss and the (nonlinear) mixing loss observed in the steady simulation was excellent, despite the large magnitude of the perturbations in the stator outflow. It was pointed out that, as a consequence of the averaging at the stator/rotor interface, the steady simulation of a stage can have a lower efficiency than the corresponding unsteady simulation. This aspect of steady simulations seems to have gone unrecognized, so far.

It is also relevant to note that *Mathematica*®, a software package for performing symbolic mathematical manipulations by computer, proved to be an extremely useful tool in carrying out the extensive manipulations required by the asymptotic analysis.

5.1.2 Chapters 3 and 4 — Unsteady Loss Mechanisms

The thesis treated two unsteady loss mechanisms in a 2D, linearized framework. They are called Unsteady Circulation Loss and Unsteady Viscous Loss, respectively.

Chapter 3 — Unsteady Circulation Loss

Unsteady Circulation Loss results from the transfer of mean-flow energy to kinetic energy associated with vorticity shed at the trailing edges of a blade row. In accordance with Kelvin's Circulation Theorem, the vorticity is shed in response to a time-varying blade circulation. The kinetic energy associated with the shed vorticity is unlikely to be recovered and is thus related to an efficiency drop as detailed in chapter 2.

While Unsteady Circulation Loss has been considered previously, this thesis presented the first application of numerical simulations to the loss mechanism. The use of circulation amplitudes determined from simulations allows one to obtain Unsteady Circulation Losses for arbitrary blade and/or stage geometries and Mach numbers. Eliminating the need to estimate the circulation amplitudes or to deduce them from thin-airfoil theory results in a realistic loss measure for modern turbomachines.

The Unsteady Circulation Losses were found to be small. For the case with the strongest unsteady interaction between blade rows, the ACE turbine stage, Unsteady Circulation Loss led to a drop in the isentropic stage efficiency of only 0.3%.

The most important interaction mechanisms leading to an unsteady circulation were found to be wake/blade row interaction and oblique shock wave/blade row interaction. Potential interaction played a minor role only. In the so-called NASA-stage 67 compressor, for example, Unsteady Circulation Loss led to a drop in the efficiency of only 0.03% for the smallest gap between blade rows.

The circulation amplitudes were found to be surprisingly small, i.e. $O(1\%)$ of the time-mean circulation. Even the ACE turbine stage with a 40% peak-to-peak variation

in the rotor lift, only showed a peak-to-peak variation in the rotor circulation of 5.5%.

No further work is required on the subject of Unsteady Circulation Loss because its magnitude has been clearly established and was found to be small.

Chapter 4 — Unsteady Viscous Loss

The unsteady stator/rotor interaction can generate strong pressure waves. Unsteady Viscous Loss is a consequence of dissipation in unsteady boundary layers driven by these pressure waves. The proposed loss model represents the first attempt to model Unsteady Viscous Loss.

A high-reduced-frequency limit was used to obtain the streamwise velocity distribution in the laminar Stokes sublayer driven by unsteady pressure gradients. The driving pressure gradients were obtained from a simulation. In the high-frequency limit, the dissipation in unsteady boundary layers depends only on the unsteady shear. The associated entropy rise was again related to a drop in the isentropic efficiency.

To check the errors introduced by a departure from the high-reduced-frequency limit, a numerical study was performed on a flat plate boundary layer subject to a pressure wave disturbance. The accuracy of the predicted dissipation was shown to depend primarily on the freestream Mach number and the ratio of the laminar sublayer thickness (of the turbulent mean flow) to the unsteady boundary layer thickness.

The loss model was applied to the ACE-turbine stage. Unsteady Viscous Loss was predicted to cause a drop in the isentropic stage efficiency of 0.09%. Compared to the total loss in an unsteady viscous simulation, this is a very small contribution; it accounts for only 1.4% of the total loss. Taking into account errors due to modeling approximations, the loss could be at most five times the predicted level. At that level, it would be roughly of the same magnitude as the Unsteady Circulation Loss but remain a small contribution, accounting for no more than 7.1% of the total loss.

Unsteady Viscous Loss could, however, account for about one third of the loss increase in the rotor passage observed in the unsteady simulation over the level in the corresponding steady simulation. Analytical considerations and detailed examination of the simulations showed that the increase is induced primarily by numerical smoothing. Numerical smoothing shifts the primary locus of unsteady loss from boundary layers into the freestream. Pressure waves, which constitute the input to the loss model, are attenuated prematurely in the freestream, reducing the predicted level of Unsteady Viscous Loss. The magnitude of the loss increase in the freestream of the unsteady simulation is possibly indicative of the levels of Unsteady Viscous Loss that would otherwise appear in unsteady boundary layers.

The thesis contains the first investigation on the origin of the increase in loss seen in the rotor passage of an unsteady viscous simulation. The finding that there can be different unsteady loss mechanisms and loci in physical flows and simulations, is an important one. Since unsteady simulations are used to assess the performance of turbomachinery, the potential problems and the limitations of CFD-codes need to be understood.

In contrast to Unsteady Circulation Loss, Unsteady Viscous Loss requires future work to address the problems identified in the course of this thesis.

Synopsis of Unsteady Loss

The contributions of the unsteady loss mechanisms considered to the overall loss in a stage with a high level of unsteadiness are small, but not negligible if an accurate account of the loss sources and the time-mean efficiency are required. This is particularly true as long as the magnitude of Unsteady Viscous Loss cannot be established more accurately.

As discussed above, Unsteady Viscous Loss could be a significant contributor to unsteady loss. A less conditional statement must await additional research into the effect of numerical smoothing and modeling approximations on the predicted level of Unsteady Viscous Loss.

5.2 Future Work Recommendations

5.2.1 Chapter 2 — Unsteadiness and Loss

Chapter 2 linked unsteady waves to the entropy rise upon their dissipation. While it was concluded that little of the energy associated with unsteady waves can be recovered, a closer analytical study of rectification mechanisms in turbomachines and a quantitative measure of rectification would be highly desirable.

References on wave reflection and transmission through blade rows did not provide a clear picture on reflection and transmission coefficients. The coefficients vary greatly, depending on the exact choice of parameters like Mach number, incidence angle, and stagger angle. None of the references treated geometries realistic for turbomachinery. Therefore, it was difficult to make a general conclusion about the relative importance of transmission versus reflection, and ultimately about the locus of dissipation.

If an unsteady wave is not dissipated 'in place', but only after transmission through blade rows, it may extract additional energy from the mean flow. Also, if dissipation of unsteady waves happens in a nonuniform mean flow, the associated loss is not known. The asymptotic analysis for a control volume holds only in a uniform mean flow. Both of the above issues should be addressed analytically.

An experiment, measuring the unsteady flow field of a turbine stage with the spatial and temporal resolution required to identify the unsteady waves, could provide answers to the above questions. Knowing the wave content at the stator/rotor interface and the outflow boundary would allow one to draw a conclusion about the relative importance of reflection versus transmission and the locus of dissipation.

5.2.2 Chapter 4 — Unsteady Viscous Loss

Chapter 4 treated Unsteady Viscous Loss and applied the loss model to the ACE turbine stage. The predicted loss was small, but its magnitude was not well-defined due to modeling approximations and the action of numerical smoothing.

Numerical smoothing was found to shift the primary locus of unsteady loss in numerical simulations from boundary layers into the freestream. While loss mechanisms and locations differ in physical flows and numerical simulations, the entropy rise in the freestream is possibly indicative of the level of Unsteady Viscous Loss in physical flows. Therefore, the first step in any future work should be an analytical assessment of the consequences stemming from differing mechanisms and locations of unsteady loss if the predicted level of unsteady loss is realistic.

Since numerical smoothing is necessary to stabilize CFD-codes, and in many cases is implicit in the numerical method, the only way to reduce nonphysical losses in the freestream is to increase the grid resolution at the expense of CPU-time. Careful benchmark calculations with high grid resolution are recommended to establish the resolution required to have identical dissipation mechanism in simulated and real flows.

Experiments focusing on the unsteady pressure gradients on the blade surfaces are suggested; these could be used for two purposes. First, they could be compared to pressure gradients obtained in a numerical simulation to give some guidance as to when the dissipation mechanism in a simulation is physically realistic. Second, the data could be used as an alternate source of input to a loss model.

Once the input, i.e. the unsteady pressure gradients, can be trusted, an improved loss model should be developed. In the present formulation, the errors in the predicted dissipation are appreciable when the model is applied to turbomachinery flows of practical interest. A model like the one used for the numerical error evaluation could be employed to account for turbulent mean flows and mean-flow convection.

Bibliography

[1] D.R. Lindquist. *Computation of Unsteady Transonic Flowfields Using Shock Capturing and the Linear Perturbation Euler Equations.* Ph.D. Thesis, Massachusetts Institute of Technology, Dezember 1991.

[2] K.C. Hall. *A Linearized Euler Analysis of Unsteady Flow in Turbomachinery.* Ph.D. Thesis, Massachusetts Institute of Technology, 1987.

[3] J.J. Adamzcyk. *Model Equations for Simulating Flows in Multistage Turbomachinery.* ASME Paper 85-GT-226, 1985.

[4] M.B. Giles. *A Framework for Multi-Stage Unsteady Flow Calculations.* Conference proceedings of the 6^{th} International Symposium on Unsteady Aerodynamics, Aeroacoustics, and Aeroelasticity of Turbomachines and Propellers, University of Notre Dame, 1991.

[5] M.B. Giles. *Calculations of Unsteady Wake/Rotor Interactions.* Journal of Propulsion and Power 4(4), 1988.

[6] M.B. Giles. *Stator/Rotor Interaction in a Transonic Turbine.* Journal of Propulsion and Power 6(5), 1990.

[7] M.B. Giles and R. Haimes. *Validation of a Numerical Method for Unsteady Flow Calculations.* ASME Paper 91-GT-271, 1991.

[8] M.B. Giles and R. Haimes. *Advanced Interactive Visualization For CFD.* Computing Systems in Engineering 1(1), 1990.

[9] H.P. Hodson. *Boundary Layer and Loss Measurements on the Rotor of an Axial-Flow Turbine.* ASME Paper 83-GT-4, 1983.

[10] C. Keller. *Energy Losses on High-Speed Turbomachines Resulting from Irregular Flow to the Runner Wheel.* Escher-Wyss News, March/April 1935.

[11] N.H. Kemp and W.R. Sears. *On the Wake Energy of Moving Cascades.* Journal of Applied Mechanics 23, June 1956.

[12] Th. von Karman and W.R. Sears. *Airfoil Theory for Non-Uniform Motion.* Journal of the Aeronautical Sciences 5, August 1938.

[13] W.R. Sears. *Some Aspects of Non-Stationary Airfoil Theory and Its Practical Applications.* Journal of the Aeronautical Sciences 8, January 1941.

[14] N.H. Kemp and W.R. Sears. *On the Lift and Circulation of Airfoils in Some Unsteady-Flow Problems.* Journal of Aeronautical Sciences 19, October 1952.

[15] N.H. Kemp and W.R. Sears. *Aerodynamic Interference Between Moving Blade Rows.* Journal of the Aeronautical Sciences 20, September 1953.

[16] W.R. Hawthorne. *Flow Through Moving Cascades of Lifting Lines with Fluctuating Lift.* Journal of Mechanical Engineering Science 15(1), 1973.

[17] J.L. Kerrebrock and A.A. Mikolajczak. *Intra-Stator Transport of Rotor Wakes and Its Effect on Compressor Performance.* Journal of Engineering for Power, 1970.

[18] W.F. Ng, A.H. Epstein. *Unsteady Losses in Transonic Compressors.* Journal of Engineering for Power 107(2), 1985.

[19] A.J. Strazisar *Investigation of Flow Phenomena in a Transonic Rotor Using a Laser Anemometer.* Journal of Engineering for Power 107(2), 1985.

[20] M.D. Hathaway, J.Gertz, A. Epstein, and A.J. Strazisar. *Rotor Wake Characteristics of a Transonic Axial Flow Fan.* AIAA Paper 85-1133, 1985.

[21] P.R. Owen. *Computational Simulation of Unsteady Flow in a Transonic Compressor Rotor.* MIT S.M.-Thesis, 1986.

[22] L.H. Smith. *Casing Boundary Layers in Multistage Axial Flow Compressors.* Flow Research in Blading, edited by L.S. Dzung, Elsevier Publishing Company, Amsterdam, 1970.

[23] A.A. Mikolajczak. *The Practical Importance of Unsteady Flow.* AGARD-CP 177.

[24] R. Hetherington and R.R. Moritz. *The Influence of Unsteady Flow Phenomena on Design and Operation of Aero Engines.* AGARD-CP 177.

[25] A.O. Lopatitskii et al. *Energy Losses in the Transient State of an Incident Flow on the Moving Blades of Turbine Stages.* Energomashinostroenie 15, 1969.

[26] I.Y. Kirillov, A.S. Laskin and C.G. Shpenzer *Influence of Unsteadiness of the Flow on Efficiency of Turbine Stages.* Teploenergetika 17(10), 1970.

[27] V.Y. Yurinskiy and I. Shestachenko. *Losses in an Impulse Turbine Cascade in an Unsteady Flow.* Fluid Mechanics-Soviet Research 3(1), 1974.

[28] H.J. Obremski and A.A. Feier. *Transition in Oscillatory Boundary Layer Flows.* Journal of Fluid Mechanics 29(1), 1967.

[29] G.J. Walker. *The Unsteady Nature of Boundary Layer Transition on an Axial-Flow Compressor Blade.* ASME Paper 74-GT-135, 1974.

[30] H. Pfeil, R. Herbst. *Transition Process of Instationary Boundary Layers.* ASME Paper 79-GT-128, 1979.

[31] H. Pfeil, R. Herbst and T. Schröder. *Investigation of the Laminar-Turbulent Transition of Boundary Layers Disturbed by Wakes.* ASME Paper 82-GT-124, 1982.

[32] R.L. Evans. *Boundary Layer Development on an Axial-Flow Compressor Stator Blade.* Journal of Engineering for Power 100, 1978.

[33] R.P. Dring, H.D. Joslyn, L.W. Hardin, J.H. Wayner. *Turbine Rotor-Stator Interaction.* ASME Paper 82-GT-3, 1982.

[34] H.P. Hodson. *Modeling Unsteady Transition and Its Effect on Profile Loss.* AGARD-CP-468.

[35] J.D. Doorly and M.L.G. Oldfield. *Simulation of the Effects of Shock-Wave Passing on a Turbine Rotor Blade.* Journal of Engineering for Gas Turbines and Power 107(4), 1985.

[36] D.S. Whitehead. *The Calculation of Steady and Unsteady Transonic Flow in Cascades.* University of Cambridge, Department of Engineering Report CUED/A-Turbo/TR 118, 1982.

[37] J.M. Verdon and J.R. Caspar. *A Linearized Unsteady Aerodynamic Analysis for Transonic Cascades.* Journal of Fluid Mechanics 149, 1984.

[38] R.H. Ni and F. Sisto. *Numerical Computations of Non-Stationary Aerodynamics of Flat Plate Cascades in Compressible Flow.* ASME Paper 75-GT-5, 1975.

[39] R.H. Ni. *A Multiple-Grid Scheme for Solving the Euler-Equations.* AIAA Journal 20(11).

[40] R.H. Ni and J.C. Bogoian. *Prediction of 3D Multistage Turbine Flow Fields Using a Multiple-Grid Euler Solver.* AIAA Paper 89-0203, 1989.

[41] M.M. Rai. *A Relaxation Approach to Patched-Grid Calculations with the Euler Equations.* Journal of Computational Physics 66(1), 1986.

[42] H.P. Hodson. *An Inviscid Blade-to-Blade Prediction of a Wake-Generated Unsteady Flow.* ASME Paper 84-GT-43, 1984.

[43] J.D. Denton. *An Improved Time-Marching Method for Turbomachinery Flow Calculations.* ASME Paper 82-GT-239, 1982.

[44] M.M. Rai. *Navier-Stokes Simulations of Rotor-Stator Interaction Using Patched and Overlaid Grids.* ASME Paper 85-1519, 1985.

[45] J.D. Doorly and M.L.G. Oldfield. *Simulation of Wake-Passing in a Stationary Turbine Rotor Cascade.* Journal of Propulsion and Power 1(4), 1985.

[46] T.L. Butler, O.P. Sharma, H.D. Joslyn and R.P. Dring. *Inlet Temperature Distortion in an Axial Flow Turbine Stage.* AIAA Paper 86-1468, 1986.

[47] B. Krouthen. *Numerical Investigation of Hot Streaks in Turbines.* MIT, Computational Fluid Dynamics Lab, CFDL-TR-88-9, 1988.

[48] R.H. Ni and R. Takahashi. *Hot Streak Migration Through a Turbine Stage - An Unsteady Flow Simulation.* NASA-MSFC CFD-workshop.

[49] M.M. Rai and R.P. Dring. *Navier-Stokes Analysis of Redistribution of Inlet Temperature Profiles in a Turbine.* AIAA Paper 87-2146, 1987.

[50] G.R. Guenette, A.H. Epstein, M.B. Giles, R. Haimes, and R.J.G. Norton. *Fully Scaled Transonic Turbine Rotor Heat Transfer Measurements.* ASME Paper 88-GT-171, 1988.

[51] R.S. Abhari, G.R. Guenette, A.H. Epstein, and M.B. Giles. *Comparison of Time-Resolved Turbine Rotor Blade Heat Transfer Measurements and Numerical Calculations.* ASME Paper 91-GT-268, 1991.

[52] D.A. Ashworth, J.E. LaGraff, D.L. Schultz, and K.J. Grindrot. *Unsteady Aerodynamic and Heat Transfer Processes in a Transonic Turbine Stage.* Journal of Engineering for Gas Turbine and Power 107, 1985.

[53] R.J. Boyle, J.E. Haas, and T. Katsanis. *Predicted Turbine Stage Performance Using Quasi-Three-Dimensional and Boundary-Layer Analysis.* Journal of Propulsion and Power 1(3), 1985. York, 1974.

[54] A.B. Johnson, M.J. Rigby, M.L.G. Oldfield, R.W. Ainsworth, and M.J. Oliver. *Surface Heat Transfer Fluctuations on a Turbine Rotor Blade due to Upstream Shock Wave Passing.* ASME Paper 88-GT-172, 1988.

[55] M.B. Giles. *Non-Reflecting Boundary Conditions for the Euler Equations.* MIT-CFDL-Report, CFDL-TR-88-1, February 1988.

[56] R.K. Amiet. *Transmission and Reflection of Sound by Two Blade Rows.* Journal of Sound and Vibrations 34(3), 1974.

[57] S. Kaji and T. Okazaki. *Propagation of Sound Waves Through a Blade Row. Part I: Analysis Based on the Semi-Actuator Disk Theory.* Journal of Sound and Vibrations 11(3), 1970.

[58] S. Kaji and T. Okazaki. *Propagation of Sound Waves Through a Blade Row. Part II: Analysis Based on the Acceleration Potential Method.* Journal of Sound and Vibrations 11(3), 1970.

[59] R.S. Muir. *The Application of a Semi-Actuator Disk Model to Sound Transmission Calculations in Turbomachinery, Part I:The Single Blade Row.* Journal of Sound and Vibrations 54(3), 1977.

[60] P.J. Grooth *Wave Reflection by a Flat Plate Cascade.* Master's Thesis, Massachusetts Institute of Technology, September 1990.

[61] P.E. Doak. *Momentum Potential Theory of Energy Flux Carried by Momentum Fluctuations.* Journal of Sound and Vibrations 131(1), 1989.

[62] O.S. Ryshov and G.M. Shefter. *On the Energy of Acoustic Waves Propagating in a Moving Media.* Journal of Applied Mathematics and Mechanics 26, 1962.

[63] W. Eversman. *Acoustic Energy in Ducts:Further Observations.* Journal of Sound and Vibrations 62(4), 1979.

[64] R.W. McCormack *A Numerical Method for Solving the Equations of Compressible Viscous Flow.* AIAA Paper 81-0110, 1981.

[65] L. N. Cattafesta. *An Experimental Investigation of the Effects of Inlet Radial Temperature Profiles on the Aerodynamic Performance of a Transonic Turbine Stage.* Master's Thesis, Massachusetts Institute of Technology, August 1988.

[66] C.F. Gerald and P.O. Wheatley *Applied Numerical Analysis,* 3rd edition, chapter 4. Addison-Wesley Publishing Company, 1984.

[67] M.B. Giles. *UNSFLO: A Numerical Method for Calculating Unsteady Stator/Rotor Interaction.* Technical Report TR-86-6, MIT Computational Fluid Dynamics Laboratory, October 1988.

[68] J.D. Denton. *The Calculation of Three-Dimensional Viscous Flow Through Multistage Turbomachines* ASME Paper 90-GT-19, 1990.

[69] H.P. Hodson. *Measurements of Wake-Generated Unsteadiness in the Rotor Passages of Axial Flow Turbines.* ASME Paper 84-GT-189, 1984.

[70] N.H. Kemp and W.R. Sears. *The Unsteady Forces Due to Viscous Wakes in Turbomachines.* Journal of the Aeronautical Sciences 22, July 1955.

[71] T.P. Korakianitis. *A Design Method for the Prediction of Unsteady Forces on Subsonic, Axial Gas-Turbine Blades.* Sc.D.-Thesis, Massachusetts Institute of Technology, July 1987.

[72] H.D. Joslyn, R.P. Dring, and O.P. Sharma. *Unsteady Three-Dimensional Turbine Aerodynamics.* Journal of Engineering for Power 105, April 1983.

[73] A. Binder. *Instationäre Strömungsvorgänge im Laufrad einer Turbine.* Doctoral Thesis, RWTH Aachen, December 1985.

[74] D.C. Urasec, W.T. Correll, and W.S. Cunnan. *Performance of a Two-Stage Fan Having Low-Aspect-Ratio First-Stage Rotor Blading.* NASA TP-1493, August 1979.

[75] M.D. Hathaway, T.H. Okiishi, A.J. Strazisar, and J.J. Adamczyk. *Measurements of the Unsteady Flow Field within the Stator Row of a Transonic Axial Flow Fan.* ASME Papers 87-GT-226 and 87-GT-227, 1987.

[76] J.R. Wood, A.J. Strazisar, and P.S. Simonyi, and W.T. Correll. *Shock Structure in a Transonic Fan Using Laser Anemometry.* AGARD CP-401, September 1986.

[77] T. Shang. *Blade Row Interaction Effects on Compressor Measurements.* Master's Thesis, Massachusetts Institute of Technology, August 1989.

[78] D.P. Telionis. *Unsteady Viscous Flow,* Chapter 7, Springer Verlag, 1981.

[79] G. Binder, S. Tardu, R.F. Blackwelder, and J.L. Kueny. *Large Amplitude Periodic Oscilations in the Wall Region of a Turbulent Channel Flow.* Proceedings of the 5*th* Symposium on Turbulent Shear Flows, Cornell, 1985.

[80] S.K.F. Karlsson. *An Unsteady Turbulent Boundary Layer.* Journal of Fluid Mechanics 5, 1959.

[81] P.G. Parikh, W.C. Reynolds, R. Jayaramon. *Behavior of an Unsteady Turbulent Boundary Layer.* AIAA Journal 20, 1982

[82] D. B. Spalding. *A Single Formula for the "Law of the Wall".* Journal of Applied Mechanics 28, 1961.

[83] D.E. Coles. *The Law of the Wake in the Turbulent Boundary Layer.* Journal of Fluid Mechanics 1, 1956.

[84] H. Schlichting. *Boundary Layer Theory,* 7th edition, chapter XIII. McGraw-Hill Book Company, New York, 1978.

[85] P.S. Klebanoff. *Characteristics of Turbulence in a Boundary Layer with Zero Pressure Gradient.* NACA Report 1247, 1955.

[86] W.J. Cook, J.D. Murphy, F.K. Owen. *An Experimental and Computational Study of Turbulent Boundary Layers in Oscillating Flows.* Fifth Symposium on Turbulent Shear Flows, Cornell University, Ithaca, N.Y., August 1985.

[87] J. Cousteix, R. Houdeville. *Unsteady Boundary Layers.* VKI Lecture Series on Turbulent Shear Flows, Von Kármán Institute, Brussels.

[88] B.R. Ramaprian, S.W. Tu, A.N. Menedez. *Periodic Turbulent Shear Flows.* Fourth Symposium on Turbulent Shear Flows, Universität Karlsruhe, F.R.G., September 1983.

[89] M.J. Lighthill. *The Response of Laminar Skin Friction and Heat Transfer to Fluctuations in the Stream Velocity.* Proceedings of the Royal Society A, Volume 224, June 1954.

[90] J. Cousteix, A. Desopper, R. Houdeville. *Structure and Development of a Turbulent Boundary Layer in an Oscillatory Outer Flow.* Proceedings of the First Symposium on Turbulent Shear Flows, Penn State University, 1977.

[91] T. Cebeci and A.M.O. Smith. *Analysis of Turbulent Boundary Layers.* Academic Press, New York, 1974.

Appendix A

Derivatives of the Axial Flux Vector

$$\frac{dF}{dU} = \begin{bmatrix} u & \rho & 0 & 0 \\ u^2 & 2\rho u & 0 & 1 \\ uv & \rho v & \rho u & 0 \\ \frac{u}{2}\left(u^2+v^2\right) & \frac{\gamma}{\gamma-1}p + \frac{\rho}{2}\left(3u^2+v^2\right) & \rho uv & \frac{\gamma}{\gamma-1}u \end{bmatrix}$$

$$\frac{d^2F_1}{dU^2} = \begin{bmatrix} 0 & 1 & 0 & 0 \\ 1 & 0 & 0 & 0 \\ 0 & 0 & 0 & 0 \\ 0 & 0 & 0 & 0 \end{bmatrix} \qquad \frac{d^2F_2}{dU^2} = \begin{bmatrix} 0 & 2u & 0 & 0 \\ 2u & 2\rho & 0 & 0 \\ 0 & 0 & 0 & 0 \\ 0 & 0 & 0 & 0 \end{bmatrix}$$

$$\frac{d^2F_3}{dU^2} = \begin{bmatrix} 0 & v & u & 0 \\ v & 0 & \rho & 0 \\ u & \rho & 0 & 0 \\ 0 & 0 & 0 & 0 \end{bmatrix} \qquad \frac{d^2F_4}{dU^2} = \begin{bmatrix} 0 & \left(u^2+\frac{u^2+v^2}{2}\right) & uv & 0 \\ \left(u^2+\frac{u^2+v^2}{2}\right) & 3\rho u & \rho v & \frac{\gamma}{\gamma-1} \\ uv & \rho v & 0 & 0 \\ 0 & \frac{\gamma}{\gamma-1} & 0 & 0 \end{bmatrix}$$

$$H_1 = \begin{bmatrix} 0 & \frac{-1}{2M_x} & 0 & 0 \\ \frac{-1}{2M_x} & \left(\frac{\gamma-1}{2}-1\right) & 0 & \frac{\gamma}{2M_x} \\ 0 & 0 & \frac{\gamma-1}{2} & 0 \\ 0 & \frac{\gamma}{2M_x} & 0 & 0 \end{bmatrix} \qquad H_2 = M_x \begin{bmatrix} 0 & \frac{M_x}{2} & 0 & 0 \\ \frac{M_x}{2} & \left(1-\frac{\gamma-1}{2}\right) & 0 & \frac{-\gamma}{2M_x} \\ 0 & 0 & \frac{1-\gamma}{2} & 0 \\ 0 & \frac{-\gamma}{2M_x} & 0 & 0 \end{bmatrix}$$

$$H_3 = \begin{bmatrix} 0 & 0 & -\frac{1}{2} & 0 \\ 0 & 0 & -\frac{1}{2M_x} & 0 \\ -\frac{1}{2} & -\frac{1}{2M_x} & 0 & 0 \\ 0 & 0 & 0 & 0 \end{bmatrix} \qquad H_4 = M_x^2 \begin{bmatrix} 0 & -\frac{1}{2M_x} & 0 & 0 \\ -\frac{1}{2M_x} & \frac{\gamma-1}{2}-\frac{1}{M_x^2} & 0 & \frac{\gamma}{2M_x} \\ 0 & 0 & \frac{\gamma-1}{2} & 0 \\ 0 & \frac{\gamma}{2M_x} & 0 & 0 \end{bmatrix}$$

Appendix B

Derivatives of the Axial Entropy Flux

$$\frac{dS}{dU_p} = \begin{bmatrix} u(s - c_p) & \rho s & 0 & \frac{M_x c_p}{a} \end{bmatrix}$$

$$\frac{d^2 S}{dU_p^2} = \begin{bmatrix} -\frac{u c_p}{\rho} & (s - c_p) & 0 & \frac{M_x c_p}{\rho a} \\ (s - c_p) & 0 & 0 & \frac{c_p}{a^2} \\ 0 & 0 & 0 & 0 \\ \frac{M_x c_p}{\rho a} & \frac{c_p}{a^2} & 0 & -\frac{M_x c_p}{ap} \end{bmatrix}$$

$$D = \frac{1}{2} \begin{bmatrix} 1 & 0 & 0 & -1 \\ 0 & (\gamma - 1) & 0 & \frac{\gamma - 1}{M_x} \\ 0 & 0 & (\gamma - 1) & 0 \\ -1 & \frac{\gamma - 1}{M_x} & 0 & \gamma \end{bmatrix}$$

Appendix C

Orthogonalities of Trigonometric Functions

$$\frac{1}{2\pi}\int_0^{2\pi} \sin(m_i x)\sin(m_j x + \varphi)dx = \delta_{ij}\frac{\cos(\varphi)}{2} \quad |m| = 1, 2, 3, \ldots$$

$$\frac{1}{2\pi}\int_0^{2\pi} \cos(m_i x)\cos(m_j x + \varphi)dx = \delta_{ij}\frac{\cos(\varphi)}{2} \quad |m| = 1, 2, 3, \ldots$$

$$\frac{1}{2\pi}\int_0^{2\pi} \sin(m_i x)\cos(m_j x)dx = 0 \quad |m| = 1, 2, 3, \ldots$$

The Kronecker delta δ_{ij} is defined such that

$$\delta_{ij} = \begin{cases} 0 & \text{if} \quad i \neq j \\ 1 & \text{if} \quad i = j \end{cases} .$$

Appendix D

Separation Properties for Non-Evanescent Pressure Waves

In accordance with equation (2.37), one has to show that the following three relations hold in order to prove that there is no crosscoupling between the two propagating pressure waves, and between vorticity waves and propagating pressure waves:

$$\overline{\tilde{u}_3\tilde{u}_4} + \overline{\tilde{v}_3\tilde{v}_4} + \overline{\tilde{p}_3\tilde{p}_4} + \frac{\overline{\tilde{p}_3\tilde{u}_4} + \overline{\tilde{p}_4\tilde{u}_3}}{M_{x,0}} = 0$$

$$\overline{\tilde{u}_3\tilde{u}_2} + \overline{\tilde{v}_3\tilde{v}_2} + \frac{\overline{\tilde{p}_3\tilde{u}_2}}{M_{x,0}} = 0$$

$$\overline{\tilde{u}_4\tilde{u}_2} + \overline{\tilde{v}_4\tilde{v}_2} + \frac{\overline{\tilde{p}_4\tilde{u}_2}}{M_{x,0}} = 0$$

The right eigenvectors $\vec{w}_{r,i} = [\hat{\rho}, \hat{u}, \hat{v}, \hat{p}]_i^T$ are defined by

$$\vec{w}_2 = \begin{bmatrix} 0 \\ -M_{x,0} \\ \Omega - M_{y,0} \\ 0 \end{bmatrix} \quad \text{and} \quad \vec{w}_{3,4} = \begin{bmatrix} -\left(\pm RM_{x,0} - 1\right) \\ \left(\pm R - M_{x,0}\right) \\ \left(1 - R^2\right)\left(\Omega - M_{y,0}\right) \\ -\left(\pm RM_{x,0} - 1\right) \end{bmatrix}.$$

The subscripts '2', '3', and '4' denote a vorticity wave, a downstream and an upstream propagating pressure wave, respectively. R and Ω are defined by

$$R = \sqrt{1 - \frac{1 - M_{x,0}^2}{\left(\Omega - M_{y,0}\right)^2}} \quad \text{and} \quad \Omega = \frac{\omega_f}{a_0 k_y}.$$

Let α denote the phase angle between the complex pressure amplitudes $\hat{p}_3$ and $\hat{p}_4$ and β the phase angle between the complex axial velocity $\hat{u}_2$ of the vorticity wave and the complex pressure $\hat{p}_3$ of a downstream propagating pressure wave.

Looking at the individual pressure wave crosscoupling terms, one can derive the

following relations:

$$\overline{\widetilde{p}_3\widetilde{p}_4} = +\frac{|\widehat{p}_3\widehat{p}_4|}{2}\cos\alpha$$

$$\frac{\overline{\widetilde{p}_3\widetilde{u}_4}}{M_{x,0}} = -\frac{R+M_{x,0}}{(1+RM_{x,0})M_{x,0}}\overline{\widetilde{p}_3\widetilde{p}_4} = -\frac{R+M_{x,0}}{(1+RM_{x,0})M_{x,0}}\frac{|\widehat{p}_3\widehat{p}_4|}{2}\cos\alpha$$

$$\frac{\overline{\widetilde{p}_4\widetilde{u}_3}}{M_{x,0}} = +\frac{R-M_{x,0}}{(1-RM_{x,0})M_{x,0}}\overline{\widetilde{p}_3\widetilde{p}_4} = +\frac{R-M_{x,0}}{(1-RM_{x,0})M_{x,0}}\frac{|\widehat{p}_3\widehat{p}_4|}{2}\cos\alpha$$

$$\overline{\widetilde{u}_3\widetilde{u}_4} = -\frac{R+M_{x,0}}{(1+RM_{x,0})}\frac{R-M_{x,0}}{(1-RM_{x,0})}\overline{\widetilde{p}_3\widetilde{p}_4} = -\frac{R^2-M_{x,0}^2}{1-R^2M_{x,0}^2}\frac{|\widehat{p}_3\widehat{p}_4|}{2}\cos\alpha$$

$$\overline{\widetilde{v}_3\widetilde{v}_4} = +\frac{(1-R^2)^2(\Omega-M_{y,0})^2}{1-R^2M_{x,0}^2}\overline{\widetilde{p}_3\widetilde{p}_4} = +\frac{(1-R^2)\left(1-M_{x,0}^2\right)}{1-R^2M_{x,0}^2}\frac{|\widehat{p}_3\widehat{p}_4|}{2}\cos\alpha$$

Thus, one obtains

$$\overline{\widetilde{u}_3\widetilde{u}_4} + \overline{\widetilde{v}_3\widetilde{v}_4} + \overline{\widetilde{p}_3\widetilde{p}_4} + \frac{\overline{\widetilde{p}_3\widetilde{u}_4} + \overline{\widetilde{p}_4\widetilde{u}_3}}{M_{x,0}} =$$

$$= \left[-\frac{R^2-M_{x,0}^2}{1-R^2M_{x,0}^2} + \frac{(1-R^2)\left(1-M_{x,0}^2\right)}{1-R^2M_{x,0}^2} + 1 - \frac{R+M_{x,0}}{(1+RM_{x,0})M_{x,0}} + \right.$$

$$\left. + \frac{R-M_{x,0}}{(1-RM_{x,0})M_{x,0}}\right]\frac{|\widehat{p}_3\widehat{p}_4|}{2}\cos\alpha = 0.$$

An upstream and a downstream propagating pressure wave do not couple in the flux-averaging procedure.

The individual crosscoupling terms between a downstream propagating pressure wave and a vorticity wave can be rewritten to yield:

$$\frac{\overline{\widetilde{p}_3\widetilde{u}_2}}{M_{x,0}} = +\frac{1}{M_{x,0}}\frac{|\widehat{p}_3\widehat{u}_2|}{2}\cos\beta$$

$$\overline{\widetilde{u}_3\widetilde{u}_2} = +\frac{R-M_{x,0}}{1-RM_{x,0}}\overline{\widetilde{p}_3\widetilde{u}_2} = +\frac{R-M_{x,0}}{1-RM_{x,0}}\frac{|\widehat{p}_3\widehat{u}_2|}{2}\cos\beta$$

$$\overline{\widetilde{v}_3\widetilde{v}_2} = -\frac{(1-R^2)(\Omega-M_{y,0})^2}{(1-RM_{x,0})M_{x,0}}\overline{\widetilde{p}_3\widetilde{u}_2} = -\frac{1-M_{x,0}^2}{(1-RM_{x,0})M_{x,0}}\frac{|\widehat{p}_3\widehat{u}_2|}{2}\cos\beta$$

Summing all terms, one obtains

$$\overline{\widetilde{u}_3\widetilde{u}_2} + \overline{\widetilde{v}_3\widetilde{v}_2} + \frac{\overline{\widetilde{p}_3\widetilde{u}_2}}{M_{x,0}} = \frac{1}{M_{x,0}}\left[\frac{(R-M_{x,0})M_{x,0}}{1-RM_{x,0}} - \frac{1-M_{x,0}^2}{1-RM_{x,0}} + 1\right]\frac{|\widehat{p}_3\widehat{u}_2|}{2}\cos\beta = 0.$$

Vorticity waves and pressure waves do not couple in the flux-averaging procedure. In this very same manner, one can prove the third of the above conditions for crosscoupling between an upstream propagating pressure wave and a vorticity wave.

Appendix E

Separation Properties for Evanescent Pressure Waves

In accordance with equation (2.37), one would have to show that the following three relations hold in order to prove that there is no crosscoupling between the evanescent pressure waves, and between vorticity waves and evanescent pressure waves:

$$\overline{\tilde{u}_3\tilde{u}_4} + \overline{\tilde{v}_3\tilde{v}_4} + \overline{\tilde{p}_3\tilde{p}_4} + \frac{\overline{\tilde{p}_3\tilde{u}_4} + \overline{\tilde{p}_4\tilde{u}_3}}{M_{x,0}} = 0$$

$$\overline{\tilde{u}_3\tilde{u}_2} + \overline{\tilde{v}_3\tilde{v}_2} + \frac{\overline{\tilde{p}_3\tilde{u}_2}}{M_{x,0}} = 0$$

$$\overline{\tilde{u}_4\tilde{u}_2} + \overline{\tilde{v}_4\tilde{v}_2} + \frac{\overline{\tilde{p}_4\tilde{u}_2}}{M_{x,0}} = 0$$

For evanescent pressure waves, the right eigenvectors $\vec{w}_{r,i}$ are defined by

$$\vec{w}_2 = \begin{bmatrix} 0 \\ -M_{x,0} \\ \Omega - M_{y,0} \\ 0 \end{bmatrix} \qquad \vec{w}_{3,4} = \begin{bmatrix} -\left(\pm iRM_{x,0} - 1\right) \\ \left(\pm iR - M_{x,0}\right) \\ \left(1 + R^2\right)\left(\Omega - M_{y,0}\right) \\ -\left(\pm iRM_{x,0} - 1\right) \end{bmatrix}.$$

The subscripts 2, 3, and 4 denote a vorticity wave and pressure waves decaying downstream and upstream, respectively. Note the complex nature of the pressure wave eigenvectors; there are phase shifts other than $\pm\pi$ between the pressure or density perturbation and the velocity perturbations. R and Ω are now defined by

$$R = \sqrt{\frac{1 - M_{x,0}^2}{\left(\Omega - M_{y,0}\right)^2} - 1} \quad \text{and} \quad \Omega = \frac{\omega_f}{a_0 k_y}.$$

Figure E.1 presents the elements of the eigenvectors corresponding to the evanescent pressure waves in the complex plane. Without subscripts, the variable φ denotes the phase shift between the complex pressure amplitudes $\hat{p}_3$ and $\hat{p}_4$. φ_{pu} is the phase angle

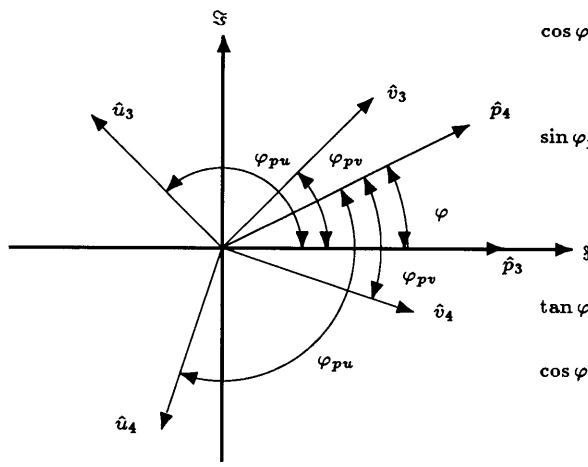

$$\tan\varphi_{pu} = -\frac{\left(1 - M_{x,0}^2\right) R}{\left(1 + R^2\right) M_{x,0}}$$

$$\cos\varphi_{pu} = -\frac{\left(1 + R^2\right) M_{x,0}}{\sqrt{\left(1 + R^4\right) M_{x,0}^2 + \left(1 + M_{x,0}^4\right) R^2}}$$

$$\sin\varphi_{pu} = \frac{\left(1 - M_{x,0}^2\right) R}{\sqrt{\left(1 + R^4\right) M_{x,0}^2 + \left(1 + M_{x,0}^4\right) R^2}}$$

$$\tan\varphi_{pv} = RM_{x,0}$$

$$\cos\varphi_{pv} = \frac{1}{\sqrt{1 + R^2 M_{x,0}^2}}$$

$$\sin\varphi_{pv} = \frac{RM_{x,0}}{\sqrt{1 + R^2 M_{x,0}^2}}$$

Figure E.1: Eigenvectors for evanescent pressure waves in the complex plane

between the pressures $\widehat{p}_{3,4}$ and the corresponding axial velocities $\widehat{u}_{3,4}$. Correspondingly, the variable φ_{pv} denotes the phase angles between the pressures and the corresponding velocities $\widehat{v}_{3,4}$. The following relationships between the components of the eigenvectors hold for evanescent pressure waves:

$$\widehat{u}_3 = \frac{\sqrt{\left(1 + R^4\right) M_{x,0}^2 + \left(1 + M_{x,0}^4\right) R^2}}{1 + R^2 M_{x,0}^2} \widehat{p}_3 e^{+i\varphi_{pu}}$$

$$\widehat{u}_4 = \frac{\sqrt{\left(1 + R^4\right) M_{x,0}^2 + \left(1 + M_{x,0}^4\right) R^2}}{1 + R^2 M_{x,0}^2} \widehat{p}_4 e^{-i\varphi_{pu}}$$

$$\widehat{v}_3 = \frac{\left(1 + R^2\right)\left(\Omega - M_{y,0}\right)}{\sqrt{1 + R^2 M_{x,0}^2}} \widehat{p}_3 e^{+i\varphi_{pv}}$$

$$\widehat{v}_4 = \frac{\left(1 + R^2\right)\left(\Omega - M_{y,0}\right)}{\sqrt{1 + R^2 M_{x,0}^2}} \widehat{p}_4 e^{-i\varphi_{pv}}$$

Thus, the individual pressure crosscoupling terms can be written as

$$\frac{\overline{\widetilde{p}_4 \widetilde{u}_3}}{M_{x,0}} = \frac{\sqrt{\left(1 + R^4\right) M_{x,0}^2 + \left(1 + M_{x,0}^4\right) R^2}}{\left(1 + R^2 M_{x,0}^2\right) M_{x,0}} \overline{\widetilde{p}_4 \left(\widetilde{p}_3 e^{+i\varphi_{pu}}\right)} =$$

$$\frac{\sqrt{\left(1+R^4\right)M_{x,0}^2+\left(1+M_{x,0}^4\right)R^2}}{\left(1+R^2M_{x,0}^2\right)M_{x,0}}\,\frac{|\widehat{p}_3\widehat{p}_4|}{2}\cos\left(\varphi_{pu}-\varphi\right),$$

$$\frac{\overline{\widetilde{p}_3\widetilde{u}_4}}{M_{x,0}}=\frac{\sqrt{\left(1+R^4\right)M_{x,0}^2+\left(1+M_{x,0}^4\right)R^2}}{\left(1+R^2M_{x,0}^2\right)M_{x,0}}\,\overline{\widetilde{p}_3\left(\widetilde{p}_4e^{-i\varphi_{pu}}\right)}=$$

$$\frac{\sqrt{\left(1+R^4\right)M_{x,0}^2+\left(1+M_{x,0}^4\right)R^2}}{\left(1+R^2M_{x,0}^2\right)M_{x,0}}\,\frac{|\widehat{p}_3\widehat{p}_4|}{2}\cos\left(\varphi_{pu}-\varphi\right),$$

$$\overline{\widetilde{u}_3\widetilde{u}_4}=\frac{\left(1+R^4\right)M_{x,0}^2+\left(1+M_{x,0}^4\right)R^2}{\left(1+R^2M_{x,0}^2\right)^2}\,\overline{\left(\widetilde{p}_3e^{+i\varphi_{pu}}\right)\left(\widetilde{p}_4e^{-i\varphi_{pu}}\right)}=$$

$$\frac{\left(1+R^4\right)M_{x,0}^2+\left(1+M_{x,0}^4\right)R^2}{\left(1+R^2M_{x,0}^2\right)^2}\,\frac{|\widehat{p}_3\widehat{p}_4|}{2}\cos\left(2\varphi_{pu}-\varphi\right),$$

$$\overline{\widetilde{v}_3\widetilde{v}_4}=\frac{\left(1+R^2\right)\left(\Omega-M_{y,0}\right)}{\left(1+R^2M_{x,0}^2\right)}\,\overline{\left(\widetilde{p}_3e^{+i\varphi_{pv}}\right)\left(\widetilde{p}_4e^{-i\varphi_{pv}}\right)}=$$

$$\frac{\left(1+R^2\right)^2\left(1-M_{x,0}^2\right)}{1+R^2M_{x,0}^2}\,\frac{|\widehat{p}_3\widehat{p}_4|}{2}\cos\left(2\varphi_{pv}-\varphi\right),$$

and

$$\overline{\widetilde{p}_3\widetilde{p}_4}=\frac{|\widehat{p}_3\widehat{p}_4|}{2}\cos\varphi.$$

This leads to

$$\overline{\widetilde{u}_3\widetilde{u}_4}+\overline{\widetilde{v}_3\widetilde{v}_4}+\overline{\widetilde{p}_3\widetilde{p}_4}+\frac{\overline{\widetilde{p}_3\widetilde{u}_4}+\overline{\widetilde{p}_4\widetilde{u}_3}}{M_{x,0}}=$$

$$\left[2\,\frac{\sqrt{\left(1+R^4\right)M_{x,0}^2+\left(1+M_{x,0}^4\right)R^2}}{\left(1+R^2M_{x,0}^2\right)M_{x,0}}\left(\cos\varphi_{pu}\cos\varphi+\sin\varphi_{pu}\sin\varphi\right)+\right.$$

$$\frac{\left(1+R^4\right)M_{x,0}^2+\left(1+M_{x,0}^4\right)R^2}{\left(1+R^2M_{x,0}^2\right)^2}\left[\left(2\cos^2\varphi_{pu}-1\right)\cos\varphi+2\sin\varphi_{pu}\cos\varphi_{pu}\sin\varphi\right]+$$

$$\left.\frac{\left(1+R^2\right)\left(1-M_{x,0}^2\right)}{1+R^2M_{x,0}^2}\left[\left(2\cos^2\varphi_{pv}-1\right)\cos\varphi+2\sin\varphi_{pv}\cos\varphi_{pv}\sin\varphi\right]+\cos\varphi\right]\frac{|\widehat{p}_3\widehat{p}_4|}{2}.$$

After some algebraic manipulations involving the phase angles defined in figure E.1, the final result is

$$\overline{\widetilde{u}_3\widetilde{u}_4} + \overline{\widetilde{v}_3\widetilde{v}_4} + \overline{\widetilde{p}_3\widetilde{p}_4} + \frac{\overline{\widetilde{p}_3\widetilde{u}_4} + \overline{\widetilde{p}_4\widetilde{u}_3}}{M_{x,0}} = \frac{\left(1 - M_{x,0}^2\right) R^2}{1 + R^2 M_{x,0}^2} \left(\frac{\sin\varphi}{M_{x,0}} + \cos\varphi\right) \frac{|\widehat{p}_3\widehat{p}_4|}{2}.$$

It is seen that there is, in general, crosscoupling between the two evanescent pressure waves.

There is, however, no crosscoupling between an evanescent pressure wave and a vorticity wave. To show this, let φ now denote the phase shift between the pressure $\widehat{p}_3$ of a pressure wave decaying downstream and the axial velocity $\widehat{u}_2$ of a vorticity wave. Again, the individual crosscoupling terms are first rewritten as:

$$\frac{\overline{\widetilde{p}_3\widetilde{u}_2}}{M_{x,0}} = \frac{|\widehat{p}_3\widehat{p}_4|}{2M_{x,0}} \cos\varphi$$

$$\overline{\widetilde{u}_3\widetilde{u}_2} = \frac{\sqrt{\left(1 + R^4\right) M_{x,0}^2 + \left(1 + M_{x,0}^4\right) R^2}}{1 + R^2 M_{x,0}^2} \overline{\left(\widetilde{p}_3 e^{+i\varphi_{pu}}\right) \widetilde{u}_2} =$$

$$\frac{\sqrt{\left(1 + R^4\right) M_{x,0}^2 + \left(1 + M_{x,0}^4\right) R^2}}{1 + R^2 M_{x,0}^2} \frac{|\widehat{p}_3\widehat{u}_2|}{2} \left(\cos\varphi_{pu}\cos\varphi + \sin\varphi_{pu}\sin\varphi\right)$$

$$\overline{\widetilde{v}_3\widetilde{v}_2} = -\frac{\left(1 + R^2\right)\left(\Omega - M_{y,0}\right)^2}{\sqrt{1 + R^2 M_{x,0}^2} M_{x,0}} \overline{\left(\widetilde{p}_3 e^{+i\varphi_{pv}}\right) \widetilde{u}_2} =$$

$$-\frac{\left(1 + R^2\right)\left(1 - M_{x,0}^2\right)}{\sqrt{1 + R^2 M_{x,0}^2} M_{x,0}} \frac{|\widehat{p}_3\widehat{u}_2|}{2} \left(\cos\varphi_{pv}\cos\varphi + \sin\varphi_{pv}\sin\varphi\right)$$

Summing the above terms and substituting the expressions of figure E.1 for φ_{pu} and φ_{pv} into the above equation, one obtains

$$\overline{\widetilde{u}_3\widetilde{u}_2} + \overline{\widetilde{v}_3\widetilde{v}_2} + \frac{\overline{\widetilde{p}_3\widetilde{u}_2}}{M_{x,0}} = 0.$$

In the very same manner, one can prove that there is no crosscoupling between an evanescent pressure wave decaying upstream and a vorticity wave.

Appendix F

Single Evanescent Pressure Waves

In order to show that a single evanescent pressure wave does not lead to a rise in entropy under the flux-averaging procedure, one has to show that

$$\overline{\widetilde{p}_3^2} + \overline{\widetilde{u}_3^2} + \overline{\widetilde{v}_3^2} + 2\,\frac{\overline{\widetilde{p}_3\widetilde{u}_3}}{M_{x,0}} = 0$$

holds. The definitions of the phase angle φ_{pu}, R, and Ω are the same as in appendix E. The individual terms above can be rewritten in the following form:

$$\overline{\widetilde{p}_3^2} = \frac{|\widehat{p}_3^2|}{2}$$

$$\overline{\widetilde{u}_3^2} = \frac{|\widehat{u}_3^2|}{2} = \frac{\left(1+R^4\right)M_{x,0}^2 + \left(1+M_{x,0}^4\right)R^2}{\left(1+R^2M_{x,0}^2\right)^2}\,\frac{|\widehat{p}_3^2|}{2}$$

$$\overline{\widetilde{v}_3^2} = \frac{|\widehat{v}_3^2|}{2} = \frac{\left(\Omega - M_{y,0}\right)^2\left(1+R^2\right)}{1+R^2M_{x,0}^2}\,\frac{|\widehat{p}_3^2|}{2} = \frac{\left(1-M_{x,0}^2\right)\left(1+R^2\right)^2}{1+R^2M_{x,0}^2}\,\frac{|\widehat{p}_3^2|}{2}$$

$$\frac{\overline{\widetilde{p}_3\widetilde{u}_3}}{M_{x,0}} = \frac{\sqrt{\left(1+R^4\right)M_{x,0}^2 + \left(1+M_{x,0}^4\right)R^2}}{\left(1+R^2M_{x,0}^2\right)M_{x,0}}\,\overline{\widetilde{p}_3\left(\widetilde{p}_3 e^{i\varphi_{pu}}\right)} =$$

$$\frac{\sqrt{\left(1+R^4\right)M_{x,0}^2 + \left(1+M_{x,0}^4\right)R^2}}{\left(1+R^2M_{x,0}^2\right)M_{x,0}}\,\frac{|\widehat{p}_3^2|}{2}\cos\varphi_{pu}$$

This leads to

$$\overline{\widetilde{u}^2}_3 + \overline{\widetilde{v}^2}_3 + \overline{\widetilde{p}^2}_3 + 2\,\frac{\overline{\widetilde{p}_3\widetilde{u}_3}}{M_{x,0}} =$$

$$\left[1 + \frac{\left(1+R^4\right)M_{x,0}^2 + \left(1+M_{x,0}^4\right)R^2}{\left(1+R^2M_{x,0}^2\right)^2} + \frac{\left(1-M_{x,0}^2\right)\left(1+R^2\right)^2}{1+R^2M_{x,0}^2} + \right.$$

$$\left. 2\frac{\sqrt{\left(1+R^4\right)M_{x,0}^2 + \left(1+M_{x,0}^4\right)R^2}}{\left(1+R^2M_{x,0}^2\right)M_{x,0}}\cos\varphi_{pu}\right]\frac{|\widehat{p}_3^2|}{2} = 0.$$

Therefore, a single evanescent pressure wave does not lead to an entropy rise.

Appendix G

Left Eigenvectors of the Linearized Euler Equations

The left eigenvectors, corresponding to the right eigenvectors $\vec{w}_{r,i}$ of section 2.1, are needed to determine the individual wave amplitudes contained in an arbitrary unsteady perturbation superimposed upon a uniform mean flow. Note that the left and the right eigenvectors are not normalized, i.e. $\vec{w}_{l,i} * \vec{w}_{r,j} \neq \delta_{ij}$. The symbol δ_{ij} denotes the Kronecker delta function defined in appendix C.

$$\vec{w}_{l,1} = \begin{bmatrix} 1 \\ 0 \\ 0 \\ -1 \end{bmatrix}^T$$

$$\vec{w}_{l,2} = \begin{bmatrix} 0 \\ -M_{x,0} \\ \Omega - M_{y,0} \\ -1 \end{bmatrix}^T$$

$$\vec{w}_{l,3/4} = \begin{bmatrix} 0 \\ \pm(\Omega - M_{y,0}) \\ \pm M_{x,0} \\ (\Omega - M_{y,0})\, R \end{bmatrix}^T$$

Appendix H

Scaling Arguments in the Near-Wall Approximation

Close to the wall, the inertial terms in the streamwise momentum equation (4.11) can be neglected in the steady as well as the linearized unsteady equations. To first order, the streamwise pressure gradients near the wall are balanced by the normal shear stress.

$$\overline{\tau} = \overline{\tau}_w + \left(\frac{\partial \overline{p}}{\partial s}\right) n + \ldots$$

$$\widetilde{\tau} = \widetilde{\tau}_w + \left(\frac{\partial \widetilde{p}}{\partial s}\right) n + \ldots$$

It follows that both the steady and the unsteady streamwise velocity, $\overline{u}$ and $\widetilde{u}$, vary linearly with the normal coordinate n close to the wall. The mean flow continuity equation is

$$\overline{\rho}\left(\frac{\partial \overline{u}}{\partial s} + \frac{\partial \overline{v}}{\partial n}\right) + \overline{u}\,\frac{\partial \overline{\rho}}{\partial s} + \overline{v}\,\frac{\partial \overline{\rho}}{\partial n} = 0.$$

Moving towards the wall, the 1st, 3rd, and 4th term clearly vanish because $\overline{u}$ and $\overline{v}$ approach zero. The second term then also vanishes, which implies that, at a minimum, $\overline{v} \sim n^2$. This holds for an adiabatic wall, and for an isothermal wall as well.

The first-order perturbation of the continuity equation (4.16) is

$$\frac{\partial \widetilde{\rho}}{\partial t} + \overline{\rho}\left(\frac{\partial \widetilde{u}}{\partial s} + \frac{\partial \widetilde{v}}{\partial n}\right) + \widetilde{\rho}\left(\frac{\partial \overline{u}}{\partial s} + \frac{\partial \overline{v}}{\partial n}\right) + \overline{u}\,\frac{\partial \widetilde{\rho}}{\partial s} + \overline{v}\,\frac{\partial \widetilde{\rho}}{\partial n} + \widetilde{u}\,\frac{\partial \overline{\rho}}{\partial s} + \widetilde{v}\,\frac{\partial \overline{\rho}}{\partial n} = 0.$$

Moving towards the wall, all the above terms, except the time derivative and the unknown term containing the normal derivative $(\partial \widetilde{v}/\partial n)$, vanish. The normal velocity at the wall results from an adiabatic or isothermal compression in response to the unsteady pressure acting on the boundary layer. At an adiabatic boundary, $(\partial \widetilde{T}/\partial n|_w) = 0$ holds.

Together with the equation of state and $(\partial\widetilde{p}/\partial n)=0$ from the boundary layer approximation, this leads to the conclusion that $\widetilde{\rho}$ is independent of the normal coordinate at the wall. Therefore, $\widetilde{v}\sim n$ must hold to have $\overline{\rho}(\partial\widetilde{v}/\partial n)$ balance the unsteady term $(\partial\widetilde{\rho}/\partial t)$. For a constant temperature boundary, the equation of state gives $(\partial\widetilde{\rho}/\partial t)\sim(\partial\widetilde{p}/\partial t)$. Together with $(\partial\widetilde{p}/\partial n)=0$, this again leads to the conclusion that $\widetilde{v}\sim n$.

Coming back to the linearized streamwise momentum equation (4.17) above, one concludes that all inertial terms on the left hand side are of $O(n^2)$ near the wall except for the unsteady term and the convective term $\widetilde{v}(\partial\overline{u}/\partial n)$ which are of $O(n)$. Those two terms are the first to play a role as one moves away from the wall. It is not the convective term (4.58), but (4.60), whose neglect introduces the largest errors at the wall. From (4.44) and (4.45) one obtains

$$\left|\frac{\partial\widetilde{u}}{\partial t}\right| \approx \frac{1}{\overline{\rho}_w}\,\frac{k_s}{k_e}\,\frac{n}{\delta_f}\,|\widetilde{p}|$$

using a Taylor series expansion near the wall. From (4.23), one obtains the near-wall approximation of the linearized continuity equation as

$$\frac{\partial\widetilde{v}}{\partial n} \approx -k_e\,\frac{1}{\overline{\rho}}\,\frac{\partial\widetilde{\rho}}{\partial t}$$

which leads to

$$|\widetilde{v}| \approx k_e\,M_e^2\,n\,|\widetilde{p}|$$

for an adiabatic boundary. In the calculation of $|\widetilde{v}|$, the relation $(\widetilde{\rho}/\overline{\rho}_w)=M_e^2\widetilde{p}$ has been used; for a constant temperature boundary, the relation $(\widetilde{\rho}/\overline{\rho}_w)=(M_e^2\widetilde{p}/\gamma)$ has to be used. The ratio (4.60) can now be written as

$$\widetilde{v}\frac{\partial\overline{u}}{\partial n}\Big/\frac{\partial\widetilde{u}}{\partial t} \approx \frac{\overline{\rho}_w}{\rho_e}\,\frac{k_e}{k_s}\,\frac{\partial\overline{u}}{\partial n}\,M_e^2\,\frac{\delta_f}{c_a}.$$

For a pressure wave propagating (approximately in or against the freestream) over a laminar flat plate boundary layer with $(\partial\overline{u}/\partial n)\approx 0.332\sqrt{Re/s}$, the argument can be made more precise:

$$\widetilde{v}\frac{\partial\overline{u}}{\partial n}\Big/\frac{\partial\widetilde{u}}{\partial t} \approx 0.332\,\frac{M_e\,(1\pm M_e)}{\sqrt{k_e s}}$$

Appendix I

Length and Time Scales in Turbulent Flow

Unsteadiness causes extra time-mean dissipation in an unsteady boundary layer. It is, a priori, not obvious whether the dissipation mechanism is turbulent even if the mean flow is turbulent. To address this issue, the forcing time scale T_f is compared to the characteristic turbulent time scale T_τ and the unsteady boundary layer thickness δ_f to the turbulent length scale l_t. The time scale of turbulence is

$$T_\tau = \frac{\nu}{u_\tau^2}.$$

For an incompressible turbulent boundary layer along a flat plate at zero incidence, the time-mean wall shear is approximately

$$\frac{\overline{\tau}_w}{\rho} \approx 0.0225 \left(\frac{\nu}{\overline{U}_e \overline{\delta}} \right)^{1/4} \overline{U}_e^2,$$

with the steady boundary layer thickness defined by (4.85). Using the above equation and equation (4.89), one can rewrite the ratio of time scales as

$$\frac{T_\tau}{T_f} \approx 5.52 \frac{k_{e,s}}{Re_s^{4/5}} \sim s^{1/5}.$$

The ratio of length scales becomes

$$\frac{l_t}{\delta_f} \approx 5.88 \frac{k_{e,s}^{1/2}}{Re_s^{2/5}} \sim \sqrt{\frac{T_\tau}{T_f}}.$$

Except for the leading edge region, the time scale of the turbulent motion is much less than the forcing time scale. This implies that turbulent eddies move much more than a characteristic length l_t during a period. A period much larger than the turbulent time scale also provides the rationale for the application of a steady turbulence model to an unsteady flow. For Reynolds numbers and reduced frequencies typical of turbomachinery ($Re = 10^6$ and $k_e = 5$), the ratio of length scales is $O(0.1)$. Turbulent diffusion of momentum takes place in the unsteady boundary layer.

Appendix J

Attenuation of Pressure Waves at Boundaries

The attenuation coefficient (4.101) can also be obtained from the high-reduced-frequency limit of the linearized continuity equation (4.23).

$$\frac{\partial \tilde{v}}{\partial n} = -k_e M_e^2 \frac{\partial \tilde{p}}{\partial t} - \frac{\partial \tilde{u}}{\partial s} \tag{J.1}$$

The relation $\tilde{\rho} = \tilde{p} M_e^2$, valid in compressible isentropic mean flow, was used in (J.1). Using the full viscous expressions for the unsteady pressure and streamwise velocity, one may recast (J.1) as

$$\begin{aligned}\frac{\partial \tilde{v}}{\partial n}|_{vis} = {} & ik_e M_e^2 \left[(1-\beta)\exp\{ik_n n\} + \exp\{-ik_n n\}\right] \hat{p} \exp\{i(k_s s - t)\} \\ & - ik_e \left(\frac{k_s}{k_e}\right)^2 \left(1 - \exp\left\{\frac{(i-1)}{\sqrt{2}} \frac{n}{\delta_f}\right\}\right) [(1-\beta)\exp\{ik_n n\} \\ & + \exp\{-ik_n n\}] \hat{p} \exp\{i(k_s s - t)\}\,. \end{aligned} \tag{J.2}$$

For the inviscid case, i.e. for $\beta \to 0$ and $Re \to \infty$, equation (J.2) simplifies to

$$\frac{\partial \tilde{v}}{\partial n}|_{inv} = ik_e \left[M_e^2 - \left(\frac{k_s}{k_e}\right)^2\right] \left(\exp\{ik_n n\} + \exp\{-ik_n n\}\right) \hat{p} \exp\{i(k_s s - t)\}, \tag{J.3}$$

which corresponds to a standing wave with a normal velocity

$$\tilde{v}|_{inv} = \left(\frac{k_e}{k_n}\right) \left[M_e^2 - \left(\frac{k_s}{k_e}\right)^2\right] \left(\exp\{ik_n n\} - \exp\{-ik_n n\}\right) \hat{p} \exp\{i(k_s s - t)\}. \tag{J.4}$$

In the inviscid case, any normal derivative of $\tilde{v}$ is solely due to a phase shift governed by the wave number k_n of the standing wave. It is instructive to contrast this to the viscous case. To this end, one takes the difference between the viscous and the inviscid normal gradient.

$$\frac{\partial \tilde{v}}{\partial n}|_{vis} - \frac{\partial \tilde{v}}{\partial n}|_{inv} = \beta i k_e \left[\left(1 - \exp\left\{\frac{(i-1)}{\sqrt{2}} \frac{n}{\delta_f}\right\}\right) \left(\frac{k_s}{k_e}\right)^2 - M_e^2\right] \hat{p} \exp\{i(k_s s + k_n n - t)\}$$

$$+ ik_e \left(\frac{k_s}{k_e}\right)^2 \exp\left\{\frac{(i-1)}{\sqrt{2}}\frac{n}{\delta_f}\right\} \left[\exp\{ik_n n\}+\exp\{-ik_n n\}\right] \hat{p} \exp\{i(k_s s - t)\} \quad \text{(J.5)}$$

The exponential factor in the first term on the right-hand side of equation (J.5) may be neglected because it is multiplied by the small factor β and thus negligible when compared to the second term. Equation (J.5) will be integrated to obtain the difference in the unsteady normal velocities at the boundary layer edge. The limits of integration are 0 and ∞ on a scale (n/δ_f) or 0 and $O(\beta)$ on a scale $k_n n$. Upon integration, the second term on the right hand side of (J.5) contributes the dominating term and one obtains approximately

$$\tilde{v}_{vis} - \tilde{v}_{inv} = \left(\frac{k_s}{k_e}\right)^2 \sqrt{\frac{k_e}{Re}} \left(\exp\{ik_n n\}+\exp\{-ik_n n\}\right) \hat{p} \exp\{i(k_s s - t)\} \exp\left\{i\frac{3\pi}{4}\right\}. \quad \text{(J.6)}$$

In keeping with the arguments advanced above, the dependence of the second term on the right-hand side of (J.5) on the phase angle $\pm k_n n$ has been neglected in the integration. The result (J.6) cannot readily be compared to the solution of the energy balance approach (4.100) because, due to its nature, it did not retain phase information. Figure J.1 helps to clarify the issue.

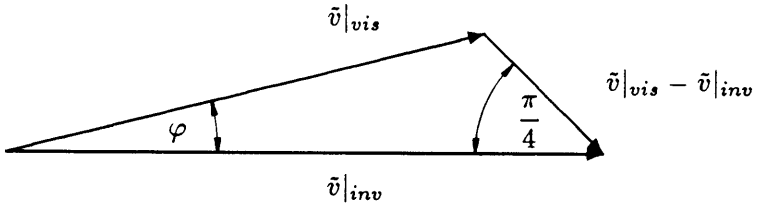

Figure J.1: Normal velocity vectors in viscous and inviscid flow

Utilizing (4.69) and rewriting (J.6) in terms of magnitudes, one obtains

$$|\hat{v}_{vis}| - |\hat{v}_{inv}| \approx M_e \sqrt{2\,\frac{k_e}{Re}} \tan\theta \sin\theta \; |\hat{p}|\, M_e \cos\theta = \beta_1 \; |\hat{p}|\, M_e \cos\theta, \quad \text{(J.7)}$$

because the phase shift φ between $\tilde{v}_{vis}$ and $\tilde{v}_{inv}$ is small. Noting that $|\tilde{v}| = |\tilde{p} M_e| \cos\theta$, it becomes obvious that the edge of the unsteady boundary layer exhibits an additional normal velocity as if it were exited by an acoustic wave with an amplitude $\beta_1 |\hat{p}_{e,m}|$. This is exactly what happens physically, because the amplitude of the reflected wave has been diminished by a factor β due to unsteady dissipation; both approaches lead to

the same attenuation factor

$$\beta_1 \;=\; M_e \sqrt{2\frac{k_e}{Re}}\tan\theta\sin\theta. \tag{J.8}$$

The unsteady pressure and the unsteady velocity at the edge of the unsteady boundary layer can be related to the dissipated energy as follows:

The second-order time-mean dissipation function $\overline{\overline{\Phi}}_{2i}$ (in dimensional form) can be transformed to read

$$\overline{\int_0^\infty \mu\left(\frac{\partial\tilde{u}}{\partial n}\right)^2 dn} = \overline{\int_0^\infty \frac{\partial}{\partial n}\left(\tilde{u}\,\mu\frac{\partial\tilde{u}}{\partial n}\right) dn} - \overline{\int_0^\infty \tilde{u}\frac{\partial}{\partial n}\left(\mu\frac{\partial\tilde{u}}{\partial n}\right) dn}. \tag{J.9}$$

In the high-reduced frequency limit, the first term on the right-hand side is zero at the wall and at the edge of the unsteady boundary layer. Using (4.39) in dimensional form, the right-hand side can be written in the form

$$\overline{\int_0^\infty \mu\left(\frac{\partial\tilde{u}}{\partial n}\right)^2 dn} = \overline{\int_0^\infty \tilde{u}\left(\overline{\rho}\frac{\partial\tilde{u}}{\partial t} + \frac{d\tilde{p}}{ds}\right) dn}. \tag{J.10}$$

For a harmonic disturbance, $\tilde{u}$ and $(\partial\tilde{u}/\partial t)$ are $(\pi/2)$ out of phase such that the time mean of their product is identically zero. The right-hand side may be transformed further by

$$\overline{\frac{d\tilde{p}}{ds}\int_0^\infty \tilde{u}\;dn} \;=\; \frac{d}{ds}\left(\overline{\tilde{p}\int_0^\infty \tilde{u}\;dn}\right) - \overline{\tilde{p}\int_0^\infty \frac{\partial\tilde{u}}{\partial s}dn}. \tag{J.11}$$

In the high-reduced-frequency limit, the first term on the right-hand side is again zero. Due to the assumption of parallel mean flow, it is independent of the streamwise coordinate. The high-reduced-frequency limit of the continuity equation in dimensional form reads

$$\frac{\partial\tilde{\rho}}{\partial t} + \overline{\rho}\left(\frac{\partial\tilde{u}}{\partial s} + \frac{\partial\tilde{v}}{\partial n}\right) = 0. \tag{J.12}$$

Substituting (J.10) and $(\partial\tilde{u}/\partial s)$ from (J.12) into (J.11), one obtains

$$\overline{\int_0^\infty \mu\left(\frac{\partial\tilde{u}}{\partial n}\right)^2 dn} = \overline{\tilde{p}\left(\tilde{v}|_{n=\infty} + \frac{1}{\overline{\rho}}\int_0^\infty \frac{\partial\tilde{\rho}}{\partial t}dn\right)}. \tag{J.13}$$

The first term on the right-hand side represents the work transferred into the unsteady boundary layer while the second term represents the potential energy stored in the boundary layer.